Alma Mater Studiorum · University of Bologna

School of Science
Department of Physics and Astronomy
Master Degree in Physics

Modeling of high resolution depth of interaction detector for Small Animal In-Beam PET Scanner

Supervisor:
Prof. Roberto Spighi

Submitted by:
Davide Boscaini

External Supervisors:
Prof. Katia Parodi
Dr. Munetaka Nitta

Academic Year 2024/2025

Master's Thesis

Modeling of high resolution depth of interaction detector for Small Animal In-Beam PET Scanner

Faculty of Physics
Ludwig-Maximilians-Universität München

Davide Boscaini

Munich, July, 2025

Submitted in partial fulfillment of the requirements for the degree of M. Sc.
Supervised by Prof. Katia Parodi and Dr. Munetaka Nitta

Abstract

The development of novel PET imaging systems plays a key role in advancing in-beam range verification techniques for particle therapy. Within the ERC-funded SIRMIO project at LMU (www.lmu.de/sirmio), a compact, high-resolution PET scanner has been developed to accurately monitor dose delivery in preclinical proton irradiation studies. This thesis contributes to optimizing this technology by modeling and characterizing the depth-of-interaction (DOI) detector response of a single detection module, utilizing both experimental data and Geant4-based Monte Carlo simulations.

Experimental measurements were performed using a micro Derenzo phantom (MediLumine, Canada) filled with ^{18}F-FDG, supplemented by acquisitions with a ^{22}Na source. A dedicated analysis pipeline, combining ROOT frameworks and custom Python scripts, was developed to extract precise spatial and spectral response parameters for each detector pixel. Parameters analyzed include pixel positions, spatial spread, and per-channel energy distributions.

The generated pixel-wise database provides detailed insights into the detector's response, significantly advancing the understanding of spectral and spatial features at the pixel level. Although this pixel-wise model has not yet been implemented for event-level filtering, it represents a critical step toward advanced classification methods aimed at selectively retaining true 511 keV single-interaction events. Ultimately, this foundational modeling work is expected to improve the overall spatial resolution, localization accuracy, and imaging performance of the SIRMIO PET scanner.

Contents

Chapter 1

Introduction

Cancer is a group of diseases characterized by uncontrolled cell growth, with the potential to invade surrounding tissues or metastasize to distant organs. It remains a leading cause of mortality worldwide, placing immense pressure on global health systems. In 2022, the European Union reported 2.74 million new cancer cases, leading to approximately 1.3 million cancer-related deaths [1]

The incidence and mortality rates of cancer in Europe are projected to rise significantly by 2040, primarily due to an aging population. Estimates suggest a 19% increase in cancer diagnoses and a 27% rise in mortality compared to 2022, highlighting the disproportionate impact of demographic changes and emphasizing the need for effective intervention strategies [1].

The treatment of cancer involves several strategies, including chemotherapy, surgery, radiotherapy, and immunotherapy. Radiotherapy, especially ion beam therapy, has become notable for its accuracy in targeting tumors while reducing harm to nearby healthy tissues. Progress in this area continues to influence current oncology practices, tackling the difficulties presented by the rising incidence of cancer.

This chapter provides an overview of radiation therapy, including a comparative analysis of photon and ion beam therapy, emphasizing their respective advantages and challenges. Building on these considerations, it explores range verification techniques, which form the basis for the motivation and objectives of this thesis. Additionally, the chapter introduces the SIRMIO project, to which this thesis contributes, outlining its role within this research framework. The chapter concludes by presenting the thesis structure and objectives.

1.1 Radiotherapy and Ion Beam Therapy

The fundamental idea of Radiotherapy and Ion beam therapy lies in the controlled deposition of energy within tumor cells to eliminate them or halt their replication.

Ideally, energy should be deposited only in the tumor region, minimizing exposure to healthy tissue (Figure 1.1). For deep-seated tumors, this can be achieved using different types of radiation, the most common are electromagnetic radiation (X-rays or γ-rays) and charged particles (such as protons or carbon ions). Each type of radiation interacts with matter through different physical interactions, explained in detail in Chapter 2, leasing to a different energy deposited shape as shown in Figure (1.1)

Radiation-induced damage to cancer cells occurs via two primary mechanisms: direct DNA ionization and indirect damage through reactive oxygen species. The cellular response to radiation depends on biological factors (e.g., repair mechanisms) and radiation parameters (e.g., type, energy, dose rate). While some cells successfully repair damage and continue functioning, others undergo apoptosis or mitotic catastrophe if the damage is irreparable.

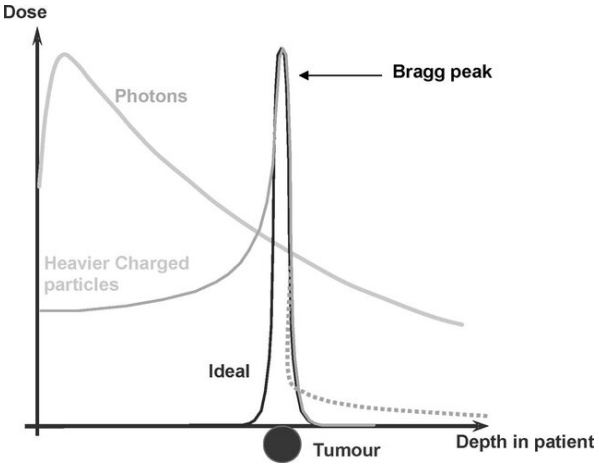

Figure 1.1: Simplified depth dose distributions of photons and heavier charged particles compared with the ideal dose distribution [2]

1.1.1 Radiotherapy

Radiotherapy originated in the late 19$^{\text{th}}$ century following Wilhelm Röntgen's discovery of X-rays in 1895 and Henri Becquerel and Marie Curie's research on radioactivity. The first reported cancer treatment using X-rays occurred in 1899 [3]. Subsequent advancements, such as the introduction of linear accelerators (LINACs) in the 1950s, enabled deeper tissue penetration while reducing collateral exposure [4].

Despite technological advancements, photon therapy's dose deposition profile remains a fundamental limitation. As shown in Figure 1.1, photon beams deposit energy both before and beyond the tumor, increasing the risk of damage to healthy tissues and secondary malignancies. To address these limitations, modern radiotherapy techniques optimize dose distribution and tumor targeting through advanced imaging and beam

modulation methods:

- Intensity-Modulated Radiation Therapy (IMRT): Modulates photon beam intensity across multiple angles to conform to tumor geometry [5].
- Volumetric Modulated Arc Therapy (VMAT): Delivers radiation in a continuous arc, reducing treatment time while maintaining precision [6].
- Stereotactic Body Radiotherapy (SBRT): High-dose, image-guided therapy enabling precise targeting of small tumors [7].

While these methods enhance precision and optimize dose distribution, the inherent limitations of photon therapy have led the scientific community to explore alternative modalities, such as ion beam therapy, which offers distinct physical and biological advantages for treating deep-seated and radioresistant tumors.

1.1.2 Ion Beam Therapy

Ion beam therapy utilizes charged particles such as protons and carbon ions, which interact with matter differently from photons, allowing for superior dose localization. As illustrated in Figure 1.1, ion beams deposit most of their energy at a well-defined depth, known as the Bragg peak, with a rapid dose falloff beyond this point. This characteristic significantly reduces damage to surrounding healthy tissues [8].

This feature has profound clinical implications, enabling greater tumor control while reducing normal tissue toxicity. Ion therapy is particularly effective for treating radioresistant tumors [9]. Additionally, heavier ions such as carbon interact with biological tissue in a way that leads to enhanced biological effectiveness, resulting in more lethal DNA damage to tumor cells compared to conventional photon therapy.

Due to the well-defined depth-dose distribution of ion beams and their complete absorption within the target medium (unlike photons), precise localization of the Bragg peak is crucial. Even slight deviations on the millimeter scale can result in significant dose misplacement, potentially reducing tumor coverage or increasing exposure to surrounding healthy tissues. Consequently, range uncertainties remain a major challenge in ion beam therapy, arising from various factors:

- Hounsfield Unit (HU) to Relative Stopping Power (RSP) Conversion: Treatment planning in ion therapy relies on X-ray CT imaging, which provides tissue information in terms of Hounsfield Units (HU). However, converting HU to Relative Stopping Power (RSP) is nontrivial, as it depends on tissue composition, density, and imaging artifacts. Errors in this conversion introduce range uncertainties of

3–5%, which can translate typically to millimeter-scale deviations in dose deposition, particularly in heterogeneous tissues such as lung or bone [10].

- Patient Positioning and Anatomical Variations: The precise localization of the Bragg peak is further complicated by patient-specific anatomical changes. Variations in organ filling, respiration, cardiac motion, and even weight loss over the course of treatment can lead to shifts in the beam range [11].
- Statistical Effects and Nuclear Interactions: While ions primarily lose energy through electromagnetic interactions, nuclear reactions and multiple Coulomb scattering introduce additional complexities. Multiple Coulomb scattering broadens the beam, reducing spatial precision, while nuclear interactions generate secondary particles, which can deposit dose beyond the intended treatment region. These effects are particularly pronounced in heavier ions such as carbon, where nuclear fragmentation can lead to increased dose uncertainties and unwanted biological effects in surrounding tissues [12].

To enhance treatment precision, in vivo range verification techniques such as PET imaging, prompt gamma detection, and MRI images are actively being developed. These methods leverage treatment plan simulations, quasi-real time imaging, and post treatment validation to ensure accurate dose delivery [13].

1.2 Range Verification using PET

Among the various *in vivo* techniques developed for range verification in particle therapy, **Positron Emission Tomography (PET)** has gained significant attention due to its capacity to indirectly assess the beam range by imaging the distribution of positron-emitting radionuclides generated during irradiation. Unlike other methods, PET does not require additional radiation exposure and allows for post-treatment imaging, making it clinically attractive.

When therapeutic ion beams such as protons or carbon ions interact with atomic nuclei in tissue, they induce nuclear fragmentation reactions that produce unstable isotopes. Among these, ^{15}O, ^{11}C, and ^{13}N are the primary contributors to the PET signal. These nuclides undergo β^+ decay, emitting positrons that subsequently annihilate with electrons, producing two 511 keV photons emitted approximately 180 degrees apart. The detection of these coincident photons by PET scanners allows for three-dimensional reconstruction of the annihilation sites, indirectly reflecting the spatial distribution of the activated nuclei [11].

A fundamental challenge in PET-based range verification is that the spatial distribution of the activity does not directly coincide with the physical dose distribution.

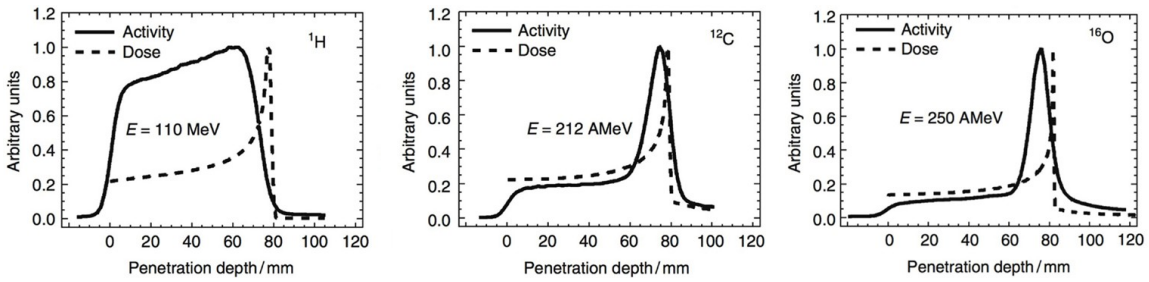

^{1}H irradiation ^{12}C irradiation ^{16}O irradiation

Figure 1.2: Measured positron emission activity (solid line) and physical dose distribution (dashed line) in PMMA for different projectiles. The spatial mismatch between activity and dose depends on ion species and their fragmentation behavior [14].

This is due to both the physical processes of radionuclide production and physiological processes such as biological washout, in which metabolic activity and blood perfusion cause the redistribution of positron-emitting isotopes away from their production sites. These effects influence the accuracy of the measured PET signal in relation to the actual dose administered to the target.

The correlation between PET signal and physical dose depends significantly on the projectile type. For instance, protons only produce positron emitters through target fragmentation, resulting in an activity distribution that is poorly correlated spatially with the Bragg peak. In contrast, heavier ions such as ^{12}C or ^{16}O produce positron emitters from both target and projectile fragmentation, leading to better correlated activity profiles with respect to the Bragg peak position, as illustrated in Figure 1.2. This discrepancy complicates the direct translation of PET signals into dose maps, necessitating the integration of predictive models such as Monte Carlo simulations. By leveraging these models and simulations, PET-based verification provides a non-invasive means to assess ion beam range and verify dose delivery accuracy [13].

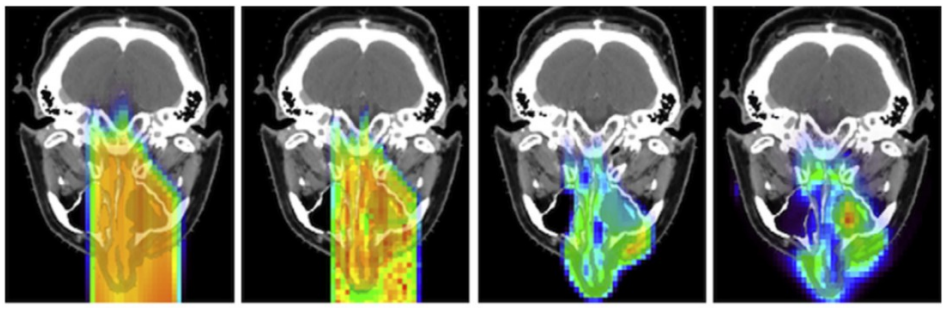

Figure 1.3: From left to right: Planned Dose, Monte Carlo predicted dose, Monte Carlo predicted PET activity distribution, measured PET activity distribution [15].

Figure 1.3 illustrates a typical PET-based range verification workflow. By comparing

the measured PET activity distribution with Monte Carlo predictions based on the treatment plan, deviations in beam range or unexpected anatomical changes can be detected.

PET Imaging Modalities for Ion Beam Therapy

PET-based range verification can be performed using different imaging strategies:

- **In-beam PET**: Imaging is carried out during irradiation, enabling quasi-real-time monitoring of beam range and minimizing the impact of biological washout. Despite its advantages, this modality presents significant technical challenges due to interference from prompt gamma radiation and the need for specialized, radiation-hardened detector systems [13].
- **In-room PET**: Imaging is performed immediately after irradiation, allowing acquisition of activity distributions before prolonged physiological redistribution occurs. This approach requires the installation of dedicated PET scanners in the treatment room [11].
- **Offline PET**: Imaging is typically initiated within minutes after irradiation, using standard PET/CT scanners located outside the treatment room. While this approach is widely accessible, it is more susceptible to biological washout and patient repositioning, potentially compromising the accuracy of the reconstructed activity distributions [13].

Despite the clinical feasibility and non-invasive nature of PET-based range verification, its accuracy remains limited by physiological and physical factors such as biological washout, tissue heterogeneity, and the complexity of nuclear fragmentation pathways. Continued development of predictive models, improved detector technology, and optimized acquisition protocols are essential to enhance the reliability and clinical adoption of this method in particle therapy.

1.3 SIRMIO Project

Building upon the discussion of ion beam therapy and its associated challenges, it becomes evident that improving range verification techniques is essential to maximizing its clinical efficacy. Addressing these limitations in preclinical studies is a critical step towards refining treatment strategies and enhancing therapeutic precision. The SIRMIO project (Small Animal Proton Irradiator for Research in Molecular Image-guided Radiation-Oncology) at LMU was established with this goal in mind. As stated

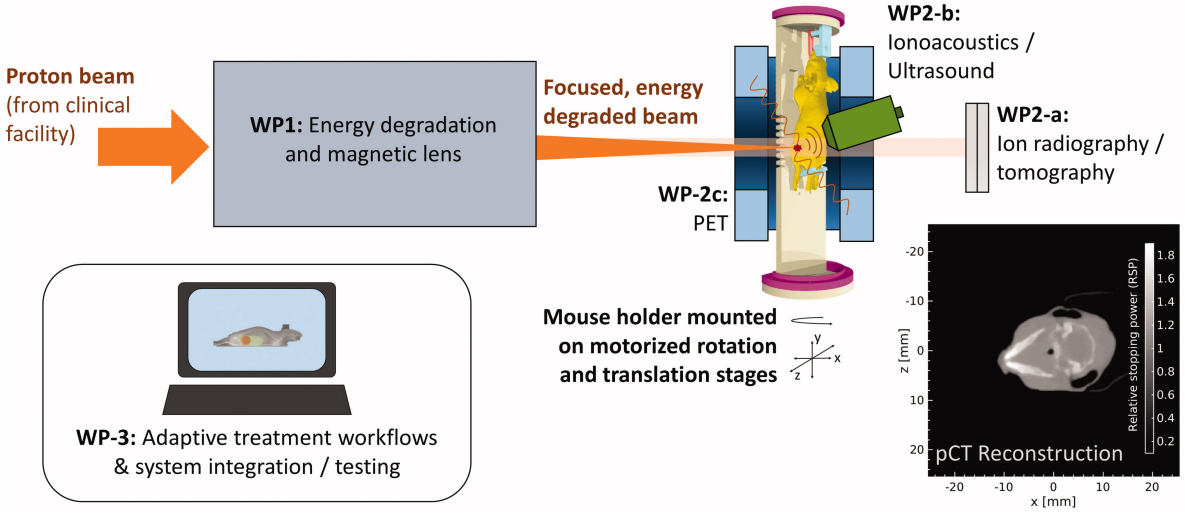

Figure 1.4: Outline of the work-packages (WPs) of the SIRMIO project: (1) beamline degrading and focusing the incoming clinical proton beam, (2) pre-treatment ion transmission imaging (WP2-a), (3) ionoacoustics/US (WP2-b), and (4) PET systems for in-vivo treatment verification (WP2-c), (5) system integration for treatment adaptation relying on pre-treatment proton CT images [16].

in [16], "SIRMIO aims at realizing and demonstrating an innovative portable prototype system for precision image-guided small animal proton irradiation, suitable for installation at existing clinical treatment facilities." The project integrates precise dose delivery with advanced anatomical image guidance and in vivo treatment verification, leveraging proton computed tomography (pCT) and ultrasound imaging for anatomical mapping, and ionoacoustics and positron emission tomography (PET) for range verification.

The project is structured into five interconnected work-packages, illustrated in Figure 1.4, each addressing key aspects of the system development. The main focus of this thesis is the PET scanner component, emphasizing its current state of the art and the challenges it seeks to overcome within the SIRMIO framework.

The project consists of five interdependent work-packages, detailed below:

- **Beamline:** This work package focuses on adapting and fine-tuning a clinical proton beamline for small animal irradiation. It ensures precise control of beam energy degradation, focusing, and monitoring to meet the spatial accuracy requirements for preclinical studies.

- **Mouse Holder:** A specialized positioning system that guarantees reproducible placement and immobilization of the subject during irradiation.

- **Pre-Treatment Imaging:** This includes proton radiography and computed tomography (pCT) imaging to acquire anatomical and tissue composition informa-

tion before irradiation. These modalities improve range accuracy by providing essential input for treatment planning.

- **Treatment Planning:** Based on pre-treatment imaging, this package is responsible for optimizing dose delivery, ensuring accurate treatment plans that account for tissue heterogeneities and anatomical variations.
- **In-Vivo Range Verification:** This package integrates PET and ionoacoustic imaging to monitor beam range in quasi-real time. By detecting positron-emitting isotopes generated within irradiated tissues, PET provides a non-invasive means of assessing ion beam range.

Among these, the PET scanner is the primary focus of this thesis and will be explored in detail in Chapters 3 and 4, covering its design, data acquisition methods, and performance evaluation.

1.4 Objective and Structure of the Thesis

This thesis focuses on the modeling and characterization of the detector response of an in-beam PET scanner developed within the SIRMIO project. The main objective is to analyze the detector behavior at the pixel level, using both experimental and simulation data, to support improvements in image quality and reconstruction accuracy.

The structure of the thesis is as follows:

- **Chapter 2: Theoretical Background**
  Provides an overview of fundamental physical principles relevant to photon detection and PET imaging.
- **Chapter 3: SIRMIO PET Scanner Overview**
  Introduces the PET scanner and its role in the SIRMIO project.
- **Chapter 4: Materials and Methods**
  Describes the experimental setup and basic simulation tools used.
- **Chapter 5: Data Processing**
  Outlines the main data analysis and pixel modeling strategies.
- **Chapter 6: Data Analysis, Results and Discussion**
  Presents the results of the detector characterization and evaluates the model's performance.
- **Chapter 7: Conclusions**
  Summarizes the findings and discusses future perspectives.

Chapter 2

Theoretical Background

This chapter explores the fundamental physical principles that govern photon interactions with matter, with a particular emphasis on γ-ray detection mechanisms. Given the focus of this research on modeling the PET detector response, the discussion will not cover the interaction of charged particles with matter. While such interactions are relevant to PET-based range verification, they fall beyond the direct scope of this study. Readers seeking a more comprehensive treatment of such topics could refer to [17].

2.1 Photon Interaction with Matter

The interaction of photons with matter is a fundamental process in medical imaging and radiation physics. In particular, X-rays and γ-rays play a crucial role in nuclear reactions and diagnostic imaging techniques. In the context of this research, the focus lies on γ-ray production and its interaction with matter, as these phenomena are central to PET-based imaging. γ-radiation is defined as high-energy electromagnetic radiation emitted from nuclear processes, in contrast to X-rays, which originate from atomic transitions. These emissions predominantly arise from nuclear de-excitation events or positron-electron annihilation, with energies typically ranging from 100 keV to several tens of MeV [15].

Photon Attenuation Description

The propagation of photons through matter is governed by probabilistic interactions. Unlike charged particles, which lose energy continuously along their path via multiple small interactions, photons undergo discrete stochastic events that result in abrupt changes in their energy and direction. These interactions lead to attenuation of the photon beam as it traverses a medium, following an exponential decay law:

$$N(x) = N_0 e^{-\mu(E_\gamma, Z)x}, \tag{2.1}$$

where $N(x)$ is the number of photons remaining after traveling a distance x, N_0 is the initial number of photons, and $\mu(E_\gamma, Z)$ is the linear attenuation coefficient, which depends on the photon energy E_γ and the atomic number Z of the material.

The linear attenuation coefficient μ quantifies the probability of interaction per unit path length and is influenced by:

- The microscopic cross-section σ, which characterizes the probability of photon interaction per target nucleus.
- The nuclear density, expressed as $n = \rho\frac{N_A}{A}$, where ρ is the mass density of the material, N_A is Avogadro's number, and A is the atomic mass number.

These lead to the relationship:

$$\mu = \sigma\rho\frac{N_A}{A}, \tag{2.2}$$

where σ is the total microscopic cross-section for photon interactions. In the energy range relevant to medical imaging and therapy (typically 10 keV to several MeV), the dominant photon interaction processes are:

$$\sigma = \sigma_{\text{photoelectric}} + \sigma_{\text{Compton}} + \sigma_{\text{pair}}. \tag{2.3}$$

Here:

- $\sigma_{\text{photoelectric}}$ corresponds to the photoelectric effect, dominant at low photon energies and in high-Z materials.
- σ_{Compton} describes incoherent scattering with atomic electrons, which predominates at intermediate energies.
- σ_{pair} accounts for pair production, relevant at energies above 1.022 MeV in the field of a nucleus.

For completeness, other interaction mechanisms such as **Rayleigh (coherent) scattering** and **photonuclear reactions** also contribute to photon attenuation. Rayleigh scattering involves elastic interactions with bound electrons and is significant mainly at low photon energies and small-angle scattering, but its contribution to energy deposition is negligible. Photonuclear interactions, in which the photon is absorbed by the nucleus causing nuclear excitation or particle emission, occur at higher energies (typically above 10 MeV) and are thus not relevant within the standard PET and diagnostic imaging energy range.

To account for variations in material density and facilitate comparisons across different substances, the attenuation coefficient is often normalized to yield the **mass attenuation coefficient**:

$$\mu_{\text{mass}} = \frac{\mu}{\rho}, \tag{2.4}$$

which expresses attenuation per unit mass and allows a more universal description of photon interaction behavior in matter.

2.1.1 Photon Interaction Mechanisms

Photons interact with matter through different mechanisms depending primarily on their energy and the atomic number (Z) of the absorbing material. The three principal interaction mechanisms within the energy range relevant to radiation physics and medical applications are the photoelectric effect, Compton scattering, and pair production.

Photoelectric Effect

The photoelectric effect is a fundamental photon interaction mechanism that dominates at low photon energies, particularly in materials with a high atomic number (Z). In this process, an incident photon is completely absorbed by an atom, transferring all its energy to an electron, which is subsequently ejected from the atom, leading to ionization, as illustrated in Figure 2.1).

The photoelectric effect occurs when the energy of the incident photon exceeds the binding energy of the electron in one of the atomic shells. This interaction occurs predominantly for inner shell electrons (e.g., K and L shells), as their higher binding energies increase the likelihood of photon absorption. The probability of absorption is further enhanced for high-Z materials due to their higher electron density and stronger electromagnetic interaction [17] with incident photons, as shown in Figure 2.7. A characteristic of this process is the sharp increase in absorption probability when the photon energy exceeds the binding energy of an atomic shell, for K-shell interaction known as the K-edge effect, as illustrated in Figure 2.8.

Following the ejection of a core electron, the atom remains in an excited ionized state and undergoes electronic rearrangement to restore equilibrium. This process results in the emission of secondary radiation in one of two forms:

- Characteristic X-ray Emission: The vacancy left in the inner shell is filled by an electron from a higher energy shell. The excess energy from this transition is emitted as a characteristic X-ray, with energy corresponding to the difference between the two electron shells.

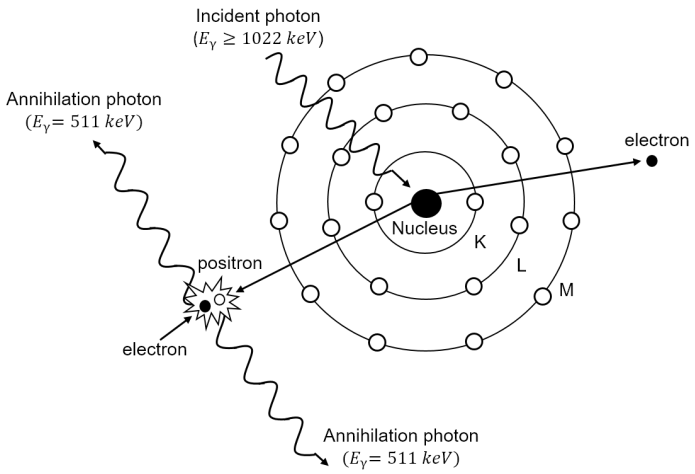

Figure 2.1: Illustration of the photoelectric effect, where the incident photon is fully absorbed and an electron is ejected [15].

- **Auger Electron Emission**: Instead of emitting an X-ray, the transition energy can be transferred to another bound electron, which is subsequently ejected from the atom as an Auger electron. This process can initiate a cascade of further Auger emissions, leaving the atom in a multiply ionized state.

The kinetic energy of the emitted photoelectron is given by:

$$E_e = E_\gamma - E_b \tag{2.5}$$

where E_b is the binding energy of the electron. The probability of photoelectric absorption follows an approximate empirical relationship:

$$\sigma_{ph} \propto \frac{(Z)^n}{(E_\gamma)^m} \tag{2.6}$$

where $n \approx 4 - 5$ and $m \approx 3.5$. This dependency highlights the strong preference for photoelectric absorption in high-Z materials, making it a crucial process in photon detection. A key advantage of the photoelectric effect is the precise localization of energy deposition, as the emitted photoelectron remains near the photon interaction point. This contrasts with other process like Compton scattering, where the scattered photon may travel further before depositing energy. This characteristic enhances spatial resolution in photon detectors, making the photoelectric effect particularly valuable for imaging applications.

Compton Scattering

Compton scattering is a fundamental photon interaction mechanism in the MeV energy range, making it especially relevant in medical photon detector. As illustrated in

Figure 2.2, this process occurs when an incident photon undergoes an inelastic collision with an atomic electron, transferring part of its energy to the electron, which is ejected from the atom. The photon is scattered at an angle (θ) with reduced energy, while the remaining energy is carried by the scattered electron.

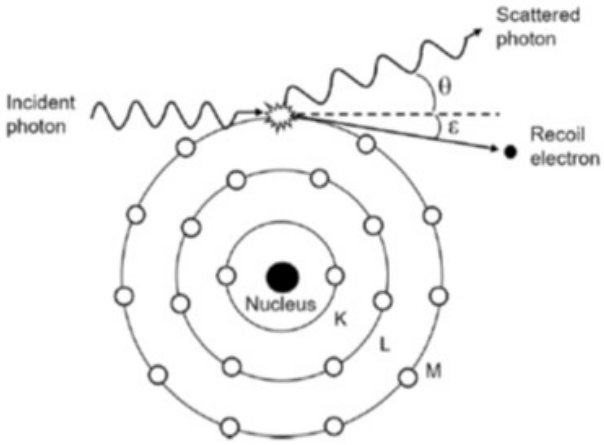

Figure 2.2: Schematic representation of Compton scattering [15].

The extent of energy transfer depends on the scattering angle, influencing the photon's trajectory and the kinetic energy of the ejected electron. The energy of the scattered photon E'_γ is given by the Compton formula:

$$E'_\gamma = \frac{E_\gamma}{1 + \frac{E_\gamma}{m_e c^2}(1 - \cos\theta)} \tag{2.7}$$

where E_γ is the initial photon energy, m_e is the mass of the electron and θ is the scattering angle. From Eq. (2.7), the kinetic energy of the recoiling electron, derived from energy conservation, is:

$$E_e = E_\gamma - E'_\gamma = E_\gamma \frac{\left(\frac{E_\gamma}{m_e c^2}\right)(1 - \cos\theta)}{1 + \left(\frac{E_\gamma}{m_e c^2}\right)(1 - \cos\theta)} \tag{2.8}$$

In this formulation, the electron binding energy is neglected, as it is small compared to the photon and electron kinetic energies.

The electron kinetic energy varies from 0 (when $\theta = 0$) to a maximum at $\theta = \pi$ (backscatter). However, the maximum kinetic energy never equals the incident photon energy, meaning complete photon absorption does not occur [18]. This characteristic results in the distinctive shape of the electron energy spectrum, terminating at what is known as the *Compton edge*, corresponding to the maximum energy transferable to the electron, as reported in Figure 2.3.

The Klein-Nishina formula describes how the probability of photon scattering varies with angle and photon energy. As shown in Figure 2.4, forward scattering becomes

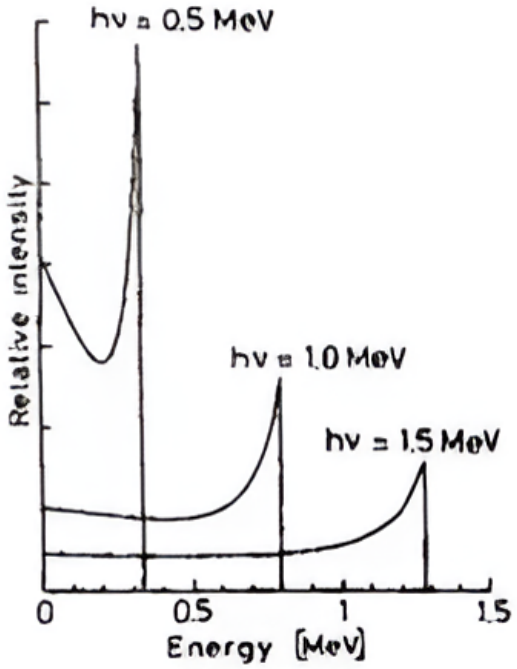

Figure 2.3: Energy distribution of recoil electrons showing the characteristic Compton Edge [14].

increasingly probable with higher photon energies [17].

The differential cross-section for Compton scattering is given by:

$$\frac{d\sigma}{d\Omega_\varphi} = \frac{r_e^2}{2}\left[\frac{1}{(1+\gamma(1-\cos\theta))^2}\right]\left(1+\cos^2\theta+\frac{\gamma^2(1-\cos\theta)^2}{1+\gamma(1-\cos\theta)}\right), \tag{2.9}$$

where r_e is the classical electron radius and $\gamma = E_\gamma/m_e c^2$. Integrating this formula over $d\Omega$ yields the total probability per electron for a Compton scattering event.

The Compton cross-section varies strongly with photon energy, particularly in the 100 keV to several MeV range. While conventional PET primarily involves 511 keV photons from positron annihilation, in-beam PET systems must also account for high-energy background from prompt gamma radiation, which can reach several MeV and significantly influence Compton scattering contributions.

The total Compton cross-section σ^c consists of two components: the Compton scattered σ^s and the Compton absorption σ^a cross-sections. The Compton scattered cross-section represents the fraction of total energy contained in the scattered photon, whereas the absorption cross-section corresponds to the average energy transferred to the recoil electron, which is absorbed by the material as the electron is stopped within it [14].

The absorbed cross-section can be determined from the Klein-Nishina formula as:

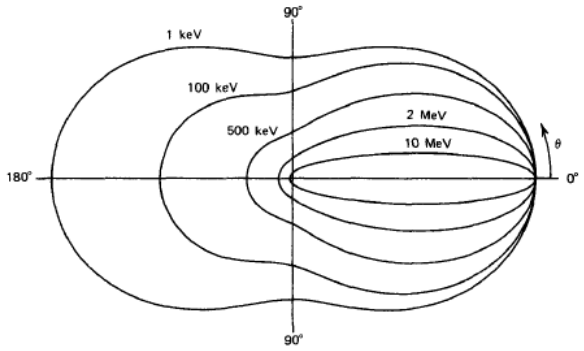

Figure 2.4: Polar plot of the number of photons (incident from the left) Compton scattered into a unit solid angle at the scattering angle θ. The curves correspond to different initial photon energies [17].

$$\sigma^a = \int_\Omega \frac{d\sigma}{d\Omega} d\Omega_\varphi = \int_\Omega \frac{d\sigma}{d\Omega} \frac{E_\gamma - E'_\gamma}{E_\gamma} d\Omega_\varphi. \tag{2.10}$$

The shape of the cross-section as a function of the energy of the incident photon is illustrated in Figure 2.5. Compton scattering dominates at photon energies of the order of $E_\gamma \sim$ MeV.

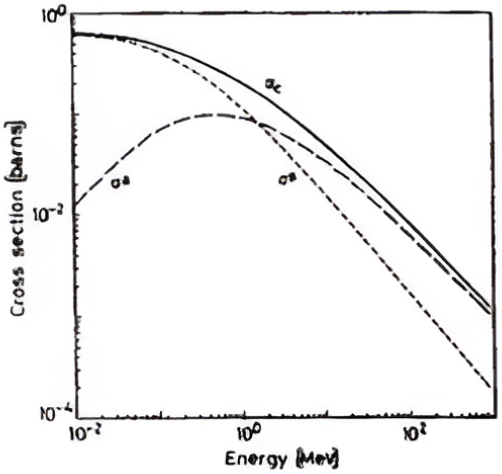

Figure 2.5: Total Compton effect cross-section given by the sum of the Compton scattered σ^s and Compton absorbed σ^a cross-sections [18] [14].

Following its initial interaction, the scattered photon often undergoes subsequent Compton scattering interactions with nearby atoms, continuing this process until it either loses all its energy or undergoes photoelectric absorption. This sequential scattering significantly affects photon transport in matter, influencing the design of radiation detectors and shielding materials.

Unlike the photoelectric effect, where energy deposition is localized, Compton scattering results in a distributed energy transfer, as the scattered photon may travel further before depositing additional energy. This characteristic influences spatial resolution in photon detectors, often necessitating corrections in imaging applications.

Pair Production

Pair production is the third principal interaction mechanism between gamma rays and matter. As illustrated in Figure 2.6, this process occurs in the intense Coulomb field of an atomic nucleus and becomes energetically possible when the incident photon energy exceeds the threshold of twice the electron rest mass energy:

$$E_\gamma > 2m_e c^2 = 1.022 \text{ MeV}. \tag{2.11}$$

Above this threshold, a pair production process could happen in which the photon is completely absorbed and converted into an electron-positron pair, satisfying both energy and momentum conservation. However, the probability of this process occurring is relatively low until the incident γ-ray energy reaches several MeV, as shown in Figure 2.7. The excess energy beyond 1.022 MeV is distributed as kinetic energy between the produced particles [17]:

$$E_{e^-} + E_{e^+} = E_\gamma - 2m_e c^2. \tag{2.12}$$

Since a free photon cannot simultaneously satisfy both energy and momentum conservation, the presence of a nucleus is required to absorb the recoil momentum. This process is more probable in high-Z materials due to their stronger electromagnetic fields, which facilitate momentum conservation [17].

In addition to pair production in the field of a nucleus, the process can also occur—though with much lower probability—in the Coulomb field of an atomic electron. This variant, known as triplet production, results in the photon being converted into an electron-positron pair, while the recoil is absorbed by the interacting electron itself. Because three particles are present in the final state, the threshold energy for this process is higher:

$$E_\gamma > 4m_e c^2 = 2.044\,\text{MeV}. \tag{2.13}$$

Triplet production is less probable due to the smaller mass and lower binding of the electron compared to the nucleus, but becomes non-negligible at high photon energies.

The positron produced in the pair production process is not a stable particle. After losing its kinetic energy in the absorbing medium, it undergoes annihilation with a nearby electron. This results in the emission of two back-to-back annihilation photons, each carrying an energy of 0.511 MeV:

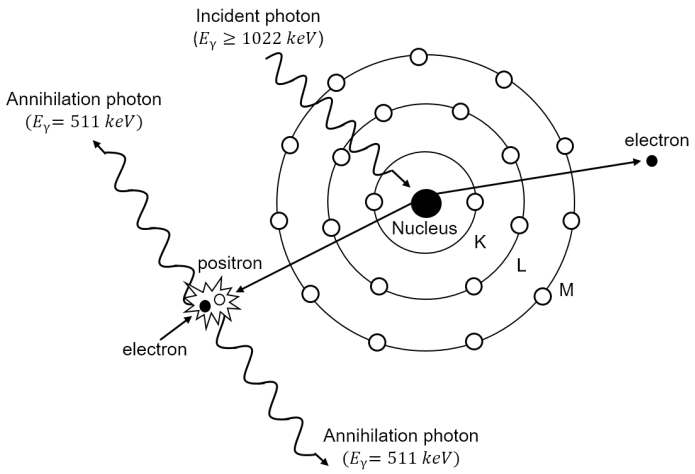

Figure 2.6: Pair production mechanism: a high-energy photon creates an electron-positron pair in the presence of a nucleus [15].

$$e^+ + e^- \rightarrow 2\gamma \quad (0.511 \text{ MeV each}). \tag{2.14}$$

Due to the short thermalization time of the positron, the annihilation radiation is emitted nearly simultaneously with the original pair production interaction, making this a rapid two-step process.

The probability of pair production increases with both photon energy and the atomic number Z of the absorbing material. At photon energies just above 1.022 MeV, the process is relatively rare compared to Compton scattering and the photoelectric effect. However, as photon energy increases, pair production becomes increasingly dominant, surpassing the other interaction mechanisms at approximately 6 MeV [15]. The approximate dependence of the pair production cross-section is given by:

$$\sigma_{\text{pair}} \propto Z^2 \ln(E_\gamma). \tag{2.15}$$

This energy dependency indicates that pair production is particularly significant in high-energy radiation interactions, influencing detector design, shielding materials, and applications such as high-energy radiotherapy.

2.1.2 Total cross-section and Interaction Dominance

The relative importance of photoelectric absorption, Compton scattering, and pair production varies significantly depending on the energy of the incident photon and the atomic number (Z) of the absorbing material. As illustrated in Figure 2.7, different interaction mechanisms dominate across distinct energy ranges, defining three principal regions of photon interaction.

At low photon energies, photoelectric absorption dominates, especially in high-Z materials, as its probability scales strongly with atomic number. As energy increases, its likelihood decreases, giving way to Compton scattering, which prevails in the MeV range, where photons undergo inelastic collisions with atomic electrons, transferring partial energy. At high photon energies ($E_\gamma > 1.022MeV$), pair production becomes significant, occurring in the Coulomb field of the nucleus and increasing rapidly with photon energy, particularly in high-Z materials due to stronger nuclear fields. These transitions between interaction mechanisms are clearly indicated in Figure 2.7.

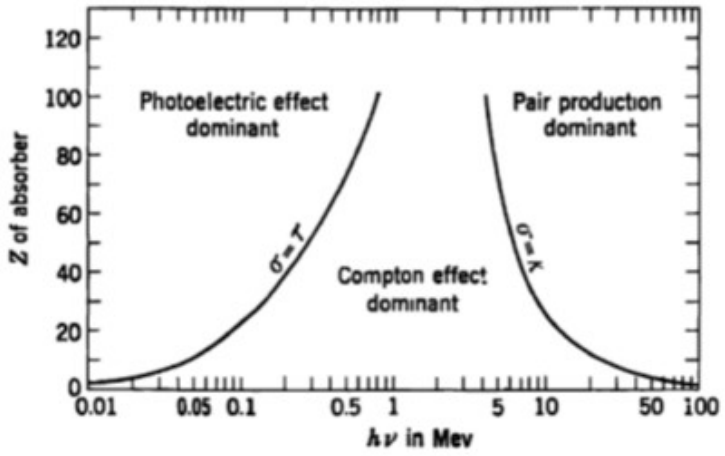

Figure 2.7: Relative importance among photoelectric absorption, Compton scattering, and pair production as a function of the absorber atomic number and photon energy [17].

Since photon interactions with matter are probabilistic, the total cross-section for photon attenuation in a given material is the sum of contributions from all three processes. The total mass attenuation coefficient, μ/ρ, is given by:

$$\frac{\mu}{\rho} = \frac{N_A}{A} \sum_i \sigma_i, \tag{2.16}$$

where N_A is the Avogadro number, A is the atomic mass, and σ_i represents the individual cross-sections of each interaction process.

The variation of the total mass attenuation coefficient as a function of photon energy is shown in Figure 2.8. The plot highlights the characteristic K-edges where photoelectric absorption increases sharply, as well as the energy-dependent transitions between dominant interaction mechanisms.

In summary, photon interactions are governed by a combination of energy-dependent mechanisms, understanding these processes is crucial for applications in radiation detection, medical imaging, and medical treatment.

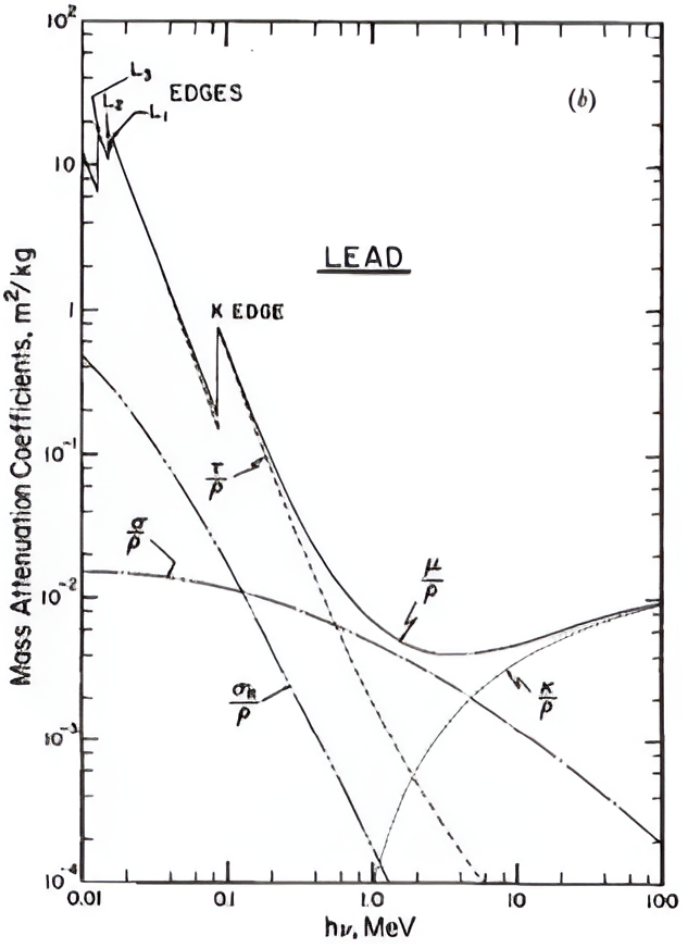

Figure 2.8: Total mass attenuation coefficient in lead as a function of the energy of the incoming photon [19].

2.2 γ-ray Detection Systems

γ-ray detection is fundamental in medical imaging and nuclear physics, particularly in applications such as Positron Emission Tomography (PET). Since gamma rays are uncharged and interact indirectly with matter, their detection relies on the generation of secondary ionizing particles, primarily electrons. This necessitates the use of specialized detectors capable of converting γ-ray energy into measurable signals.

An effective γ-ray detection system must fulfill two primary functions:

1. Ensuring sufficient interaction probability between incoming photons and the detector medium to generate detectable secondary signals (electrons)

2. efficiently capturing and processing these electrons for subsequent collection and signal analysis

The performance of a γ-ray detector is evaluated based on several key parameters, including resolution, accuracy, sensitivity, and efficiency.

2.2.1 Key Characteristics of γ-ray Detectors

Resolution

Resolution refers to a detector's ability to differentiate between similar measurement values. In γ-ray detection, resolution is categorized into three main types:

- Energy Resolution: Determines the detector's capability to distinguish gamma rays of different energies. It is often quantified using the Full Width at Half Maximum (FWHM) of a detected energy peak. A lower FWHM indicates superior resolution, which is essential for spectroscopic applications.
- Spatial Resolution: Defines the minimum distance at which two separate γ-ray interactions can be distinguished. This parameter is critical for imaging applications such as PET, where precise localization of radiation sources is required.
- Time Resolution: Represents the ability to differentiate events occurring within short time intervals. In coincidence detection methods, such as those used in PET imaging, superior time resolution enables more precise reconstruction of γ-ray emission points.

Accuracy

The accuracy of a γ-ray detector describes how closely the measured values match the actual physical parameters of the radiation being observed. Unlike resolution, which pertains to distinguishing similar values, accuracy ensures that the recorded data reliably reflect the true characteristics of the radiation source. Detector calibration, electronic noise reduction, and signal processing techniques significantly influence measurement accuracy.

Sensitivity

Sensitivity defines the detector's ability to register γ-ray interactions across a given energy spectrum. Several factors contribute to sensitivity:

- The composition and thickness of the detector material, which determine the probability of photon interaction.
- The efficiency of signal conversion processes, such as light emission in scintillators or charge generation in semiconductor detectors.
- Background noise suppression techniques, which enhance the signal-to-noise ratio and improve detection capability.

High sensitivity is particularly advantageous in low-dose imaging applications, where maximizing photon detection while minimizing radiation exposure is crucial.

Efficiency

Efficiency in γ-ray detection refers to the fraction of incident photons that successfully interact with the detector and contribute to measurable signals. It is typically divided into:

- Intrinsic Efficiency: The probability that an incoming gamma photon will undergo an interaction within the detector medium, generating a measurable response.
- Geometric Efficiency: The proportion of emitted gamma rays that reach the detector, influenced by the detector's size, shape, and positioning relative to the radiation source.

The total efficiency of a γ-ray detector can be expressed as [18]:

$$\epsilon_{\text{tot}} = \epsilon_{\text{intr}} \times \epsilon_{\text{geom}}. \tag{2.17}$$

Moreover, the energy deposition pattern can be used to classify detected events. While some photons are fully absorbed (resulting in a distinct photopeak), others undergo scattering and deposit only partial energy. A crucial metric in many applications is the photopeak efficiency, defined as the fraction of events in which the full γ-ray energy is absorbed.

As illustrated in Figure 2.9, the energy spectrum of photons interacting within a detector reveals a distinct photopeak on the right side of the distribution. The area under this peak represents the photopeak efficiency, which accounts for events where the full γ-ray energy is absorbed. In contrast, the total efficiency encompasses all detected events, including those where photons undergo partial energy deposition due to scattering.

In this thesis, we primarily focus on γ-ray detection systems that couple scintillators with photodetectors. The scintillator transforms γ-ray energy into light, which the photodetector subsequently converts into an electrical signal. Two commonly used photodetector technologies are:

- **Photomultiplier Tubes (PMTs)** – These devices use a series of dynodes to amplify weak light signals, offering high sensitivity and fast response times. PMTs are introduced in this work to illustrate the fundamental principles of photon-to-electrical signal conversion, providing a basis for comparison with alternative technologies.

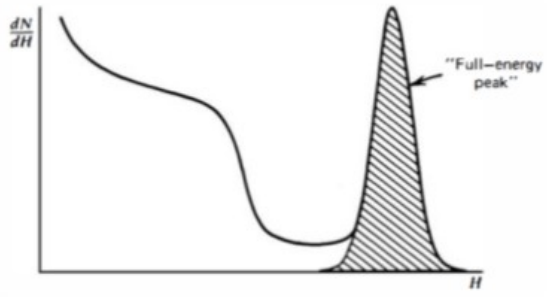

Figure 2.9: Full-energy peak for event discrimination [17]

- **Silicon Photomultipliers (SiPMs)** – Compact, semiconductor-based alternatives to PMTs that provide enhanced efficiency, robustness, and higher spatial resolution. Their smaller size makes them particularly suitable for applications with limited space, as in this thesis.

The selection of a suitable photodetector depends on application-specific requirements such as spatial resolution, timing accuracy, and operational constraints. In this work, PMTs are introduced to illustrate the fundamental principles of photon-to-electrical signal conversion, providing a basis for understanding SiPMs. SiPMs are ultimately chosen for this project due to their compact design, which is crucial given the spatial limitations of our setup, as well as their superior efficiency and resolution.

2.2.2 Scintillators Detectors

Scintillators are materials that emit light upon interaction with ionizing radiation, making them essential for radiation detection across various fields, including medical imaging, particle physics, and security screening. Their functionality is based on the absorption of high-energy radiation, followed by de-excitation processes that result in the emission of visible or ultraviolet photons. These photons are subsequently detected using photomultiplier tubes (PMTs) or silicon photomultipliers (SiPMs), which convert the optical signal into an electrical pulse for further analysis [18].

Properties of Scintillators

An ideal scintillator should exhibit several key properties to ensure optimal performance:

- Light Yield: The number of scintillation photons emitted per unit of deposited energy. A high light yield enhances energy resolution [15].
- Energy Linearity: The light output should be directly proportional to the energy deposited by ionizing radiation.

- Transparency: Optical transparency at the emission wavelength is crucial for efficient photon collection.

- Decay Time: Short decay times enable rapid response and high count-rate capability.

- Mechanical and Chemical Stability: Scintillators must be durable and chemically stable under operational conditions [18].

Scintillators can be broadly classified based on their composition:

- Organic Scintillators: These rely on molecular transitions to emit light upon excitation. They exist in solid, liquid, or vapor forms and are known for their fast response times (1–2 ns). Plastic scintillators, a subcategory, are widely used due to their mechanical robustness and ease of fabrication.

- Inorganic Scintillators: These function through electronic transitions within a crystalline lattice. Compared to organic scintillators, they have a higher density and atomic number, providing greater stopping power and higher light yield. However, they exhibit longer decay times (hundreds of nanoseconds) but offer superior energy resolution, making them ideal for γ-ray spectroscopy.

An example of Inorganic scintillator is Lutetium-Yttrium Oxyorthosilicate (LYSO:Ce) it is the scintillator used in the PET scanner discussed in this thesis. LYSO is favored for its high density (7.1 g/cm^3), fast decay time (40 ns), and excellent radiation hardness, making it ideal for detecting gamma rays in medical imaging applications [18]. Its superior timing resolution and light yield contribute to enhanced spatial and energy resolution in PET systems, ensuring precise detection of annihilation photons. A more detailed discussion of its implementation in the PET scanner used in this research is provided in Chapter 4.

2.2.3 Photomultiplier Tubes Detector

Photomultiplier tubes (PMTs) are critical components in radiation detection systems, particularly in applications requiring high sensitivity to low-light levels. They convert scintillation photons into electrical signals through the photoelectric effect, followed by electron amplification via a cascade process.

A PMT functions by converting incident photons into photoelectrons at a photosensitive cathode, known as the *photocathode*. These photoelectrons are subsequently multiplied through a series of dynodes, leading to a substantial electrical signal [17].

A schematic representation of a typical PMT structure is shown in Figure 2.10, illustrating the sequential electron multiplication process. The essential components of a PMT include:

- Input Window: Allows incident photons to reach the photocathode.
- Photocathode: Converts photons into electrons via the photoelectric effect.
- Focusing Electrodes: Direct the emitted electrons toward the dynodes.
- Electron Multiplier (Dynodes): A series of electrodes at progressively higher voltages that amplify the electron signal through secondary emission.
- Anode: Collects the amplified electrons and converts them into an output current for further processing.

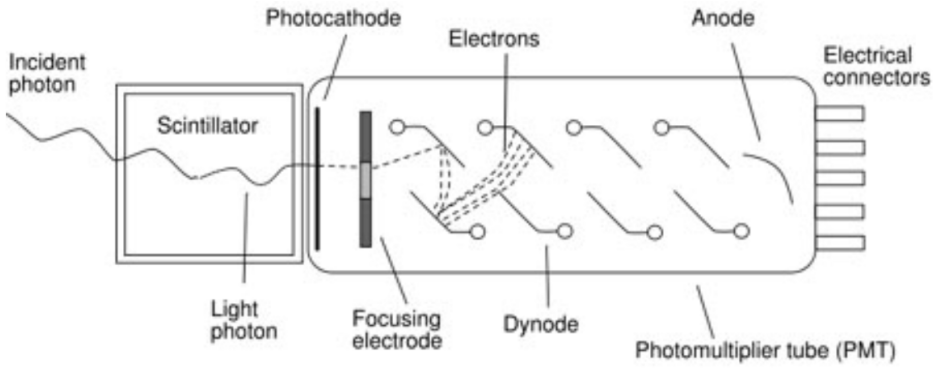

Figure 2.10: Illustration of the internal structure of a photomultiplier tube, adapted from [17].

The performance of PMTs is primarily characterized by two fundamental parameters: *quantum efficiency* and *gain*.

Quantum efficiency (η) represents the probability of photoelectron emission per incident photon and is defined as:

$$\eta(\nu) = (1 - R) \cdot P_\nu \cdot \frac{1}{1 + 1/kL} \cdot P_s \tag{2.18}$$

where:

- R is the reflection coefficient of the photocathode,
- P_ν represents the probability of photon absorption,
- kL accounts for the escape length and absorption coefficient of excited electrons,
- P_s is the probability of electron emission.

Higher quantum efficiency improves detector sensitivity, particularly in applications such as PET imaging and scintillation detection in ion beam therapy [15].

The amplification factor, or *gain*, of a PMT is achieved through secondary electron emission at each dynode stage. If each dynode amplifies the electron count by a factor δ, and there are n dynodes, the total gain (G) is expressed as:

$$G = \delta^n \tag{2.19}$$

Typical PMTs achieve gains ranging from 10^5 to 10^7, depending on the applied voltage and the number of dynodes [17].

From the gain and the number of dynodes, the initial number of emitted photoelectrons can be determined. Given the quantum efficiency, the number of scintillation photons can be estimated, which directly correlates with the energy deposited in the scintillator. Let n_e^i be the initial number of photoelectrons; then, the number of electrons outgoing from the last dynode will be $n_e^i \times \delta^m$, where m is the number of dynodes. These electrons are collected by an anode and transmitted to an external circuit for readout.

PMTs play a crucial role in medical imaging and radiation therapy monitoring. In PET scanners, they are coupled with scintillation crystals such as LYSO or $LaBr_3(Ce)$ to detect 511 keV annihilation photons with high temporal resolution. In ion beam therapy, PMTs are used in Compton camera systems to detect prompt gamma emissions, enabling real-time range verification [15].

Despite their advantages, PMTs have limitations, including sensitivity to magnetic fields, relatively large size, and mechanical fragility. Recent advancements in solid-state alternatives, such as silicon photomultipliers (SiPMs), offer potential solutions while maintaining similar detection capabilities [17].

2.2.4 Semiconducting detectors

Semiconductors are materials with electrical conductivity between conductors and insulators. Their electronic properties are defined by the presence of a bandgap, which separates the valence band (where electrons remain bound to atoms) from the conduction band (where free electrons contribute to electrical current).

Semiconductor detectors play a pivotal role in radiation detection due to their high energy resolution, compactness, and efficiency. They function by converting incident radiation into electrical signals through electron-hole pair generation in semiconductor materials, predominantly silicon (Si) and germanium (Ge). Compared to traditional photomultiplier tubes (PMTs), semiconductor detectors offer superior quantum efficiency, better scalability, and improved signal-to-noise ratios [18].

Semiconductors are classified into intrinsic and extrinsic types. Intrinsic semiconductors, such as high-purity silicon, have a natural equilibrium between electrons and holes but exhibit high electrical resistance, limiting charge collection efficiency. To enhance conductivity, semiconductors are doped with external elements to form extrinsic semiconductors.

Doping is achieved through::

- N-type doping: Incorporating group V elements (e.g., phosphorus, arsenic) introduces extra electrons, enhancing conductivity.
- P-type doping: Using group III elements (e.g., boron, aluminum) increases hole concentration, forming a positively charged material.

The junction of p-type and n-type materials results in a PN junction, the fundamental structure of most semiconductor detectors [15].

The PN Junction and Depletion Region

At the interface of p-type and n-type materials, electrons from the n-region diffuse into the p-region, while holes move in the opposite direction. This diffusion depletes the adjacent region of mobile charge carriers, forming a depletion layer that consists of immobile ionized dopant atoms. Figure 2.11 shows the resulting built-in electric field across this region prevents further diffusion and creates a potential barrier that influences charge carrier motion [18].

Applying an external reverse bias voltage increases the depletion width, further reducing capacitance and enhancing charge collection efficiency. This concept is central to PIN photodiodes, where an intrinsic (undoped) layer is introduced between the p- and n-regions to optimize carrier transport and improve bandwidth [20].

Semiconductor detectors operate based on the photoelectric effect and the generation of electron-hole pairs when ionizing radiation interacts with the material. The process unfolds as follows:

1. Energy deposition: Incident radiation (e.g., a photon or charged particle) interacts with the semiconductor, transferring energy to bound electrons.
2. Electron excitation: The imparted energy promotes electrons from the valence band to the conduction band, generating electron-hole pairs.
3. Charge separation: The built-in electric field in the depletion region accelerates the free electrons toward the n-region and holes toward the p-region, preventing recombination.

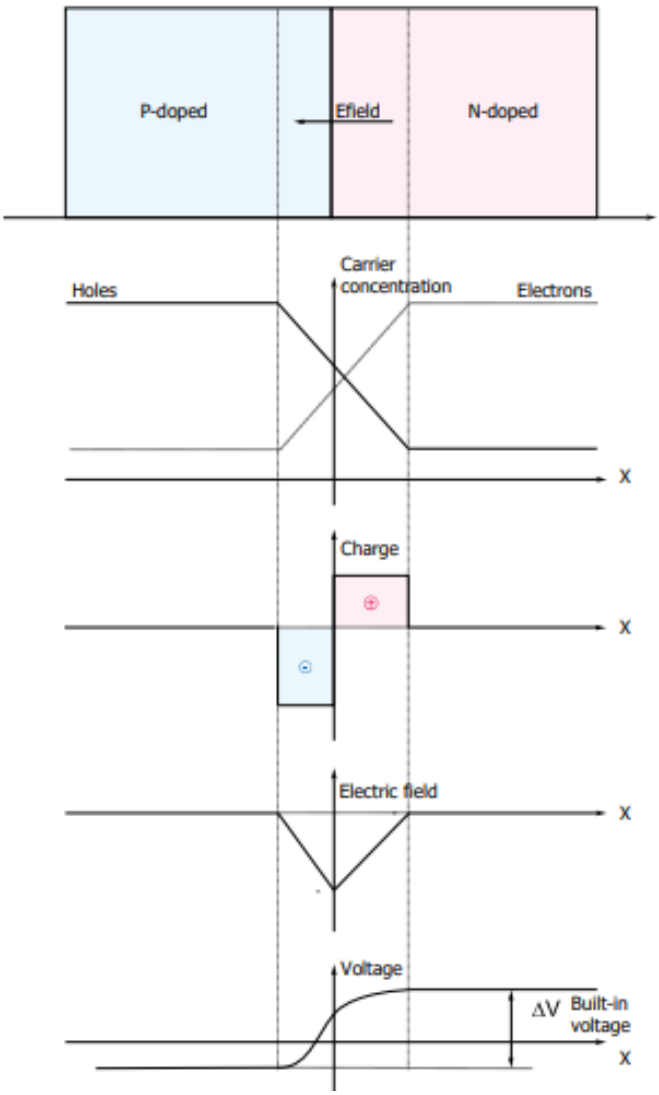

Figure 2.11: Equilibrium condition of a PN junction, depicting charge separation and electric field formation [18, 20].

4. Signal formation: The movement of charge carriers induces a current, which is subsequently amplified and processed for analysis.

Avalanche Photodiodes (APDs)

Avalanche Photodiodes (APDs) are highly sensitive semiconductor devices that operate under a strong reverse-bias voltage, creating an intense electric field within their depletion region. When an incident photon generates an electron-hole pair, the carriers are accelerated by the electric field, acquiring sufficient kinetic energy to undergo impact ionization.his process leads to an avalanche multiplication effect, amplifying the initial signal and thereby increasing the detector's sensitivity[20], as illustrated in Figure 2.12.

A key performance characteristic of APDs is their internal gain, which refers to the

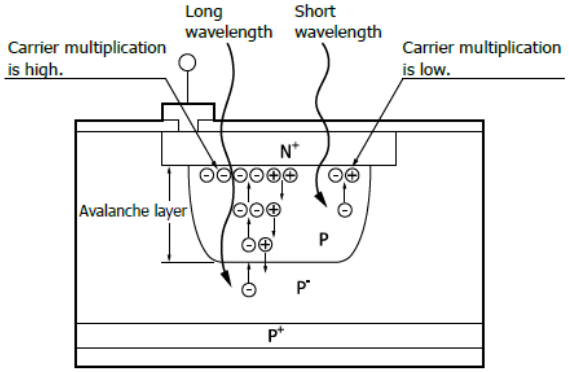

Figure 2.12: Structure of an avalanche photodiode, illustrating impact ionization and charge multiplication [20].

amplification factor of the generated charge carriers. However, this gain is not constant but depends on several factors, including the applied bias voltage, the incident light wavelength, and temperature variations. Additionally, the random nature of carrier collisions in the multiplication process introduces statistical fluctuations, leading to an excess noise factor that degrades the signal-to-noise ratio [17].

The gain-voltage response of an APD exhibits distinct operational regimes. At moderate bias voltages, the device operates in linear mode, where the gain increases steadily with voltage [20], as shown in Figure 2.13. However, as the bias voltage approaches the breakdown threshold, the device transitions into Geiger mode. In this regime, a single incident photon can trigger a self-sustaining avalanche, making Geiger-mode APDs particularly suited for single-photon detection. This property underlies the working principle of Silicon Photomultipliers (SiPMs), which consist of arrays of micro-APDs operating in Geiger mode.

Despite their high sensitivity, Geiger-mode APDs face a fundamental limitation: once an avalanche is triggered, the carrier density surges to levels that sustain a continuous current flow, rendering the device incapable of resolving discrete photon events. To address this issue, an external quenching circuit is employed. This circuit momentarily reduces the bias voltage below the breakdown threshold, suppressing the avalanche and restoring the APD to its initial state. However, during the quenching and recovery period, the APD remains inactive, leading to a dead time in detection. This limitation must be considered in applications requiring high photon count rates.

Silicon Photomultipliers (SiPMs)

Silicon Photomultipliers (SiPMs) were introduced to overcome the inherent limitations of Geiger-mode APDs—namely, dead time and lack of proportionality in output signal. SiPMs consist of an array of microcells, each functioning as an independent G-APD

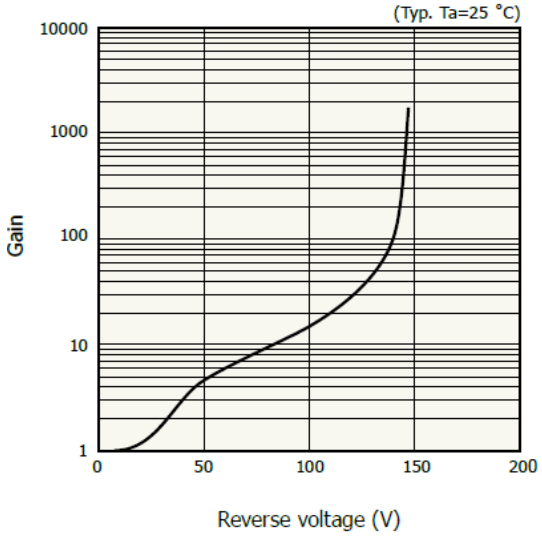

Figure 2.13: Plot of gain dependence on voltage [20].

with integrated quenching, allowing for high-resolution, high-efficiency photon counting in compact geometries-These microcells serve as independent photon counters: when a photon interacts with a microcell, it initiates an avalanche multiplication process, producing a fast, high-gain electrical pulse. As shown in Figure 2.14, all microcells are connected in parallel, enabling a collective output [15].

A key advantage of SiPMs is their ability to sum the signals from the individual microcells, creating a linear relationship between the output pulse amplitude and the number of detected photons. Although each microcell generates a fixed pulse regardless of the number of photons it absorbs, the total SiPM response reflects the number of simultaneously triggered microcells. Careful optimization of microcell dimensions is crucial to reduce the probability of multiple photon interactions within the same cell, preserving the SiPM's single-photon counting capability and ensuring excellent performance even in high-flux environments.

When coupled with scintillators, SiPMs can be used to reconstruct the energy of incident radiation. Scintillators convert the energy of incoming photons into a proportional number of visible photons, the yield of which depends on the scintillation material. By analyzing the number of activated microcells in an SiPM, the energy of the detected event can be inferred, making SiPMs particularly suitable for applications requiring precise energy resolution, such as positron emission tomography (PET) and time-of-flight PET (TOF-PET).

SiPMs offer several advantages over traditional photodetectors, including:

- High photon detection efficiency (PDE), enhancing sensitivity.
- Excellent timing resolution, crucial for fast photon counting applications.

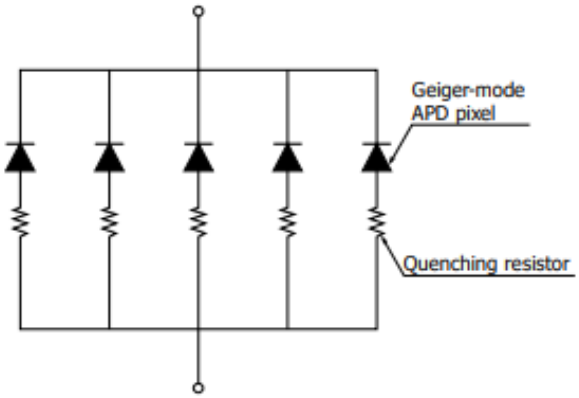

Figure 2.14: illustration of the SiPM circuit, consisting of a matrix of GAPD pixels connected in parallel [20].

- Immunity to magnetic fields, making them ideal for PET and TOF-PET applications [20].

These properties, combined with their compact size and robustness, have established SiPMs as a leading technology in modern photodetection systems, for this reason was selected for SIRMIO PET detector, as presented better in Chapter 4.

2.3 Radioactive Decay and Activity

Radioactive decay is a fundamental process wherein unstable atomic nuclei transition to more stable states by emitting energy in the form of particles or electromagnetic radiation. The number of undecayed nuclei, $N(t)$, at a given time t follows an exponential decay law:

$$N(t) = N_0 e^{-\lambda t} \tag{2.20}$$

where N_0 is the initial number of nuclei, and λ is the decay constant, representing the probability per unit time that a nucleus undergoes decay. The half-life, $t_{1/2}$, the time required for half of a given sample to decay, is given by:

$$t_{1/2} = \frac{\ln(2)}{\lambda} \tag{2.21}$$

A key parameter in radioactive decay is activity (A), defined as the number of disintegration per unit time, is expressed as:

$$A = \lambda N \tag{2.22}$$

The SI unit of activity is the Becquerel (Bq), defined as one nuclear disintegration per second. A more traditional unit, the Curie (Ci), is still commonly used in medical

and industrial applications, where

$$1\,\mathrm{Ci} = 3.7 \times 10^{10}\,\mathrm{Bq} \tag{2.23}$$

2.4 β^+ Decay

Beta-plus decay (β^+-decay) is a type of radioactive decay in which a proton inside the nucleus is converted into a neutron, emitting a positron (e^+) and a neutrino (ν_e):

$$p \rightarrow n + e^+ + \nu_e \tag{2.24}$$

This process occurs in proton-rich nuclei when the mass-energy difference between the parent and daughter nucleus is greater than 1.022 MeV, the combined rest energy of an electron and a positron. Unlike beta-minus decay, which results in an electron emission, beta-plus decay decreases the atomic number by one while conserving the total nucleon count [17].

The energy released in β^+-decay is shared between the emitted positron and the neutrino, leading to a continuous energy spectrum. The maximum positron energy varies depending on the isotope, ranging from hundreds of keV to several MeV. Because neutrinos escape detection due to their weak interaction with matter, only the positron energy can be measured experimentally [17].

Once emitted, positrons lose kinetic energy via interactions with surrounding electrons, ultimately leading to annihilation. This process produces two gamma photons:

$$e^+ + e^- \rightarrow 2\gamma \tag{2.25}$$

Each annihilation photon has an energy of 511 keV and is emitted nearly 180° apart, a property that is fundamental to positron emission tomography (PET) imaging [17]. PET scanners detect these coincident gamma rays, enabling precise localization of positron-emitting tracers, such as ^{18}F (fluorine-18) and ^{11}C (carbon-11), which are widely used in metabolic imaging and oncological diagnostics. The detection and reconstruction of these annihilation photons provide critical three-dimensional insights into biochemical processes in the body [15].

Chapter 3

SIRMIO PET work-package

The SIRMIO project (Small Animal Proton Irradiator for Research in Molecular Image-guided Radiation-Oncology), introduced in Section 1.3, is a multidisciplinary initiative aimed at developing a compact and versatile platform for precision proton irradiation in small animal models [16]. By combining advanced irradiation and imaging technologies, SIRMIO seeks to bridge the gap between preclinical radiobiological studies and clinical practice, enabling translational research under highly controlled conditions.

At the core of SIRMIO's design philosophy is the integration of high-resolution imaging modalities to support accurate, image-guided treatment delivery. Among these, **Positron Emission Tomography (PET)** plays a central role, as it is designed to meet the stringent requirements for in-beam treatment verification in small animal proton therapy. These include the ability to provide high spatial resolution, sensitivity to low levels of activity, and compatibility with real-time or quasi-real-time acquisition during irradiation [13, 18].

This chapter is dedicated to the PET work package of SIRMIO. It begins with a review of the fundamental principles of PET imaging and its role in ion beam range monitoring. Subsequently, it explores the specific challenges of implementing PET in an in-beam, small-animal context, focusing on technical limitations such as spatial resolution, detector design, and inter-crystal scattering. The chapter concludes by outlining the objectives of this thesis, which aims to develop and validate pixel-level characterization methods for PET detectors, thereby contributing to more accurate and robust range verification in proton therapy.

3.1 PET working principle

Positron Emission Tomography (PET) is a non-invasive imaging modality that enables visualization of metabolic and molecular processes by detecting the annihilation photons

resulting from positron-emitting radionuclides. These radionuclides, such as Fluorine-18, can either be injected into the subject as part of a radiotracer (as in conventional clinical PET imaging) or can originate from secondary radiation induced by external beams, such as protons or photons, as described in Chapter 2.

The fundamental physical process underlying PET imaging is the detection of two 511 keV photons emitted in nearly opposite directions (180° apart) following the annihilation of a positron with an electron. If these two photons are detected simultaneously (i.e., in coincidence) by opposing detectors, the annihilation event is assumed to have occurred somewhere along the line connecting the detectors. This line is known as the Line of Response (LOR). The spatial localization of the event is limited to the LOR, without precise knowledge of the position along it [18].

Figure 3.1 illustrates the schematic representation of $\beta+$ decay, which is detected by the PET detector ring, forming a LOR.

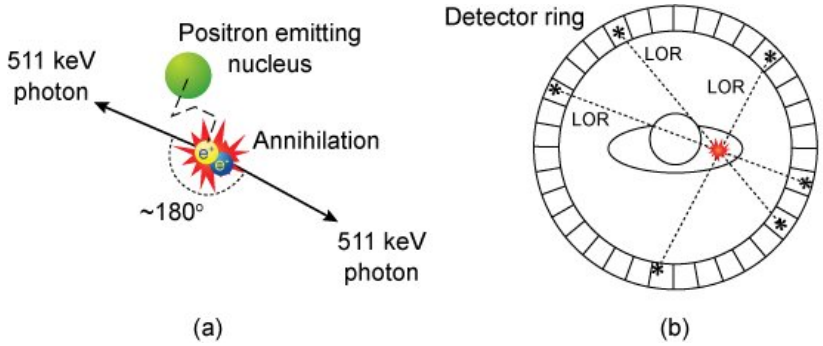

Figure 3.1: (a) Schematic of the positron annihilation process: a positron emitted from a radioactive nucleus annihilates with an electron, producing two 511 keV photons emitted nearly 180° apart. (b) Principle of PET detection: the annihilation photons are detected in coincidence by detectors arranged in a ring, defining a line of response (LOR) used for image reconstruction. [21].

PET scanners therefore consist of multiple detector elements arranged in rings to maximize the number of available LORs. This configuration allows simultaneous acquisition of many coincidence events across different angles and planes. The sensitivity and spatial resolution of PET strongly depend on the number of LORs within the scanner's Field of View (FOV), since more LORs lead to better sampling and lower statistical uncertainty in the reconstructed image [22].

To further improve axial sampling and sensitivity, multiple detector rings are often used, and coincidences can be detected not only within the same ring (direct coincidences) but also across rings (cross coincidences). The scanner configuration (e.g., the number of rings and the maximum ring difference allowed in coincidence detection) directly influences whether the acquisition is performed in 2D or 3D mode. In 2D PET,

axial septa are used to restrict coincidences to within single planes, limiting scatter and random events, whereas in 3D PET, these septa are removed, allowing for more coincidence detections and hence higher sensitivity, at the cost of increased scatter and more complex image reconstruction algorithms [22].

3.1.1 Image reconstruction

The raw data stream from the detectors includes all coincidence events, including true coincidences (from the same annihilation), random coincidences (from unrelated events), and scattered coincidences (where photons are deflected before detection). These events are time-stamped and mapped to detector pairs, producing massive datasets requiring systematic organization. The data are first sorted into sinograms, two-dimensional matrices where each pixel corresponds to a specific LOR defined by its angular orientation and displacement from the scanner center [23].

Before reconstruction, the raw sinogram data undergoes several critical preprocessing steps:

- Normalization correction accounts for variations in individual detector sensitivity and geometry.
- Attenuation correction compensates for the absorption or scattering of photons within the body, often using a transmission scan or CT data.
- Scatter correction removes scattered coincidences that falsely contribute to the image signal.
- Random coincidence correction subtracts the contribution from accidental (non-true) coincidences, often estimated using delayed coincidence window techniques.
- Dead-time and pile-up corrections adjust for detector performance limitations at high count rates [18].

Once corrections are applied, the sinograms are ready for image reconstruction. Early PET scanners employed analytical methods like filtered back projection (FBP), where each projection is mathematically back-projected across the image space, and a filter is applied to counteract the inherent blurring of the method. While fast, FBP is sensitive to noise and assumes idealized conditions, limiting its accuracy in complex scenarios.

Modern PET reconstruction relies on iterative algorithms, particularly Maximum Likelihood Expectation Maximization (ML-EM) and its accelerated form, Ordered Subsets Expectation Maximization (OSEM). These methods start with an initial estimate

of the radio-tracer distribution and iteratively refine it by comparing the measured sinograms with forward projections of the current estimate, using a system matrix that models the physical and geometric characteristics of the scanner. Each iteration updates the image estimate to maximize the likelihood of observing the measured data. Regularization techniques (such as smoothing constraints) and optimized stopping criteria are applied to prevent noise amplification and improve image stability [23].

Figure 3.2 shows the workflow of iterative image reconstruction, where the estimated tracer distribution is repeatedly updated by comparing simulated and measured data. Figure 3.3 illustrates how image quality improves with each iteration, though excessive iterations may introduce noise without proper regularization [18, 24].

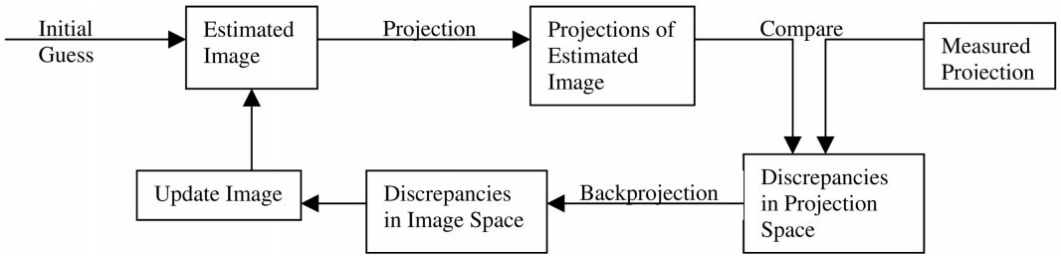

Figure 3.2: Iterative image reconstruction flow chart [24]

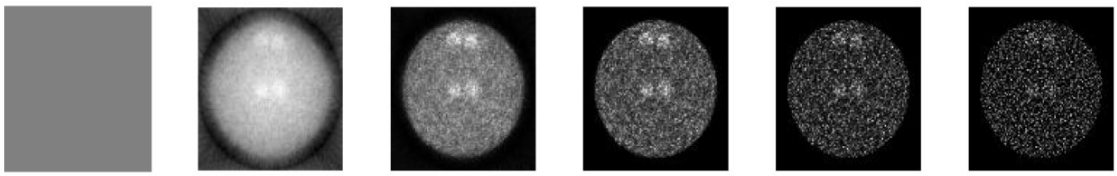

Figure 3.3: An example of iterative reconstruction. From left to right, the iteration number is increased, so that the noise [18, 24]

3.1.2 Problems and Limitations

Despite its high sensitivity and functional imaging capability, PET is subject to several physical and technological limitations that constrain spatial resolution and quantitative accuracy:

- **Detector size:** The resolution is primarily limited by the width of the scintillation crystals. The full width at half maximum (FWHM) blurring is approximately $d/2$, where d is the detector width. Reducing crystal size improves resolution but increases manufacturing complexity and the number of readout channels, raising cost and reducing detector efficiency due to the proportionally larger reflector volume [22].

- **Positron range:** Positron before annihilation travel for some millimiter depending on the positron energy and the materieale causing blurring [22].
- **Acollinearity:** Due to the residual momentum of positronium, annihilation photons deviate slightly from 180°, introducing additional blur. The effect increases with the diameter of the detector ring [22].
- **Decoding errors:** In systems using multiplexed readout electronics, some photons may be incorrectly assigned to adjacent crystals, lowering spatial precision [22].
- **Penetration effects:** High-energy photons may travel through several layers of the detector before interacting, particularly at oblique incidence angles. This effect, known as depth-of-interaction uncertainty, causes radial elongation of the image [22].
- **Sampling error:** Incomplete angular coverage or non-uniform detector geometry can result in poor image sampling, especially near the center of the field-of-view. This limits accurate quantification and introduces aliasing [22].
- **Statistical noise:** PET relies on stochastic decay events; low activity or short acquisition times yield noisy images. Iterative algorithms may amplify this noise unless carefully constrained [22].

Overall, while many of these limitations are rooted in fundamental physics (e.g., positron range, acollinearity), others can be reduced through improved hardware design, sophisticated reconstruction algorithms, and advanced correction methods. However, each improvement often comes with trade-offs in cost, complexity, or practicality, making careful optimization essential for clinical and preclinical PET systems.

3.1.3 Introduction to Inter-crystal Scattering (ICS)

After discussing the numerous challenges affecting the performance of PET imaging systems, one advanced strategy to overcome spatial resolution limitations is the use of multi-layer, pixelated detectors with depth-of-interaction (DOI) capability. This is a core design feature of the SIRMIO PET scanner. Broadly, the layered detector architecture improves the resolution and overall performance of the detector system by providing better event localization, making it essential for achieving the sub-millimeter resolution demanded in SIRMIO project.

However, even with DOI capability, an important physical challenge remains: the phenomenon of inter-crystal scattering (ICS). When a 511 keV annihilation photon enters the scintillator, it may undergo two main types of interactions. In the ideal case,

the photon is fully absorbed via the photoelectric effect, creating a single point of scintillation light that can be accurately localized. In practice, however, a large fraction of events undergo Compton scattering, where the photon deposits part of its energy in one crystal and is deflected into neighboring crystals before being absorbed. Studies report that, particularly in high-density, high-Z scintillators like LYSO, approximately 68% of interactions are Compton scatterings. These scattered photons can cross crystal boundaries, producing light in multiple detector elements and causing spatial misplacement of the event in the detector [25].

This leads to image blurring, reduced contrast recovery, and ultimately a degradation of spatial resolution. Recent research has quantified the impact of ICS on image contrast, showing reductions of up to 20% in hot-rod phantom studies [25].

Figure 3.4 shows how different photon interactions affect event localization. While photoelectric absorption enables accurate positioning, Compton scattering—especially across crystals—can mislead the event assignment and degrade spatial resolution [26].

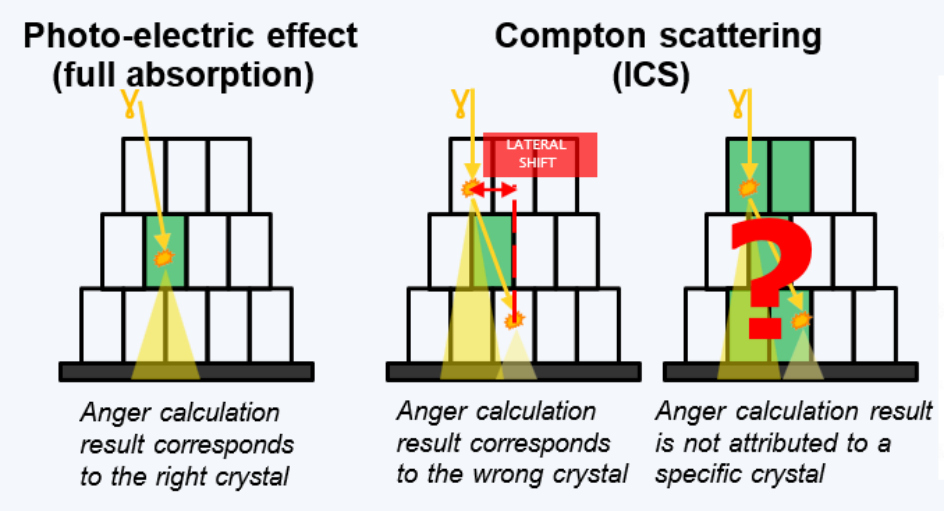

Figure 3.4: Illustration of interaction mechanisms affecting event localization in PET detectors. (Left) In the photoelectric effect, full energy absorption leads to correct crystal assignment. (Center) In Compton scattering (inter-crystal scatter, ICS), lateral shifts cause the Anger calculation to misattribute the event to the wrong crystal. (Right) In complex scatter cases, the Anger calculation cannot confidently assign the event to a specific crystal, leading to uncertainty [26].

To mitigate the impact of ICS, PET systems currently employ a combination of hardware and software strategies. Energy discrimination - applying a narrow energy window around the 511 keV photopeak - helps to reject events where the scattered photon escapes detection or deposits insufficient energy. Geometric filtering further limits accepted events to those consistent with physically plausible coincidence geometries. However, both strategies come with a tradeoff: by filtering out ICS events, a signif-

icant portion of total detected events (sometimes over 25%) is discarded [26]. These strategies are indeed used in our PET detector of the SIRMIO project to manage scattered events. While they help improve data quality, they also reduce system sensitivity, increase acquisition times, and limit the statistical power available for reconstruction.

Despite these efforts, it is increasingly recognized that energy and geometric filtering alone are insufficient to fully correct for ICS effects. This leads to the motivation for more sophisticated approaches: by better understanding the underlying physics and the detector response, we can develop methods to compensate for ICS rather than simply reject it. For example, advanced modeling and correction algorithms could recover the true interaction position even for scattered events, improving spatial resolution without sacrificing sensitivity.

3.2 Thesis Scope and Objectives

The aim of this thesis is to perform a detailed characterization of the SIRMIO PET detector response to 511 keV photons, with a specific focus on understanding and mitigating the effects of inter-crystal scattering (ICS). ICS represents a major source of spatial uncertainty and image degradation in PET systems, particularly under the demanding conditions of small-animal study.

This work combines Monte Carlo simulations, experimental measurements, and data-driven analysis to investigate the frequency, spatial signatures, and energy characteristics of 511 keV events. A key objective is to develop methods to distinguish ICS-induced signals from direct interactions, thereby enabling the suppression or correction of their impact on reconstructed images.

By advancing the modeling of the detector response at the pixel level and integrating this knowledge into event filtering strategies, the project aims to improve image quality, enhance spatial accuracy, and support the implementation of reliable PET-based range verification in proton therapy.

Chapter 4

Materials and Methods

This chapter details the experimental setup, instrumentation, and materials utilized for the modeling and characterization of the SIRMIO PET scanner. Building upon the foundational principles and limitations of PET imaging discussed in the previous chapter, the focus here is on the technical implementation of the system. Specifically, we describe the detector geometry, component layout, readout electronics, and radioactive sources employed in experimental measurements. In addition, we present the Monte Carlo simulation framework developed to model photon interactions within the detector system, which serves as a complementary tool to interpret experimental data and evaluate detector performance under controlled conditions.

4.1 SIRMIO PET Scanner

Design Objectives and Constraints

These requirements reflect the core goals of the PET in SIRMIO project: enabling precise treatment verification and biological imaging guidance during preclinical investigations.

Geometrical Configuration of the PET Ring

The SIRMIO PET scanner employs a spherical geometry with an inner radius of 72 mm, selected to maximize solid angle coverage while preserving sufficient clearance for beamline components and the integration of animal positioning systems. This configuration achieves approximately 44% solid angle coverage of the field of view (FOV), thereby ensuring enhanced angular sampling crucial for attaining high spatial resolution and detection sensitivity [27].

The geometry of the PET system is illustrated in Figure 4.1, which highlights the spherical arrangement and the compact integration with the beamline.

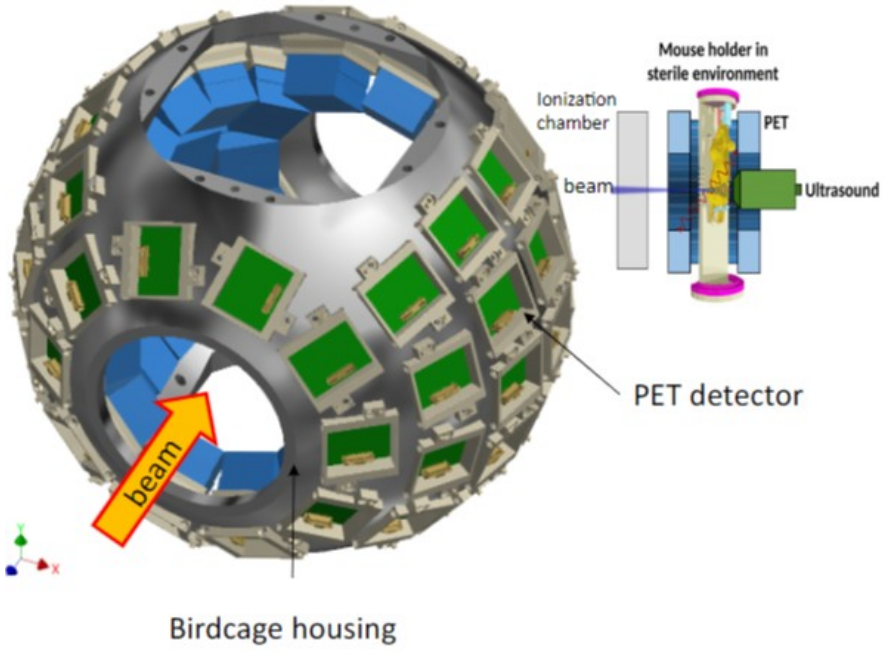

Figure 4.1: Schematic of the SIRMIO PET scanner geometry. [28]

Modular Detector Architecture

The scanner integrates 56 depth-of-interaction (DOI)-capable detector modules arranged in a pyramidal-step configuration. This staggered, multi-layer design minimizes interstitial dead space and facilitates compact, conformal placement of detectors along the spherical surface, improving geometric efficiency. The architectural flexibility of this layout enables not only optimized detection performance but also facilitates integration with auxiliary imaging modalities and a motorized mouse holder, which allows precise positioning of the animal during irradiation. Each detector module is identical and independent, allowing individual replacement or maintenance without compromising overall scanner functionality.

Monte Carlo simulations predict a central sensitivity in the range of 7–12%, with spatial resolution spanning from 0.4 mm to 1 mm full width at half maximum (FWHM), depending on the specific location within the FOV [27].

4.2 Detector Components

A detailed schematic of the detector electronics, from SiPM coupling to the digitizer module, is shown in Figure 4.2.

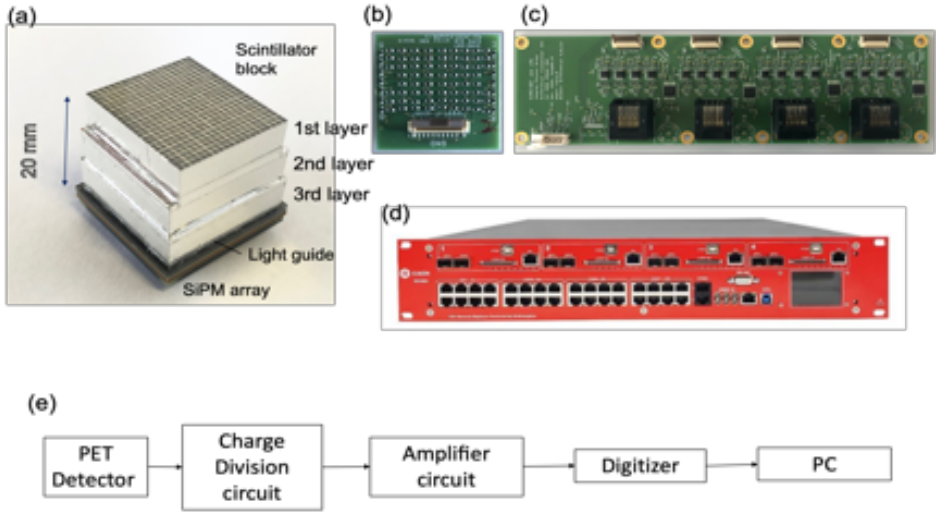

Figure 4.2: Schematic representation of the experimental set-up used: a) Scintillator blocks coupled with SiPMs; b) Charged division circuit for channels number reduction; c) Amplification board circuit; d) Digitizer module; e) Block diagram of the readout system. Image Courtesy of Dr. Munetaka Nitta, LMU. [18]

4.2.1 Scintillator

The scintillator material is a central component in determining the overall performance of a PET system, directly affecting its sensitivity, spatial resolution, and noise characteristics. For the SIRMIO PET scanner, cerium-doped lutetium-yttrium oxyorthosilicate (LYSO:Ce) was selected following a detailed simulation-based optimization study [27]. Alternatives such as GAGG were evaluated and compared across key performance metrics, including detection efficiency and signal-to-noise ratio in low-activity environments, which are typical in preclinical in-beam PET applications. LYSO consistently demonstrated superior sensitivity and lower statistical noise, justifying its selection as the optimal scintillator [27, 18].

Although LYSO contains a small fraction (about 2.6%) of the naturally radioactive isotope ^{176}Lu, simulations showed that the intrinsic background activity introduced by its β-decay and associated γ-ray emissions can be effectively mitigated. Through the application of optimized energy windows and geometrical filtering strategies for lines of response (LORs), these background contributions become negligible in the final image reconstruction. Figure 4.3 illustrates the decay scheme of ^{176}Lu, and Figure 4.4 compares the energy spectra in isolated and embedded detector configurations.

From a physical standpoint, LYSO offers an excellent combination of properties tailored for PET: high density (7.1 g/cm^3), high light yield (32,000 photons/MeV), short decay time (40 ns), and strong resistance to radiation damage [18]. These features enable effective stopping of 511 keV annihilation photons and facilitate high count-rate

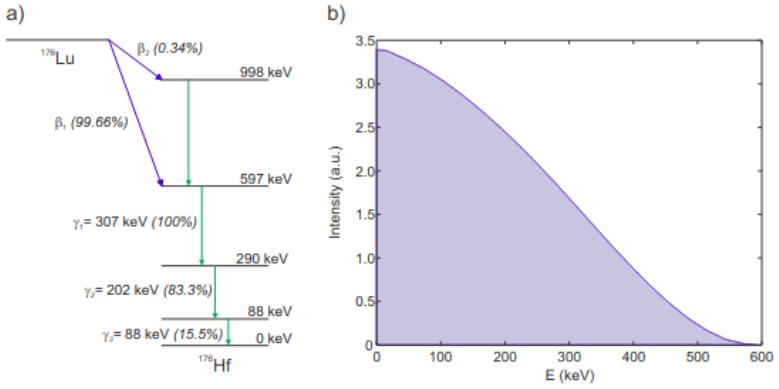

Figure 4.3: (a) Decay scheme of ^{176}Lu and (b) energy spectrum of emitted electrons. Adapted from [18].

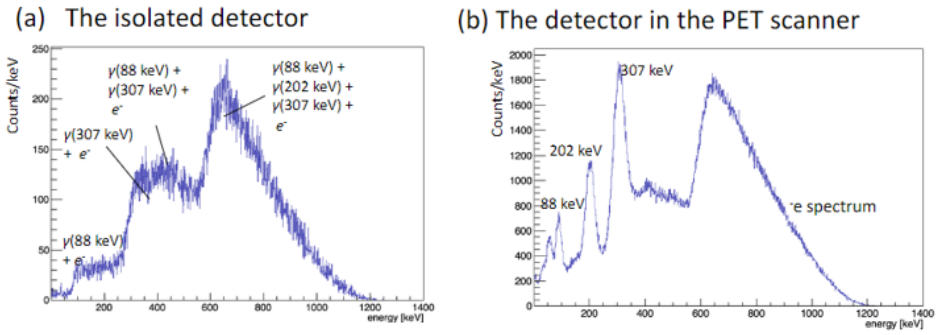

Figure 4.4: Energy spectrum of ^{176}Lu background in (a) an isolated detector and (b) the integrated PET scanner. Adapted from [18].

operation with minimal signal degradation.

Each detector module integrates a pixelated LYSO crystal block arranged in a pyramidal-step configuration composed of three staggered layers. The pixel size is 0.9 mm × 0.9 mm × 6.67 mm, with layer-specific matrices of 20 × 23, 23 × 23, and 24 × 24 pixels. The offset between layers corresponds to half a pixel pitch, enabling depth-of-interaction (DOI) encoding by resolving the axial coordinate of photon interaction. This configuration reduces parallax errors due to the incidence of oblique photons and enhances spatial resolution [18]. The mechanical layout is depicted in Figure 4.5.

To further optimize light confinement and signal clarity, each pixel is optically isolated by $BaSO_4$ reflectors, and the surface of the scintillator block is wrapped with Teflon tape, as shown in Figure 4.6. This shielding minimizes external light interference and enhances signal-to-noise performance.

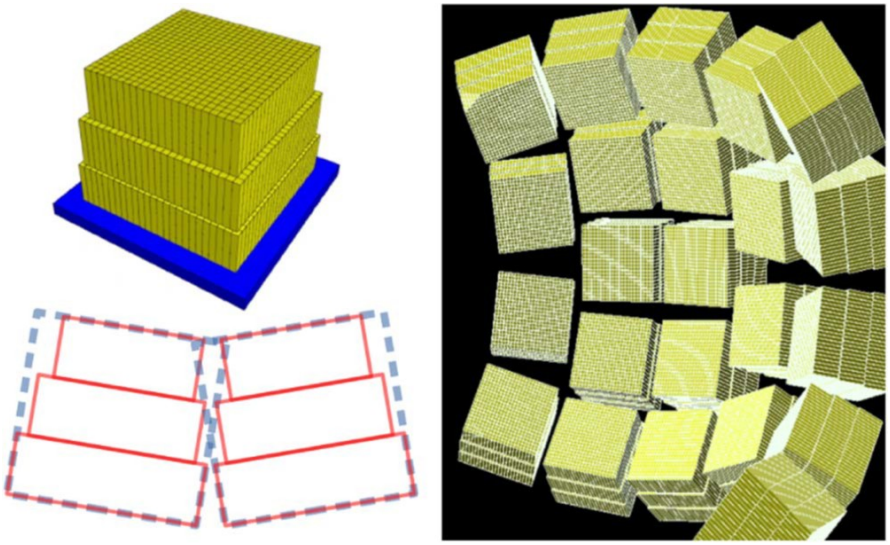

Figure 4.5: Left: Pyramidal-step configuration of a pixelated LYSO detector block. Right: Integration into the spherical PET scanner. Image adapted from [27].

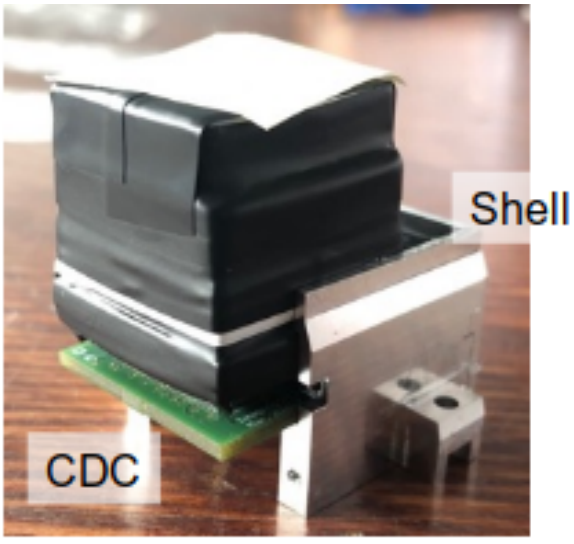

Figure 4.6: Shell used to embed the detector module, including the taped scintillator block, MPPC array, and Charge Division Circuit (CDC), into the PET scanner. Image courtesy of Dr. Munetaka Nitta, LMU [18].

4.2.2 Photodetector: SiPM Array

In the SIRMIO PET system, efficient conversion of scintillation light into electrical signals is realized by coupling each pixelated LYSO:Ce scintillator block to a silicon photomultiplier (SiPM) array via a 1 mm thick optical light guide (dimensions: 25.8 mm × 25.8 mm × 1 mm). The SiPM used is the Hamamatsu S14161-3050HS-08 model, consisting of an 8 × 8 matrix of 64 individual pixels, each measuring 3 mm × 3 mm with 0.2 mm gaps between pixels. The compact structure of the SiPM, coupled with its high fill factor, ensures precise spatial resolution, which is crucial for the small animal in-beam PET application.

This SiPM model comprises 3531 microcells per pixel, providing a typical gain on the order of 10^6 and a photon detection efficiency (PDE) of up to 50% at 450 nm, aligning well with the LYSO emission peak. Its low operational voltage of approximately 41 V enhances stability and minimizes noise, making it particularly suitable for the low-activity environment of in-beam PET scanning[18, 20].

Figure 4.7 illustrates the SiPM array (left) and its integration with the scintillator block and charge division circuit (right), forming a compact and high-performance detector module tailored to the SIRMIO scanner.

4.2.3 Readout Electronics: CDC and Amplifier Board

To reduce the number of readout channels while preserving spatial information, a Charge Division Circuit (CDC) (Figure 4.7) is employed directly behind the MPPC. The CDC aggregates the 64 individual pixel outputs into four analog signals using a resistive network. These four signals retain the positional encoding necessary for subsequent Anger logic-based event reconstruction [18].

The analog signals are routed via flat flexible cables (FFC) to custom-designed amplifier boards. These boards serve a dual function: they convert the single-ended analog signals to differential mode to suppress transmission noise, and they amplify the signals to match the dynamic range required by the digitization stage. The amplifier board used in the SIRMIO system, capable of handling four detector modules simultaneously, is shown in Figure 4.8.

4.2.4 Digitization Module

Signal digitization is carried out using CAEN R5560 modules, which support up to 128 input channels and operate at a sampling rate of 125 MHz. Each module includes field-programmable gate arrays (FPGAs) that implement real-time digital signal processing algorithms. For the SIRMIO PET application, a trapezoidal shaping filter is applied

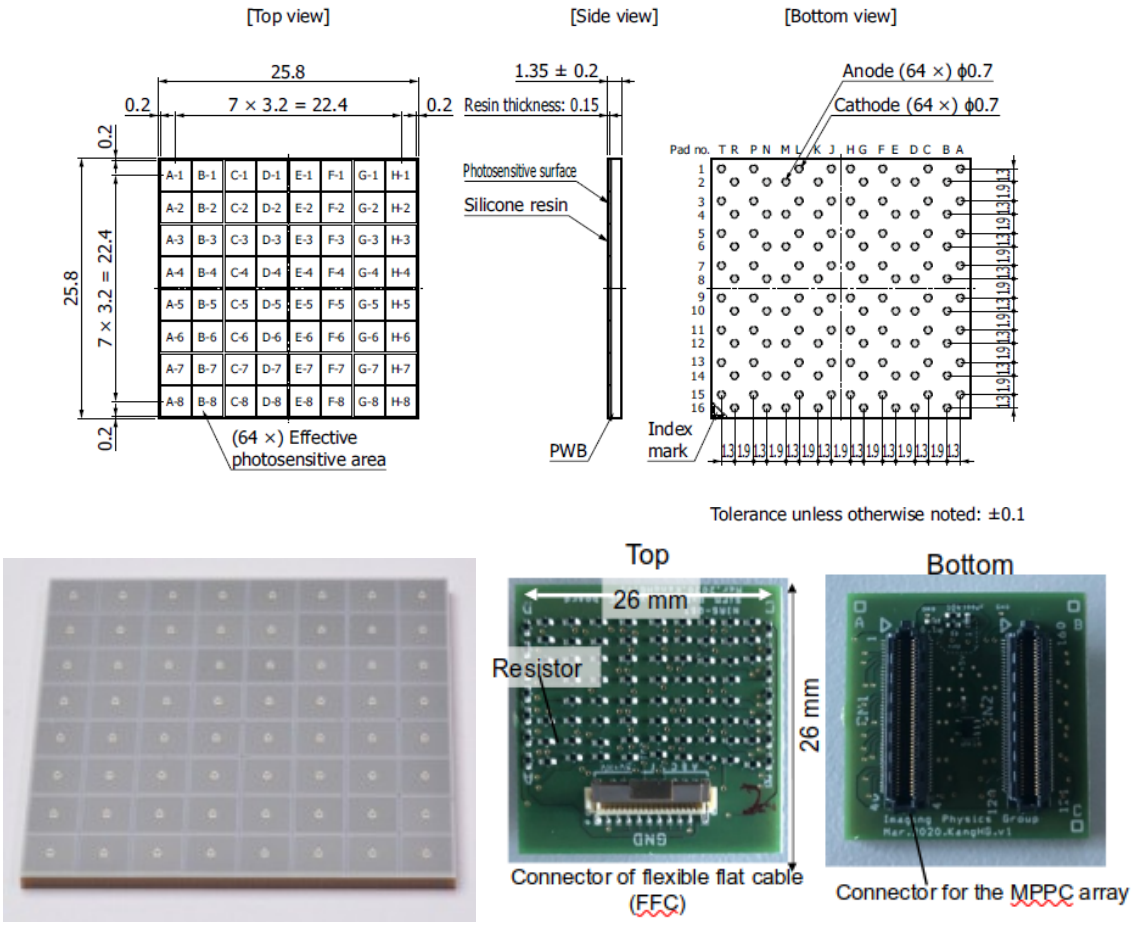

Figure 4.7: Top: Schematic of the Hamamatsu S14161-3050HS-08 SiPM [29]. Bottom left: Photograph of the SiPM array [18]. Bottom right: Integrated detector block including scintillator array, SiPM, and Charge Division Circuit (CDC). Images courtesy of Dr. Munetaka Nitta, LMU [18].

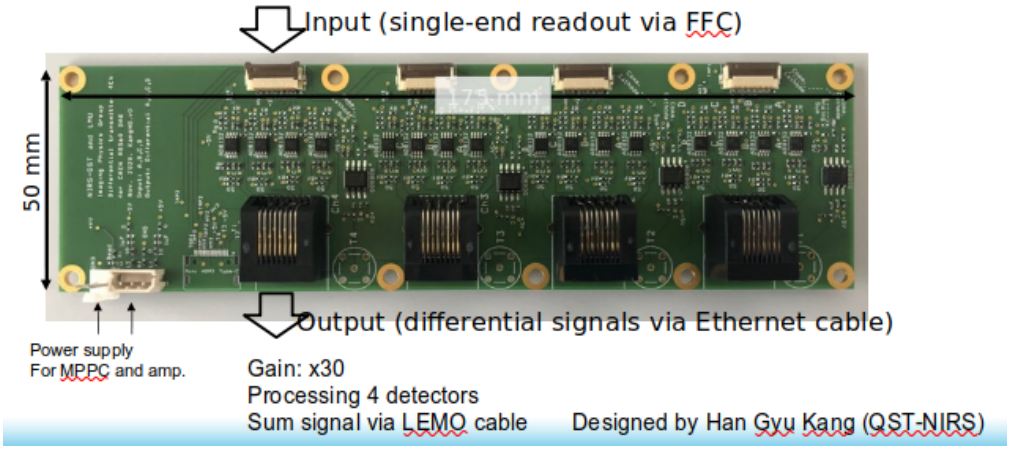

Figure 4.8: Amplifier board used for differential conversion and analog signal amplification. Image courtesy of Dr. Munetaka Nitta, LMU [18].

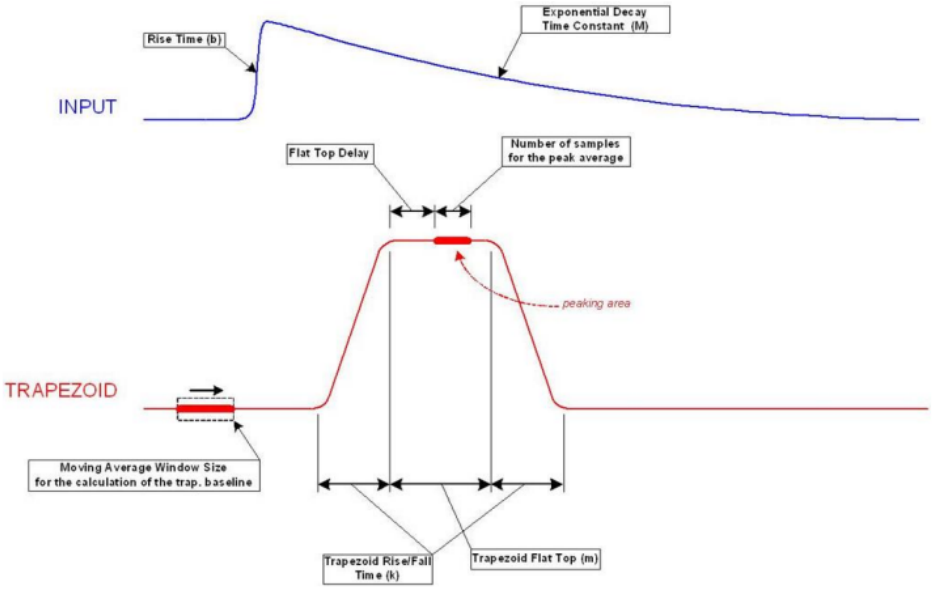

Figure 4.9: Trapezoidal shaping filter implemented in the CAEN R5560 digitizer for real-time energy extraction [18].

to extract the energy, timing, and spatial features of each signal.

This filter converts the exponentially decaying signals into trapezoidal waveforms whose flat-top amplitude correlates with the deposited energy. The filter parameters—including peaking time, flat-top duration, and decay constants—are configurable to optimize performance under different experimental conditions [18].

The digitized signals exhibit a timing resolution of 8 ns, sufficient to support coincidence event reconstruction. Output data are recorded in list-mode, enabling offline analysis and image reconstruction, presented in 5. The filtering principle is illustrated in Figure 4.9.

4.3 Interaction Position Reconstruction

4.3.1 Pixel Encoding via Geometric Offsets

To achieve the sub-millimeter spatial resolution required for in-beam small animal PET imaging, the SIRMIO scanner employs a finely pixelated LYSO:Ce scintillator array arranged in a three-layer pyramidal-step configuration. As presented above, each successive layer is laterally shifted by half a pixel pitch, introducing a geometric asymmetry along the depth (z) axis. This design ensures that interactions occurring at different depths produce unique light distribution patterns.

Consequently, each gamma interaction can theoretically be localized in three dimensions: the transverse (x, y) coordinates and the depth (z), corresponding to the layer

in which the interaction occurred. The lateral offset between layers acts as an intrinsic geometric encoder, enabling the identification of both the scintillation pixel and its depth.

When a 511 keV annihilation photon interacts within the LYSO block, it produces scintillation light that propagates through a 1 mm thick optical light guide to a Multi-Pixel Photon Counter (MPPC) array. This MPPC consists of 64 individual pixels, and the resulting signals are processed by a Charge Division Circuit (CDC), which condenses the 64 channels into four analog outputs (S_1 to S_4). This compression supports a compact and cost-efficient readout architecture while preserving spatial sensitivity.

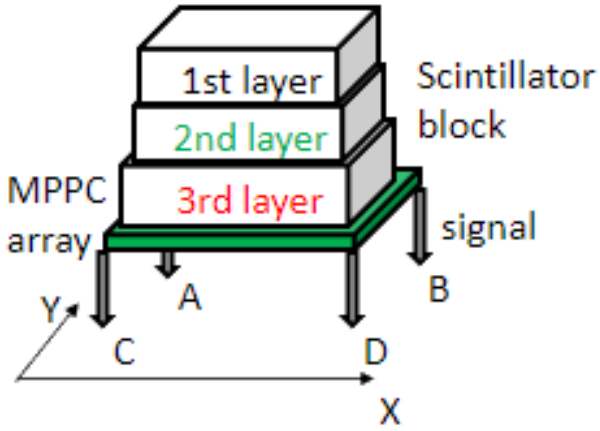

Figure 4.10: Sketch of the four-channel output signal routing from the CDC used for planar interaction position reconstruction. Courtesy of Dr. Munetaka Nitta, LMU.

4.3.2 Planar Localization using Anger Logic

The planar coordinates of the interaction point are reconstructed using the Anger logic method:

$$x = \frac{(S_2 + S_4) - (S_1 + S_3)}{\sum_{i=1}^{4} S_i}, \qquad y = \frac{(S_1 + S_2) - (S_3 + S_4)}{\sum_{i=1}^{4} S_i}. \tag{4.1}$$

These expressions yield a weighted centroid of the light distribution, serving as an estimate of the transverse interaction position. Figure 4.10 illustrates the signal routing implemented in the CDC. This layout supports the Anger logic algorithm for (x,y) position reconstruction, as described by Equation 4.1.

4.3.3 Flood Map Analysis and Layer Separation

The depth of interaction (DOI) is inferred indirectly through the spatial patterns observed in the flood maps. As shown in Figure 4.11, each layer's lateral displacement

results in a characteristic shift in the reconstructed (x, y) distribution. Events originating from different layers cluster into distinguishable patterns in these 2D histograms (see Figure 4.11), allowing identification of the originating scintillator pixel and its corresponding layer.

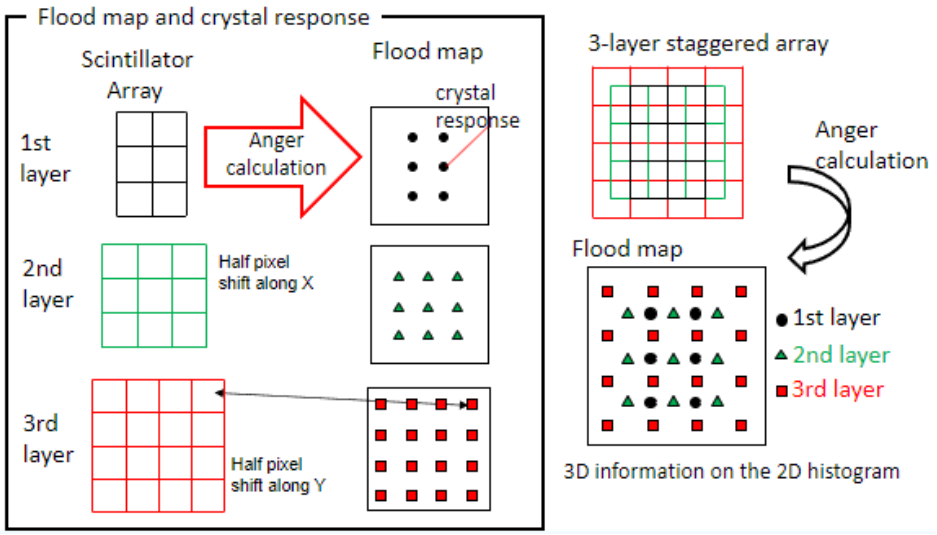

Figure 4.11: Schematic representation of layer shifts in the pyramidal crystal block. The offset between layers enables DOI discrimination. Image courtesy of Dr. Munetaka Nitta, LMU.

It should be noted, however, that this reconstruction method assumes ideal conditions. In practice, effects such as optical crosstalk, variations in crystal response, and inter-crystal scatter introduce deviations from the idealized patterns. Thus, accurate DOI determination ultimately relies on experimental calibration and correction procedures that account for these perturbations. The performance and limitations of this approach under realistic experimental conditions are presented and discussed in detail in Chapter 5.

4.4 Irradiation Sources and Data Acquisition

4.4.1 Micro Derenzo Phantom with FDG

To assess the spatial resolution and imaging capabilities of the SIRMIO PET scanner in a preclinical setting, a micro Derenzo phantom (MediLumine, Canada [30]) was employed. This phantom comprises six clusters of capillary rods with diameters of 1.5, 1.2, 1.0, 0.9, 0.8, and 0.7 mm, each arranged with inter-rod spacing equal to its respective diameter and a height of 10 mm. With an overall external diameter of 27 mm, the phantom is widely used for benchmarking high-resolution performance in

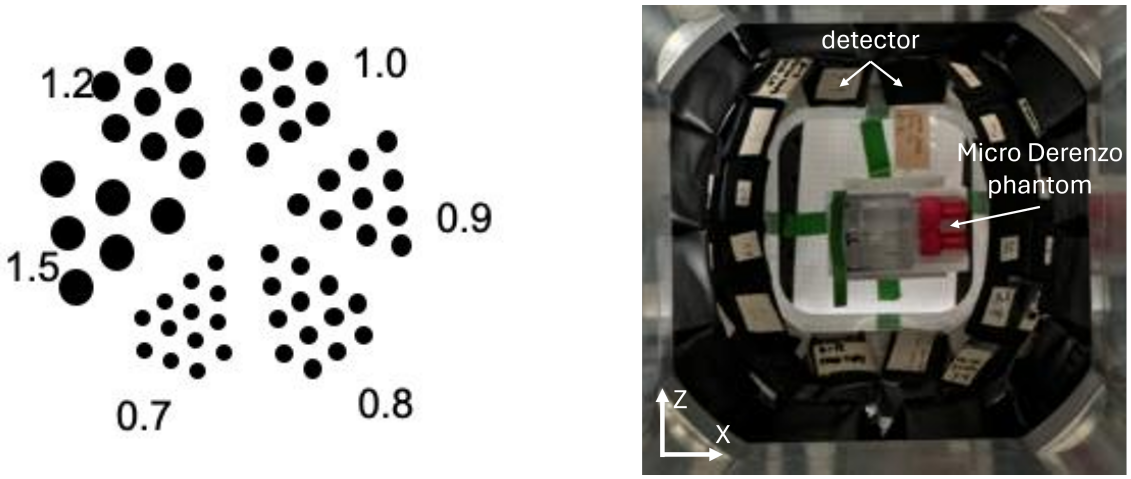

Figure 4.12: Left: Schematic of the micro Derenzo phantom (Courtesy of Dr. Munetaka Nitta). Right: Phantom positioned at the center of the PET scanner [31].

small animal PET systems.

Figure 4.12 shows the phantom features capillary rods of varying diameters, enabling resolution testing across multiple scales.

The phantom was filled with approximately 1.65 MBq of fluorodeoxyglucose (FDG) and transported from the clinical production site to the Danish Centre for Particle Therapy at Aarhus University Hospital. During acquisition, it was centrally placed within the scanner field of view, with the rod axis aligned along the horizontal (X) direction of the PET geometry.

Data were acquired in list-mode format during November 2023. Continuous acquisition over several hours enabled the collection of high-statistics datasets suitable for quantitative image quality evaluation.

Fluorodeoxyglucose (^{18}F)

FDG is a radiolabeled glucose analog in which the hydroxyl group is replaced by the positron-emitting isotope ^{18}F. This radionuclide decays via β^+ emission with a half-life of approximately 109.8 minutes:

$$^{18}\mathrm{F} \rightarrow {}^{18}\mathrm{O} + \beta^+ + \nu_e \tag{4.2}$$

Following decay, the emitted positron travels a short distance—typically less than 1 mm in soft tissue—before undergoing annihilation with an electron. This interaction yields two 511 keV photons emitted nearly back-to-back, which constitute the fundamental signal detected in PET imaging.

The corresponding energy spectrum features a continuous positron emission profile (up to 633 keV endpoint energy), overlaid with a distinct 511 keV peak originating

from the annihilation photons. This peak is critical for spatial resolution and image reconstruction studies.

4.4.2 ^{22}Na Point Sources

Two sealed ^{22}Na point sources with different activity levels were used for calibration, performance validation, and depth-of-interaction (DOI) characterization.

The high-activity source (1.25 MBq) features a 1 mm active radius encapsulated in a 25 mm diameter, 3 mm thick epoxy disk. Its high emission rate made it ideal for image reconstruction tests and DOI evaluation via back-irradiation. This source facilitated rapid acquisitions with sufficient statistics, particularly in the central field of view, and enabled accurate characterization of spatial resolution, energy response, and system sensitivity under representative and stress-test conditions.

In contrast, the low-activity source (49.9 kBq) served as a stable reference for gain and energy calibration. Its low count rate allowed for extended acquisitions without inducing pile-up or dead time effects, making it well-suited for assessing the linearity and baseline performance of individual detector modules. It was routinely employed to monitor system stability and reproducibility across multiple measurement sessions.

^{22}Na Decay Scheme

The decay of ^{22}Na proceeds predominantly via positron emission (β^+, branching ratio: 90.4%) to the first excited state of ^{22}Ne, which subsequently de-excites with the emission of a 1274.5 keV gamma photon:

$$^{22}\mathrm{Na} \rightarrow ^{22}\mathrm{Ne}^* + \beta^+ + \nu_e \qquad ^{22}\mathrm{Ne}^* \rightarrow ^{22}\mathrm{Ne} + \gamma\ (1274.5\ \mathrm{keV}) \tag{4.3}$$

The associated decay scheme is illustrated in Figure 4.13, highlighting both annihilation and de-excitation pathways.

The emitted positron eventually annihilates with an electron, producing two back-to-back 511 keV photons. The resulting energy spectrum therefore (Figure 4.14) includes both the annihilation peak and the 1274.5 keV gamma peak, which are essential for energy calibration and validating detector performance.

Data Acquisition Protocol

Calibration measurements with the ^{22}Na sources were conducted on multiple occasions at the LMU laboratory under controlled environmental conditions. Although the setup remained consistent, these sessions were performed at different times compared to the

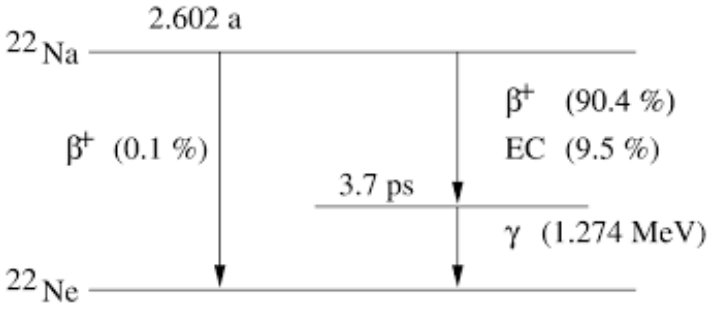

Figure 4.13: Decay scheme of the ^{22}Na isotope [18].

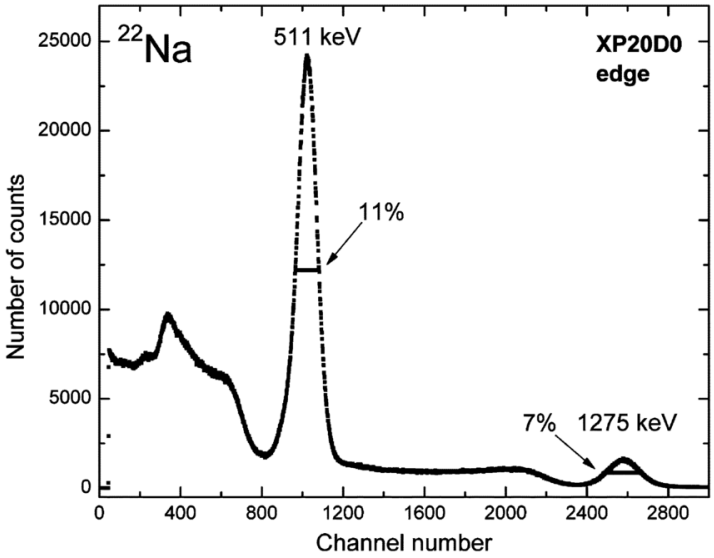

Figure 4.14: Energy spectrum acquired from a ^{22}Na point source, showing the 511 keV annihilation peak and the 1274.5 keV gamma peak [18].

FDG-based measurements, potentially under varying operational conditions (e.g., temperature, voltage, detector aging). As such, direct comparison between the two datasets is not straightforward.

Nevertheless, these calibration datasets were critical for establishing reference performance metrics, verifying energy and gain calibration procedures, and evaluating system stability over time.

4.5 Monte Carlo Simulation Framework

In order to gain a deeper understanding of photon interactions within the detector and to establish a comprehensive baseline for analyzing experimental data, Monte Carlo simulations were carried out using the Geant4 toolkit (version 10.5). These simulations allow for precise modeling of the interaction processes relevant to 511 keV annihilation photons, including photoelectric absorption, Compton scattering, and Rayleigh

scattering, all of which are essential for characterizing the performance of the detector.

The simulation geometry replicates the pixelated LYSO detector modules of the SIRMIO PET scanner, with a focus on detailed modeling of the 3-layer DOI detector blocks. The source of 511 keV photons was implemented as a uniform planar irradiation field, ensuring uniform exposure across the entire detector surface to capture a statistically relevant sample of interaction events.

A total of 10^6 photons were simulated to ensure high statistical significance. The physics processes considered were those included in the Geant4 physics list `G4EmStandardPhysics option4`, which comprehensively accounts for Compton scattering, photoelectric effect, and Rayleigh scattering. The simulation tracked all secondary processes resulting from the primary photon interactions, providing a detailed record of energy deposition events and interaction types.

The simulated data structure generated through Monte Carlo simulations provides a comprehensive dataset for each photon interaction event within the PET detector system. This dataset encompasses the following attributes:

`EventID, pixelL, pixelX, pixelY, energyDep, gammaProcessInfo`

The fields are defined as follows:

- **EventID**: A unique identifier for each simulated event, enabling precise tracking within the dataset.
- **pixelL**: The detector layer in which the interaction occurs.
- **pixelX, pixelY**: The pixel coordinates (X, Y) of the interaction within the layer.
- **energyDep**: The energy (in MeV) deposited within the pixel.
- **gammaProcessInfo**: Encodes the photon interaction process, formatted as `[interaction_type]_[parentID]`. Here, `interaction_type` denotes the specific interaction (e.g., `compt` for Compton scattering, `phot` for photoelectric effect), while `parentID` identifies the track of the primary or secondary particle that caused the interaction.

It is important to note that a photon may undergo multiple interactions as it traverses the detector, resulting in several entries with the same `EventID`. Each of these entries provides detailed information on the interaction location (detector layer and pixel), the deposited energy, and the interaction type. This sequential recording of interactions captures the complete history of photon interactions within the detector matrix.

This structured dataset underpins subsequent data processing and analysis workflows. It facilitates event classification, feature extraction, and image reconstruction, contributing to the quantitative characterization of the PET system's spatial resolution and sensitivity, as detailed in Chapter 6.

Chapter 5

Data processing

Data analysis was conducted using a combination of the ROOT framework [32] and custom Python scripts [33], leveraging both previously developed code modules and new implementations to tailor the processing to the specificities of this study. This dual-language approach combines the flexibility and visualization capabilities of Python with the speed and reliability of ROOT for high-volume data handling.

Throughout this chapter, the employed procedures, algorithms, and challenges encountered during data pre-processing and processing are presented in detail. Emphasis is placed on the essential steps of data sorting, calibration, filtering, and event identification—crucial for extracting reliable information about the detector response at pixel level.

5.1 FDG Data Pre-Processing

5.1.1 Sorting

The data acquisition system, based on CAEN digitizers, operates in a trigger mode where the four channels corresponding to a detector pixel are continuously monitored. An acquisition is triggered when at least one of these channels exceeds a predefined amplitude threshold. Upon triggering, all four channels of the corresponding group are simultaneously read out and stored as a single event. Each event includes the amplitude values for the four channels, detector identifier, and a timestamp with a resolution of 8 ns.

This hardware-level coincidence ensures that each recorded event corresponds directly to a physical interaction within a detector pixel, without requiring post-acquisition grouping. The resulting dataset forms the basis for later processing step.

5.2 Energy and Spatial Calibration

5.2.1 Energy Spectra Analysis

The analysis of the energy spectra constitutes a critical aspect of characterizing the response and performance of each detector module within the PET scanner. For each detector, a one-dimensional energy histogram is generated by summing the signals from the four readout channels associated with a single detection event. This approach exploits the fact that the energy deposited by the incident photon is directly proportional to the combined charge collected across these channels.

Notably, each of the 56 detectors in the system is inherently independent, and although designed to be identical, slight variations in the electronic response, such as differences in gain, noise levels, and optical coupling, can introduce minor discrepancies among them. Consequently, the energy spectra recorded by different detectors exhibit significant differences, as can be observed in Figure 5.1. Such differences underscore the necessity of individual energy calibration for each detector to ensure optimal performance.

The energy spectra reveal not only the photopeak corresponding to the 511 keV annihilation photons, crucial for PET imaging, but also additional peaks associated with the specific radionuclide sources employed during calibration and testing. For instance, measurements involving ^{22}Na sources display both the 511 keV peak and the 1274.5 keV gamma peak, while measurements with FDG-filled phantoms predominantly show the 511 keV peak alongside a continuous background spectrum. Another salient feature is the intrinsic background radiation from ^{176}Lu present in the LYSO crystals, which contributes to a low-energy background in the spectra. The identification and quantification of these features are essential for distinguishing 511 keV events from scattered or spurious background signals, a process that will be further detailed in Section 5.3.

A thorough analysis of the energy spectra also serves as a diagnostic tool for identifying malfunctioning or degraded detectors. For example, a significant shift of the photopeak towards lower energies, indicates potential issues such as reduced light output or electronic gain degradation. Recognizing such deviations allows for timely maintenance and ensures the integrity of the PET data acquisition process [18].

Figure 5.1 illustrates the typical energy spectra of detectors 10 and 30. The 511 keV photopeaks are clearly visible, as is the considerable shift.

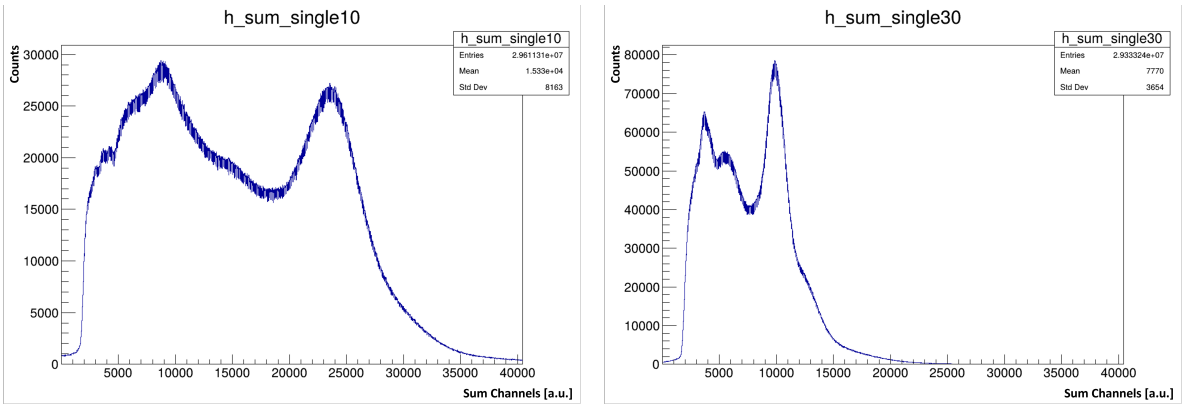

(a) Energy spectrum of detector 10.

(b) Energy spectrum of detector 30.

Figure 5.1: Example energy spectra obtained from two different detectors, illustrating differences in peak positions and background contributions.

5.2.2 Flood maps Generation

Flood maps are essential diagnostic tools in the calibration of PET detector modules. They provide a two-dimensional representation of the spatial distribution of detected events within each detector. These maps are generated by filling two-dimensional histograms with the (x, y) coordinates of each detected event, calculated using the Anger logic method described in Chapter 4. This process is repeated for each of the 56 independent detectors.

Although the overall structure of the flood maps remains consistent across detectors—reflecting the shared crystal geometry—each detector exhibits slight variations in its flood map due to intrinsic differences in construction and relative positioning with respect to the source. As illustrated in Figure 5.2 and Figure 5.3, these discrepancies manifest as subtle differences in pixel definition, shape, and intensity distribution. In general, well-calibrated detectors exhibit clearly defined pixel boundaries, especially in the central region, whereas the edges often appear blurred and less distinct. These edge effects are usually attributed to reduced light collection, poor coupling, or lower event statistics.

Flood maps play a crucial role in both qualitative and quantitative assessments of detector performance, forming the foundation for assigning events to specific pixels. They also provide a valuable diagnostic tool for identifying damaged or malfunctioning detectors, as areas with reduced or absent event counts can be visually discerned [18]. Such maps enable the approximate localization of damaged scintillator crystals or SiPM pixels.

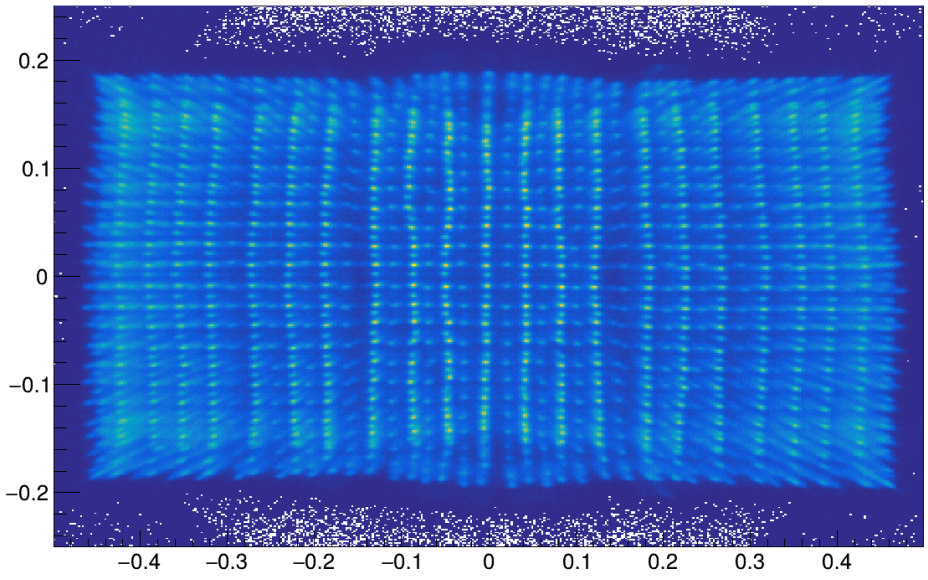

Figure 5.2: Flood map of detector 10.

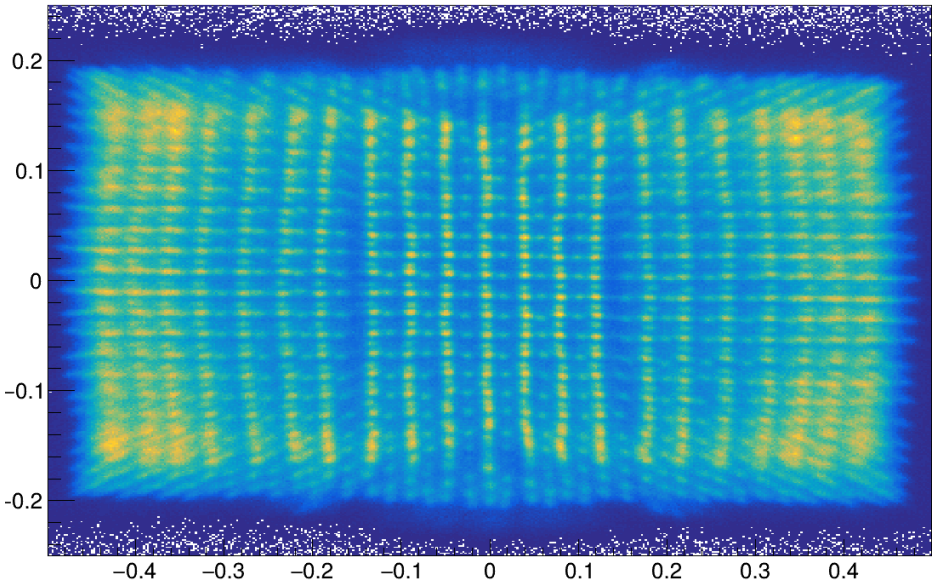

Figure 5.3: Flood map of detector 30.

5.2.3 Look-up table (LUT) Definition

As previously described, achieving optimal spatial resolution in the final PET images relies heavily on accurately assigning each detected event to the correct pixel and scintillator layer. This is accomplished by defining specific regions within the flood maps for each pixel—a process that creates what is known as the Look-up Table (LUT). Each detector's LUT encompasses a substantial number of pixels (e.g., 20×23, 23×23, and 24×24 per layer for 56 detectors), requiring careful calibration.

Initially, pixel boundaries were established manually, which was a labor-intensive

and error-prone process, particularly during later event processing for pixel identification. In this study, LUTs were crafted by manually selecting pixel regions on the flood map for the first scintillator layer using tools like ROOT's `TCutG` function [34]. The manually determined 1st Layer was then employed to algorithmically derive the corresponding regions for the 2nd and 3rd Layers, utilizing the known geometric offsets between the layers. Some complex and ambiguous LUTs were manually revised as well.

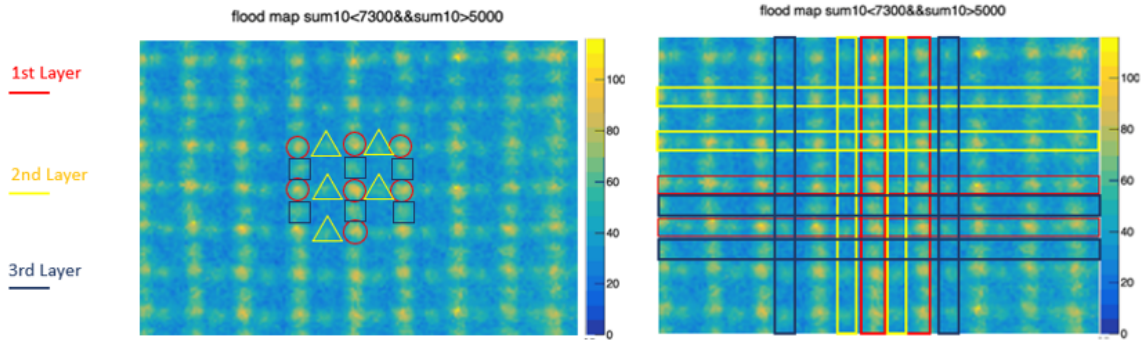

Figure 5.4: On the left, the individual pixel responses for each layer are shown: red circles represent the 1st Layer, yellow triangles the 2nd Layer, and blue squares the 3rd Layer. On the right, the highlighted regions corresponding to the responses of the first (red), second (yellow), and third (blue) layers are displayed. These pixel regions are obtained by summing all the columns and rows intersecting the activated pixels [18].

While this approach ensures good accuracy, especially in the central regions of the detector—where the pixel patterns are clear and well-separated—it is more challenging at the edges. There, pixel boundaries become blurred and overlapping due to optical cross-talk and reduced event statistics, making manual delineation less reliable. Additionally, the automated extension of first-layer boundaries to deeper layers can result in overly broad regions that may encompass events arising from inter-crystal scattering. Consequently, while this method provides the base foundation for pixel identification, it is both time-consuming and subject to uncertainties in boundary accuracy, particularly at the detector periphery. Improvements to this method will be presented in subsequent sections.

5.3 FDG Data Processing

This section describes the detailed processing pipeline using detector 10 as a primary reference, chosen for its good spectral properties and well-defined flood map. Nevertheless, the methodologies outlined here are applicable and adaptable to all detectors within the system. The processing pipeline leverages customized code specifically designed and optimized to account for detector 10's characteristics.

The primary objective is to accurately characterize the detector's response to genuine 511 keV annihilation photons, effectively separating these from scattered and background events. The analysis presented encompasses a detailed evaluation at individual pixel levels to achieve a thorough understanding of detector performance.

The comprehensive processing pipeline includes the following key steps:

- **Coincidence grouping:** Identifying temporally correlated photon pairs within a coincidence window of 40 ns, improving true event selection and reducing random coincidences.
- **Energy window filtering:** Applying a detector-specific energy window centered around the 511 keV photopeak, typically using a range of $\pm 3\sigma$, to reject scattered and background events.
- **Spatial filtering and pixel assignment:** Utilizing Look-up Tables (LUTs) to assign events to specific detector pixels.
- **Pixel position characterization:** Computing the centroid (μ_x, μ_y) and associated uncertainties (σ_x, σ_y) of each pixel to improve spatial resolution.
- **Pixel Spectra characterization:** Analyzing the energy spectra for each pixel and applying Gaussian fits to identify the main peaks associated with the true 511 keV events.
- **Final event selection and validation:** Using the refined pixel and spectral information to select valid events and reject those due to noise, background, or scattering, resulting in a high-quality dataset for image reconstruction.

5.3.1 Coincidence Grouping and Geometric Constraint

To identify true 511 keV annihilation photon pairs resulting from positron-electron interactions, a coincidence grouping procedure is applied based on temporal correlation. Events detected in separate detectors within a coincidence time window of 40 ns are considered to originate from the same annihilation event [18]. This time window is carefully selected to optimize the balance between sensitivity and specificity, minimizing the inclusion of accidental coincidences while preserving genuine pairs.

In addition to the temporal criterion, a geometric constraint is imposed based on the known, fixed configuration of the detector modules. Only coincident events detected by geometrically symmetric detector pairs—i.e., those lying on opposite sides of the scanner axis—are retained. To enforce this condition, a list of non-permissible detector pairs (i.e., those that do not define a valid line of response, or LOR) is compiled and encoded

in a configuration file. Any coincidence involving one of these disallowed detector combinations is excluded from further analysis.

The combined application of temporal and geometric filtering significantly enhances the quality of the dataset. As shown in Figure 5.5, the resulting energy spectra exhibit a notable reduction in background noise and a more pronounced 511 keV photopeak. This improvement is critical for reliable event identification and subsequent image reconstruction.

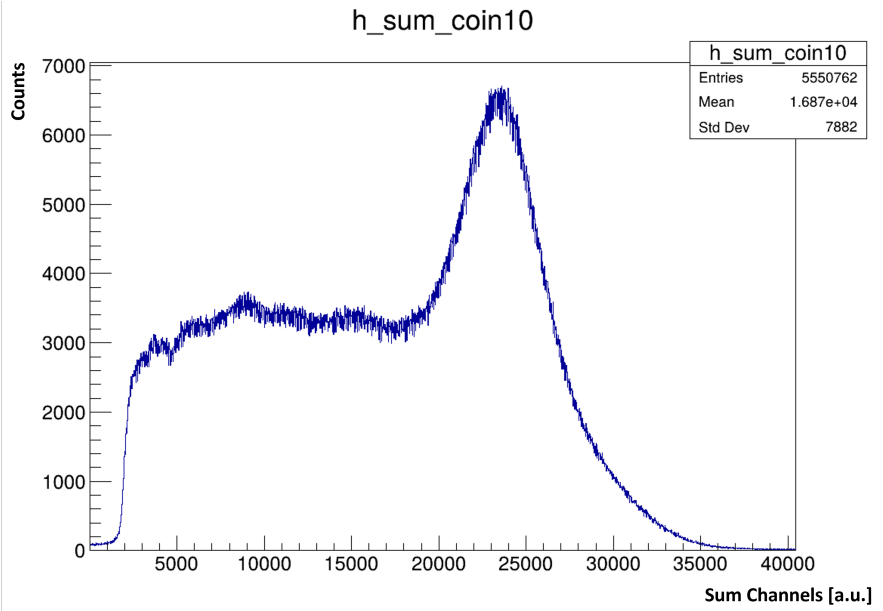

Figure 5.5: spectra of detector 10 after coincidence filtering.

Similarly, the application of coincidence grouping leads to clearer and more defined flood maps, as shown in Figure 5.6.

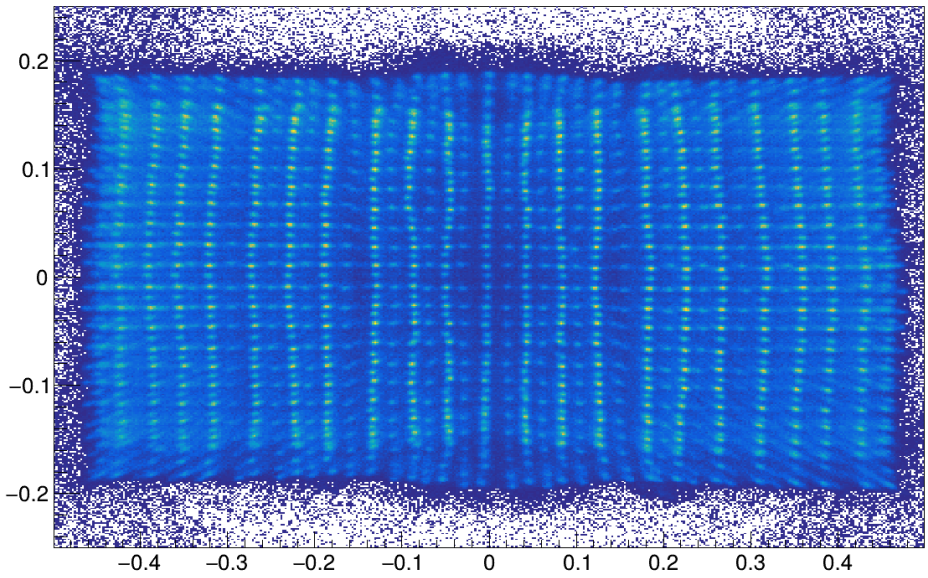

Figure 5.6: Flood map of detector 10 after applying coincidence filtering, illustrating improved spatial delineation.

5.3.2 Energy Filter

An essential step in the event selection process is the application of a detector-specific energy window designed to suppress scattered photons and background radiation while preserving true 511 keV annihilation events. This is accomplished by analyzing the energy spectrum of each detector, identifying the 511 keV photopeak, and fitting it with a Gaussian function to extract the centroid (μ_E) and standard deviation (σ_E). A detector-specific asymmetric window of $[-3\sigma, +5\sigma]$ is then applied around the peak, optimizing the trade-off between sensitivity and specificity.

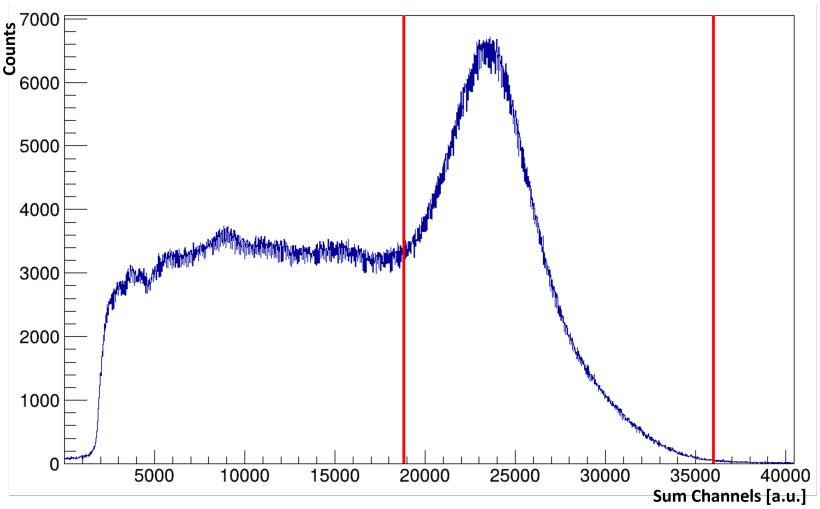

Figure 5.7: Energy spectrum of detector 10 with the applied energy window centered around the 511 keV photopeak.

A relatively broad window is required due to spatial non-uniformities in the energy response across the detector volume. In particular, systematic variations in peak position and shape are observed among the three scintillation layers, as shown in Figure 5.8, which presents energy spectra from the central region of each layer. The first layer exhibits a lower reconstructed energy peak, which is attributed to its greater distance from the SiPM array and thus higher optical attenuation. Additionally, the presence of a $BaSO_4$ reflector introduces further light loss, reducing the collected signal. In contrast, the second and third layers, being closer to the SiPMs, show higher peak positions and broader spectral shapes, likely due to more frequent photon scattering and deeper penetration that lead to increased variance in light collection.

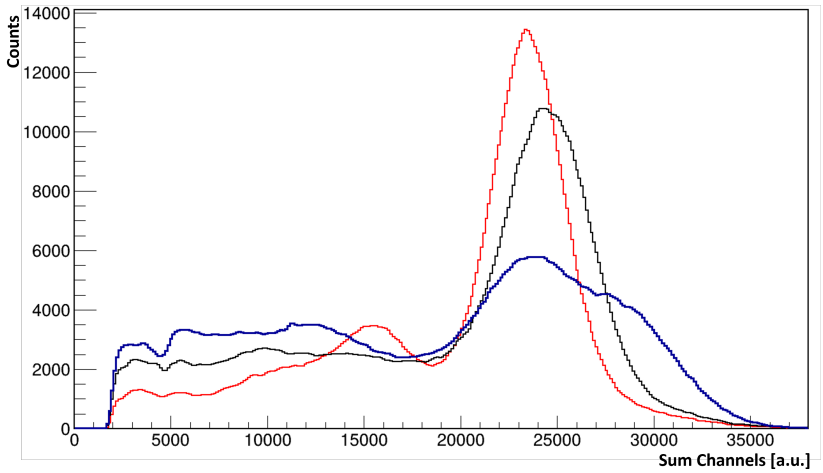

Figure 5.8: Comparison of energy spectra from the central regions of the three scintillator layers in detector 10. Red: 1st Layer, black: 2nd Layer, blue: 3rd Layer.

Further spatial dependence of the energy response emerges when comparing the central region to the edges of the detector. Figure 5.9 presents energy spectra extracted from edge pixels across the three scintillation layers. In contrast to the central region (Figure 5.8), these spectra appear significantly broader and more dispersed, with a noticeable degradation in peak definition. The 511 keV photopeak becomes increasingly difficult to identify, especially in the second and third layers, where the distributions exhibit both lower peak positions and greater spectral confusion. This deterioration in energy resolution is likely due to partial light loss at the periphery of the scintillator, where scintillation photons can escape the crystal volume or undergo multiple reflections before detection, leading to a reduced and more variable signal amplitude.

These findings underline the importance of accounting for intra-detector variations in energy response and motivate the development of pixel-specific or even channel-specific calibration strategies.

The effect of the energy filter is further demonstrated by its impact on the recon-

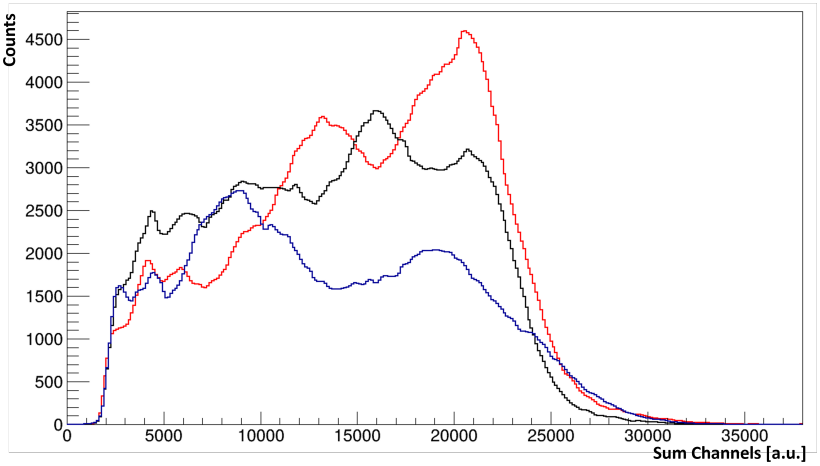

Figure 5.9: Energy spectra from edge regions of the three scintillator layers in detector 10. Red: 1st Layer, black: 2nd Layer, blue: 3rd Layer. Compared to Figure 5.8, all distributions are broader and peaks are shifted to lower energies.

structed flood map. As shown in Figure 5.10, the application of the energy window results in improved pixel separation and sharper structural delineation, owing to the suppression of misidentified or spurious events.

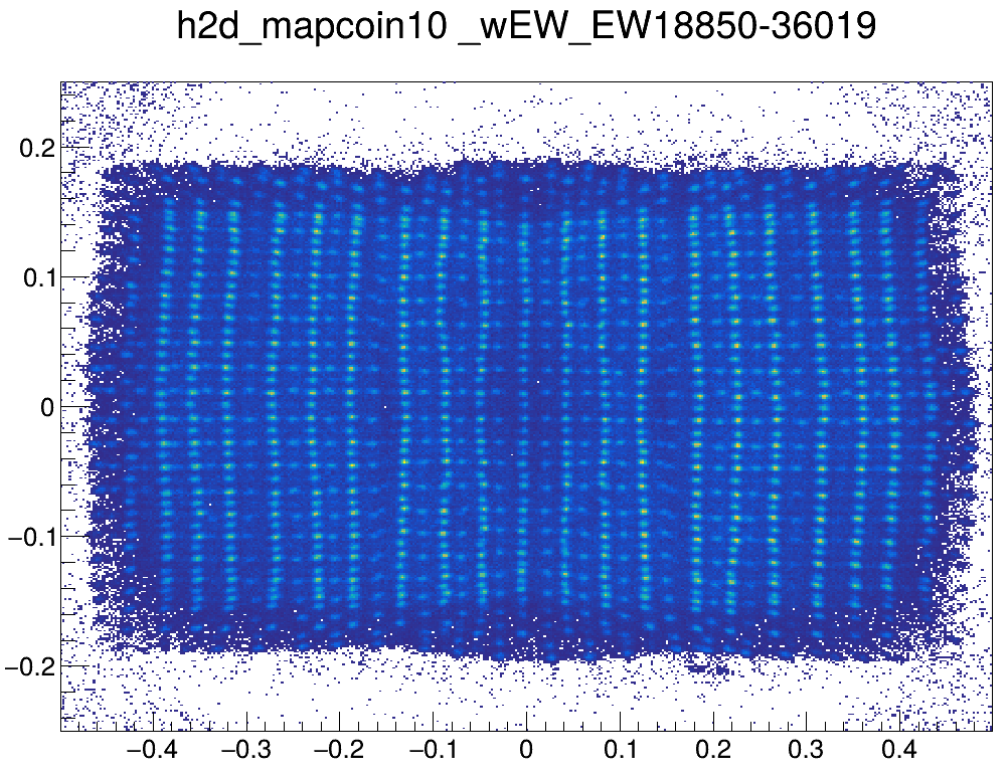

Figure 5.10: Flood map of detector 10 after applying the energy filter. Enhanced pixel delineation and reduced background highlight the effectiveness of energy-based event selection.

5.3.3 Pixel Assignation Filter

The subsequent step in the data processing workflow involves assigning each detected event to a specific pixel within the detector matrix. As previously described, this is accomplished using Look-Up Tables (LUTs), which define the boundaries of valid pixel regions within the flood map. Beyond enabling spatial localization, this procedure also serves as an effective filtering step: events that fall outside the defined LUT boundaries are excluded from further analysis, as they are presumed to originate from scattered photons or other background sources.

This filter is particularly relevant given that the LUT typically encompasses about 75% of the total area of the flood map [26]. As a result, a substantial fraction of events, estimated between 20% and 30%, depending on the data set and detector conditions, are rejected during this stage. These discarded events, as illustrated in Figure 5.11, are in regions of the flood map between pixel patter, and are therefore likely to represent non-primary or misassigned interactions.

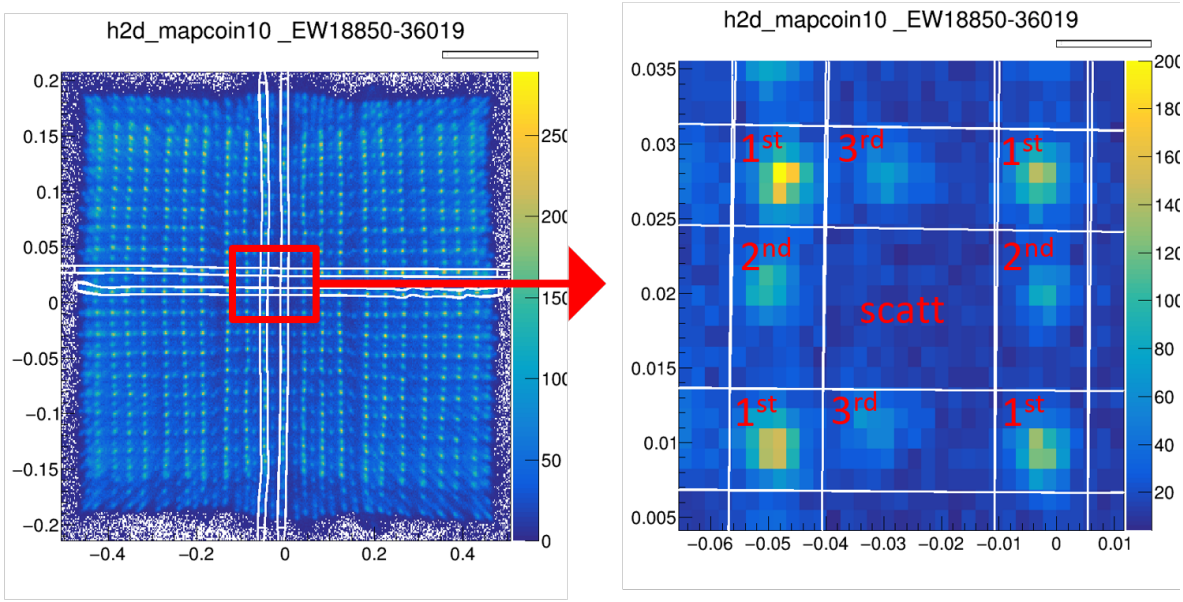

Figure 5.11: Flood map of detector 10 showing the regions excluded by the LUT-based filter. Events falling outside the pixel-defined areas are typically considered scattered or background interactions.

Although these events are excluded from the main reconstruction pipeline, they have been retained in a separate dataset for exploratory analysis. Preliminary investigations have aimed to characterize the energy spectra of these peripheral regions. Proposed ideas include using the energy profile of these excluded events as an estimate of the background spectrum permeating the entire dataset, or attempting to reassign such events to the nearest pixel based on probabilistic models of inter-crystal scattering, as

discussed in [26]. These strategies, however, remain under consideration and are not implemented in the current analysis pipeline.

5.3.4 Pixel Spatial Characterization

Following the application of energy and coincidence filters, a refined dataset for detector 10 was obtained. Although the LUT-based method effectively discards approximately 30% of events—primarily arising from inter-crystal scattering (ICS) and background noise—it presents limitations in pixel localization accuracy. LUT regions are often overly broad and insufficiently precise to resolve pixel boundaries, particularly when distortions or asymmetries in the flood map are present.

To overcome these limitations, a statistical method was developed to refine the pixel identification process. For each LUT-defined pixel region, a two-dimensional histogram of event positions was constructed. Instead of relying on a 2D Gaussian fit—which proves inadequate due to the frequently non-Gaussian and asymmetric event distributions—we computed the mean coordinates ($\bar{x}$, $\bar{y}$) and the corresponding standard deviations (σ_x, σ_y) of each pixel distribution. This statistical characterization provides a more robust, adaptable, and scalable framework suitable for the analysis of all 1565 pixels in a detector module.

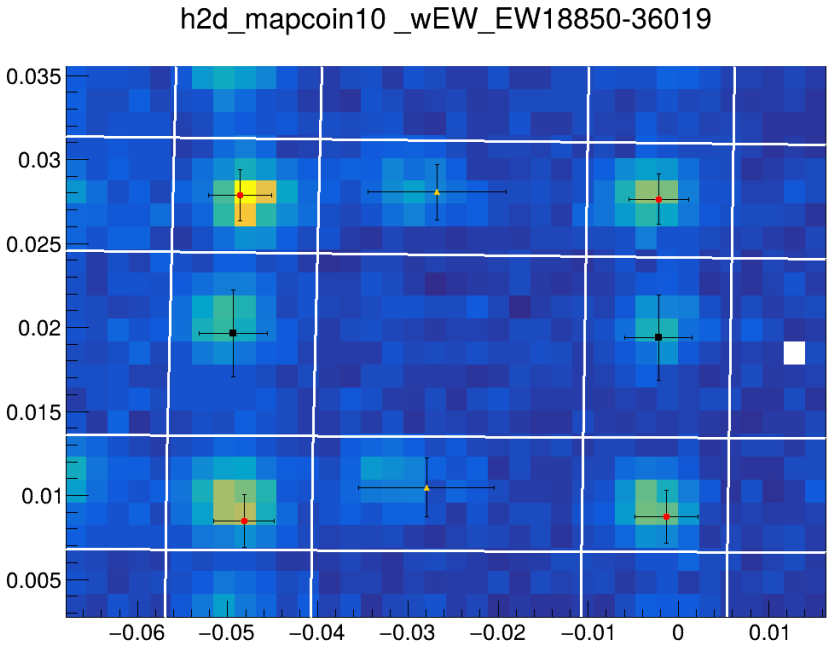

Figure 5.12: Pixel identification in the flood map: 1st layer – red dot; 2nd layer – black square; 3rd layer – yellow triangle. The error bars correspond to the standard deviation of the distribution.

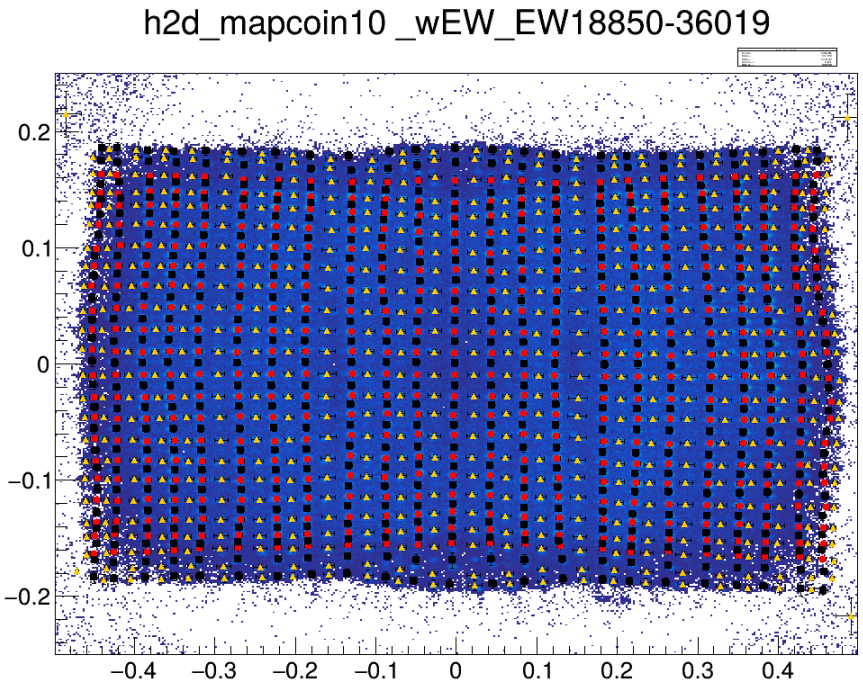

Figure 5.13: Flood map of detector 10 with identified pixel centroids: The 1st layer is marked in red, the 2nd in black, and the 3rd in yellow. Error bars represent the computed σ in x and y directions.

The output of this procedure was used to construct a comprehensive database containing, for each pixel, the centroid coordinates and spatial spread. An excerpt is presented below:

Detector	Layer	Pixel X	Pixel Y	$\bar{x}$	σ_x	$\bar{y}$	σ_y
10	0	11	10	-0.0027	0.0033	0.0096	0.0015
10	1	11	10	-0.0022	0.0038	-0.0187	0.0026
10	2	11	10	-0.0273	0.0076	-0.0271	0.0027

This database facilitates an improved event filtering strategy based on spatial criteria: only events located within a defined window (e.g., 1σ or 2σ) from the centroid are retained. Compared to LUT-defined areas, which often span 3σ to 4σ, this method yields higher spatial precision and better event attribution.

Adjusting the σ threshold allows for control over the trade-off between spatial precision and data retention. A 1σ filter retains approximately 58% of the events, focusing on the most centrally distributed interactions, but excludes a considerable portion of the data. In contrast, a 2σ filter provides a more balanced compromise by including a broader distribution while still excluding outliers and misassigned events; this setting typically results in the exclusion of about 30% of events.

In deeper layers, such as the second and third, broader spatial distributions are typically observed. Although the pixel identification process remains reliable, these layers yield larger sigma values due to increased scattering effects, lower light collection efficiency, and generally reduced event statistics. Nevertheless, the statistical characterization method remains effective and continues to improve upon LUT-only approaches, offering enhanced filtering reliability and better resolution, even in these more challenging regions.

Importantly, this statistical characterization remains dependent on the accuracy of the initial LUT-defined regions. If a LUT region is inaccurately drawn, the resulting centroid and σ values may not fully represent the true pixel structure.

The 2σ spatial filtering criterion was ultimately adopted as the standard for subsequent analyses, providing a well-balanced compromise between event purity and statistical robustness. This threshold effectively retains the core events localized within each pixel's distribution while excluding peripheral events likely to result from inter-crystal scattering or poor localization. Although it leads to the exclusion of approximately 30% of the events, the improvement in spatial resolution and reduction of ambiguous assignments justifies the trade-off, especially for downstream spectral characterization.

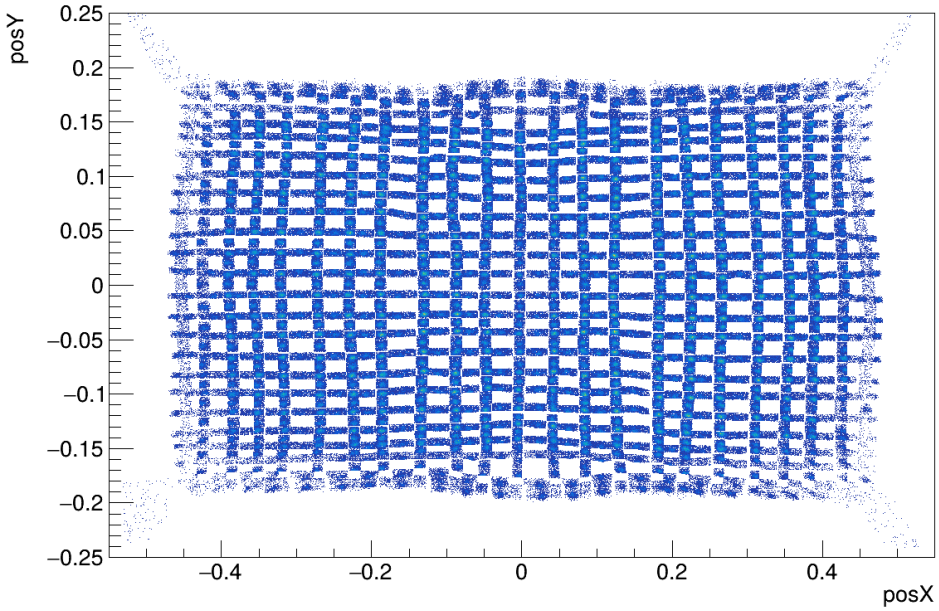

Figure 5.14: flood map of detector 10, filtered using a 2σ pixel spatial filter.

5.3.5 Pixel-Level Spectral Characterization

Following the application of spatial filtering and pixel identification procedures, a detailed pixel-wise spectral analysis was conducted for detector 10. This analysis plays a critical role in understanding the spatial variability in detector response, improving

energy calibration on a per-pixel basis, and refining event-level filtering by accounting for individual pixel behavior.

For each identified pixel, the signal distribution from the four readout channels (ch_0, ch_1, ch_2, ch_3) was extracted and analyzed. The following components were produced:

- Individual energy spectra for each readout channel
- Total energy spectrum $(E = ch_0 + ch_1 + ch_2 + ch_3)$
- Spatial event distributions along the x and y axes within the pixel

This multidimensional approach enables a more granular understanding of detector performance by capturing both spectral and spatial characteristics at the pixel level.

A visual inspection of the spectra highlighted significant variability across the detector. Central pixels in the first layer typically exhibited symmetric, well-localized photopeaks with high signal-to-noise ratio, as shown if Figure 5.15. This indicates the effective rejection of background and inter-crystal scattering (ICS) events through combined energy and spatial filtering, leaving a dominant contribution from primary 511 keV interactions. In contrast, edge pixels frequently suffered from low event statistics, which led to noisier spectra and unreliable peak identification. This lack of statistics, combined with light loss and boundary effects, often resulted in broadened or asymmetric photopeaks.

The situation further deteriorated in the second and third layers, as shown in Figure 5.17, where deeper photon penetration increased the likelihood of Compton scattering and escape events. This leads to broader spectral features, multiple peaks, and lower energy resolution due to the combination of energy loss, increased photon path length, and generally reduced light yield.

To illustrate this behavior, Figures 5.15–5.17 compare the spectral and spatial characteristics of a representative central pixel (11,10) across the three detector layers.

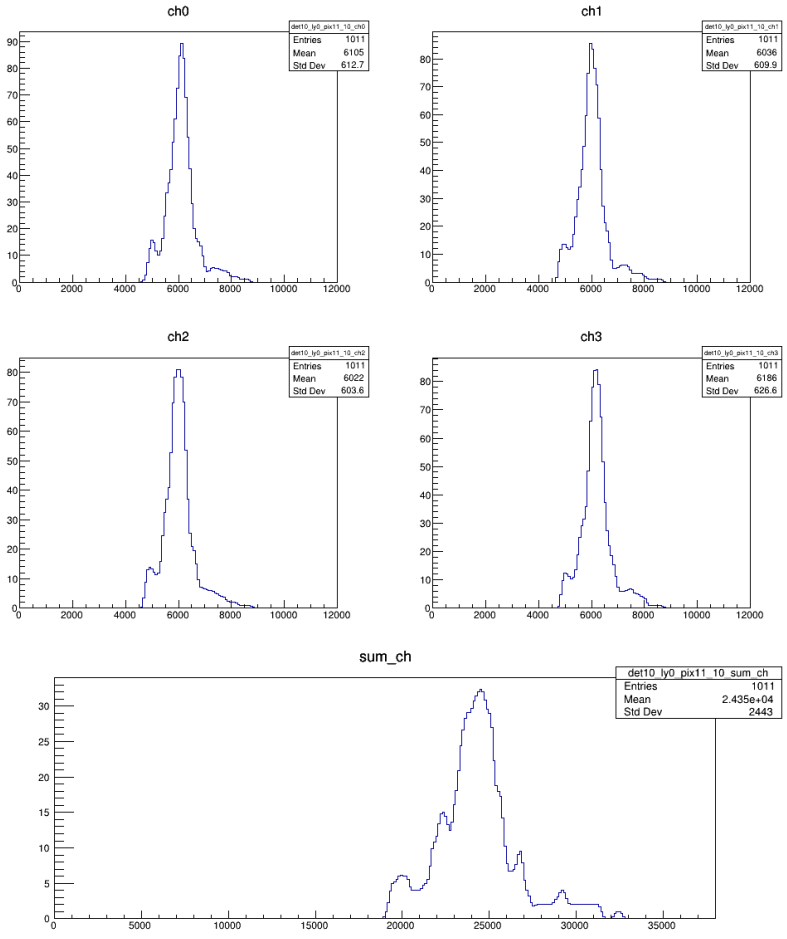

Figure 5.15: Pixel (11,10), 1st Layer: Individual channel spectra and combined energy spectrum showing well-defined photopeaks and successful Gaussian fits. X-axis: channel value [a.u.], Y-axis: event counts.

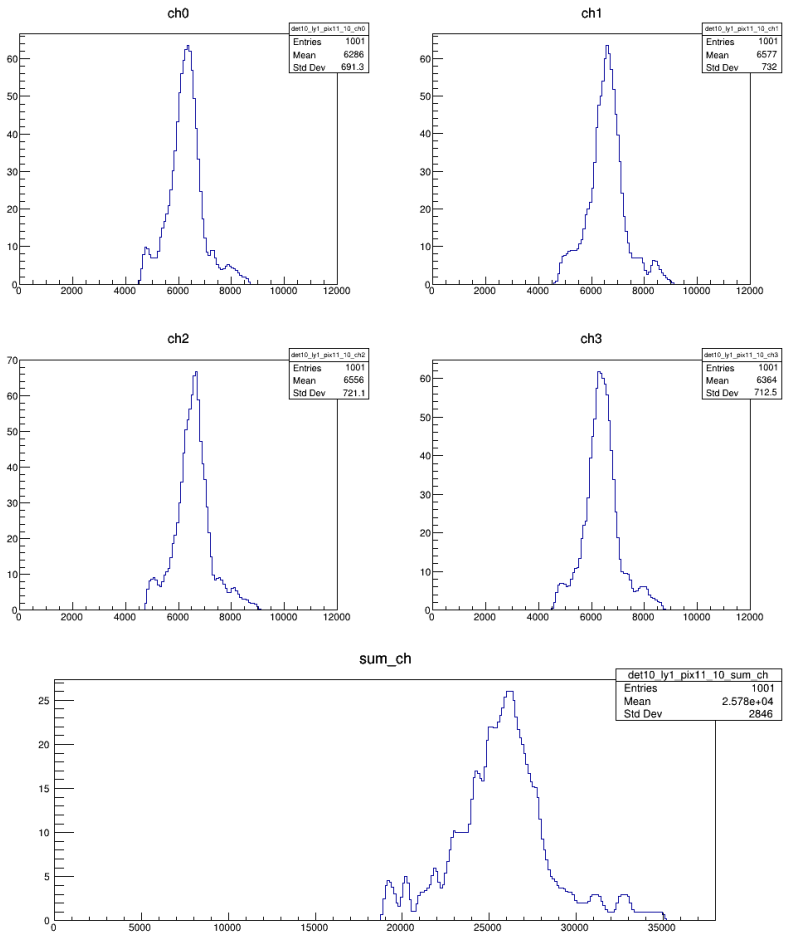

Figure 5.16: Pixel (11,10), 2nd Layer: the photopeaks are still visible, but slightly broader and asymmetric. X-axis: channel value [a.u.], Y-axis: event counts.

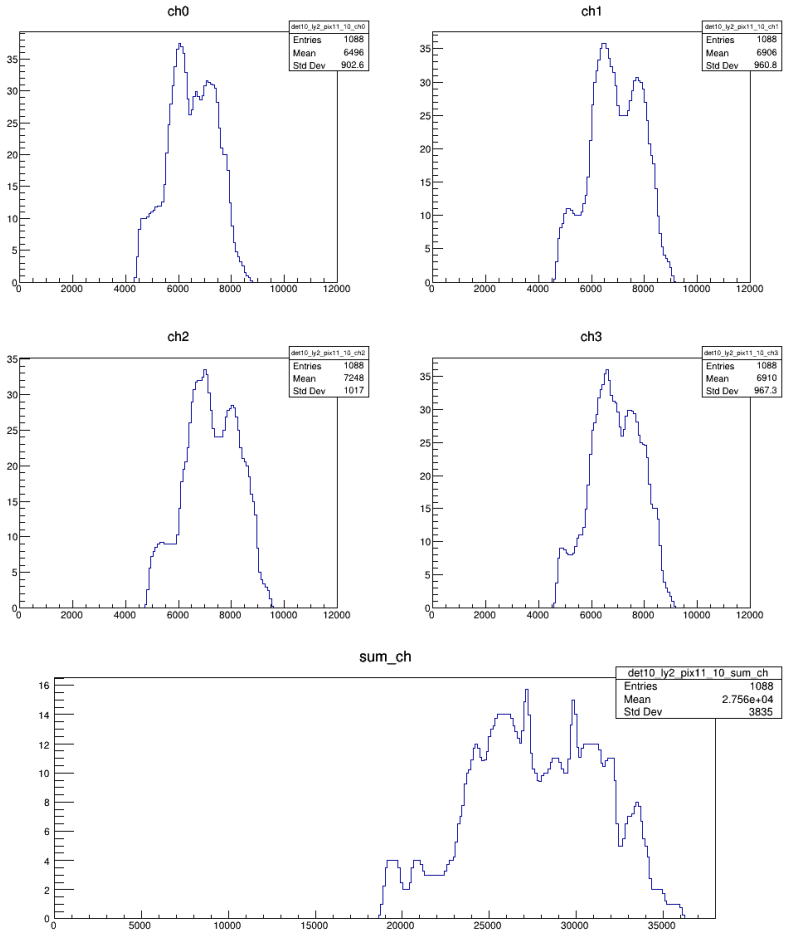

Figure 5.17: Pixel (11,10), 3rd Layer: significant broadening and distortion of the energy spectra are observed, reflecting increased scattering. X-axis: channel value [a.u.], Y-axis: event counts.

Gaussian Peak Fitting and Database Construction

To extract quantitative parameters from each pixel's spectral profile, a semi-automated fitting routine was developed using ROOT. The software was designed with several adjustable constraints and optimization parameters to ensure robust feature extraction under diverse spectral conditions.

The peak fitting and validation workflow involved the following structured steps:

1. **Peak Detection:** Each of the four channel spectra was scanned using `TSpectrum::Search`, targeting peaks within a window centered on the expected 511 keV signal. Constrains for minimum peak height and separation distance reduce the noise.

2. **Gaussian Fitting:** Detected peaks were fitted with Gaussian functions, extracting the centroid (μ), width (σ), and amplitude for each channel.

3. **Combination Matching:** For each pixel, all feasible combinations of one peak per channel were considered. The total energy ($E = \sum \mu_i$) of each combination was computed and compared to the nominal 511 keV peak. Concurrently, the spatial event position was calculated based on the relative peak amplitudes and compared to the pixel's known spatial centroid.

4. **Selection and Storage:** Among the valid combinations, the one with the energy closest to 511 keV and best spatial match was retained. The corresponding Gaussian parameters were then stored in a dedicated structure.

This algorithm was systematically applied across all pixels and layers. Pixels with insufficient statistics, overlapping features, or failed fits were flagged for manual review or excluded from further processing.

Figure 5.18 illustrates the outcome for a well-defined central pixel in the first layer (11,10). Each plot displays the fitted Gaussian peaks (solid red curves), the selected peaks (red vertical lines), and the accepted spatial window (green range) used for event attribution. This approach accounts for minor offsets between fitted centroids and known flood map positions.

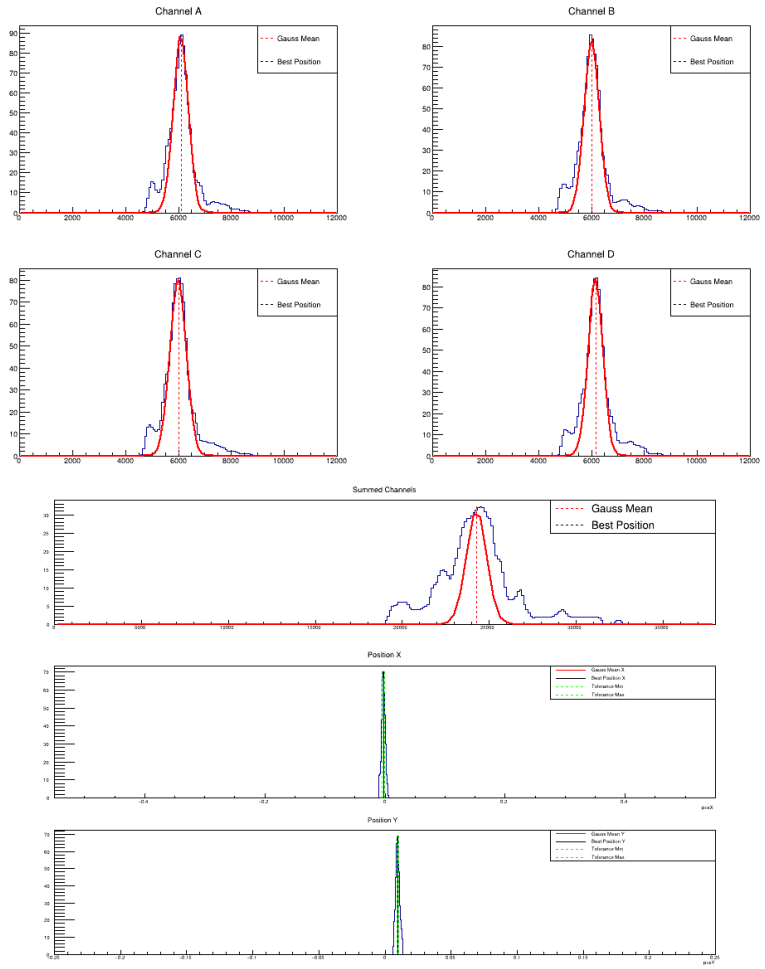

Figure 5.18: Energy spectra and position distributions for pixel (11,10), 1st Layer. Top: individual channel spectra (A–D) with Gaussian fits (red) and best-fit positions (black dashed). Middle: summed spectrum with fit derived from individual channel means. Bottom: reconstructed X and Y positions with fit results and acceptance windows. X-axes: channel value or position [a.u.]; Y-axes: event counts.

Layer	Pixel	μ_{ch_0}	σ_{ch_0}	μ_{ch_1}	σ_{ch_1}	μ_{ch_2}	σ_{ch_2}	μ_{ch_3}	σ_{ch_3}	μ_E
0	11, 10	6101.96	280.65	6022.74	275.71	6111.32	278.24	6056.11	281.89	24292.1
1	11, 10	6321.45	410.50	6605.27	402.19	6634.73	399.64	6328.31	408.12	25889.8
2	7, 19	6126.7	533.3	4976.76	501.39	7071.84	426.02	9625.83	509.81	27801.1
2	11, 10	6068.67	497.04	6506.03	484.22	6663.73	501.33	6859.69	493.10	26098.1
0	1, 11	3439.28	813.30	3342.31	896.23	3368.18	568.10	3406.90	556.27	23735.1
2	1, 6	2692.49	174.12	3043.64	182.47	3183.18	179.20	2755.89	177.99	19306.4

Table 5.1: Extracted Gaussian peak centroids (μ) and standard deviations (σ) for each channel and pixel. $\mu_E = \sum_i \mu_{ch_i}$.

To further assess the variability in spectral quality across the detector, representative fits are shown for both central and peripheral pixels across all layers. Figures 5.18,5.19,

and5.21 illustrate the evolution of the spectra for pixel (11,10), a well-defined central pixel, from the first to the third layer. In the first layer (Fig.5.18), peaks are sharp and well-localized. In the second layer (Fig.5.19), the fits remain accurate but exhibit broader features. By the third layer (Fig. 5.21), the spectral quality deteriorates noticeably, with broader peaks and a mismatch between the selected peak combination and the expected energy, highlighting the challenges posed by increased scattering and reduced light collection.

By contrast, Figure 5.20 presents a positive example from the third layer, where pixel (7, 19) exhibits good spectral resolution and spatial correspondence. This confirms that accurate fitting can be achieved in the third layer in the presence of multiple peaks and distortions.

Edge pixels, also, present difficulties. Figure 5.22 shows pixel (1,11) in the first layer, where large σ values across all channels suggest unresolved overlapping peaks, leading to excessively broad fits. Similarly, pixel (1,6) in the third layer (Fig. 5.23) shows low total energy and indistinct peak structures, likely due to limited event statistics and truncation from energy window cuts.

These examples emphasize the wide variability in spectral fidelity across the detector and underscore the need for layer- and location-specific calibration strategies.

This comprehensive database represents the spectral and spatial fingerprint of the detector at the pixel level. Its analysis and consideration will be presented in detail in Chapter 6.

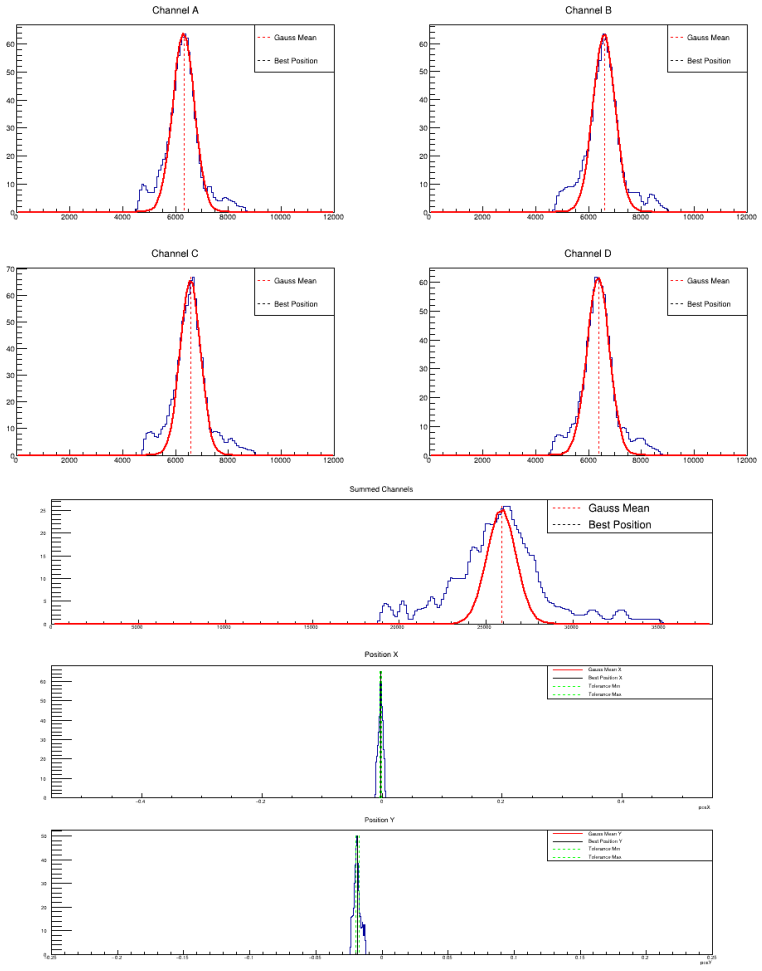

Figure 5.19: Fitted energy spectra and position distributions for pixel (11,10), 2nd Layer. Accurate peak selection and spatial match. X-axes: channel value or position [a.u.]; Y-axes: event counts.

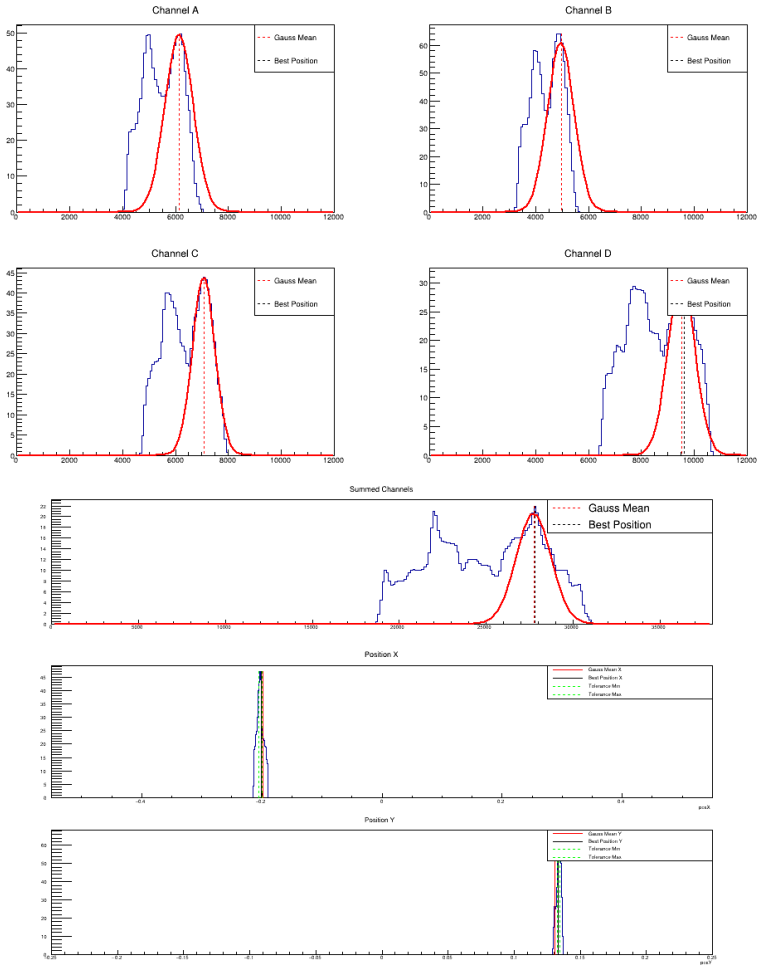

Figure 5.20: Fitted energy spectra and position distributions for pixel (7,19), 3rd Layer. Good spectral resolution and robust fit.X-axes: channel value or position [a.u.]; Y-axes: event counts.

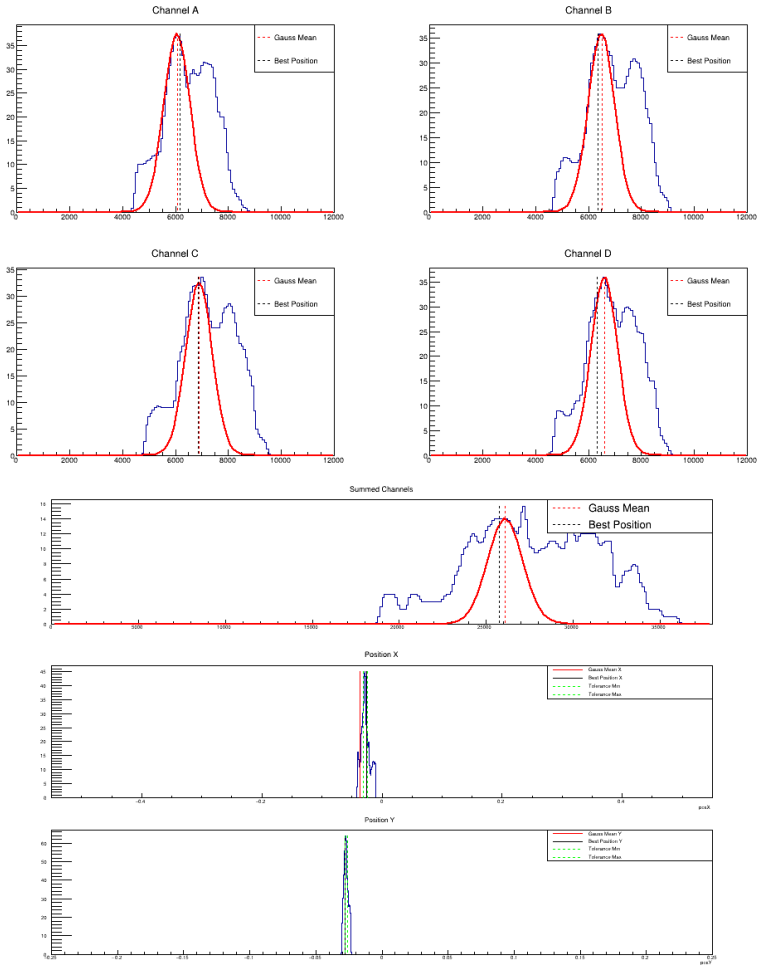

Figure 5.21: Fitted energy spectra and position distributions for pixel (11,10), 3rd Layer. Ambiguous peaks and incorrect selection despite successful fitting. X-axes: channel value or position [a.u.]; Y-axes: event counts.

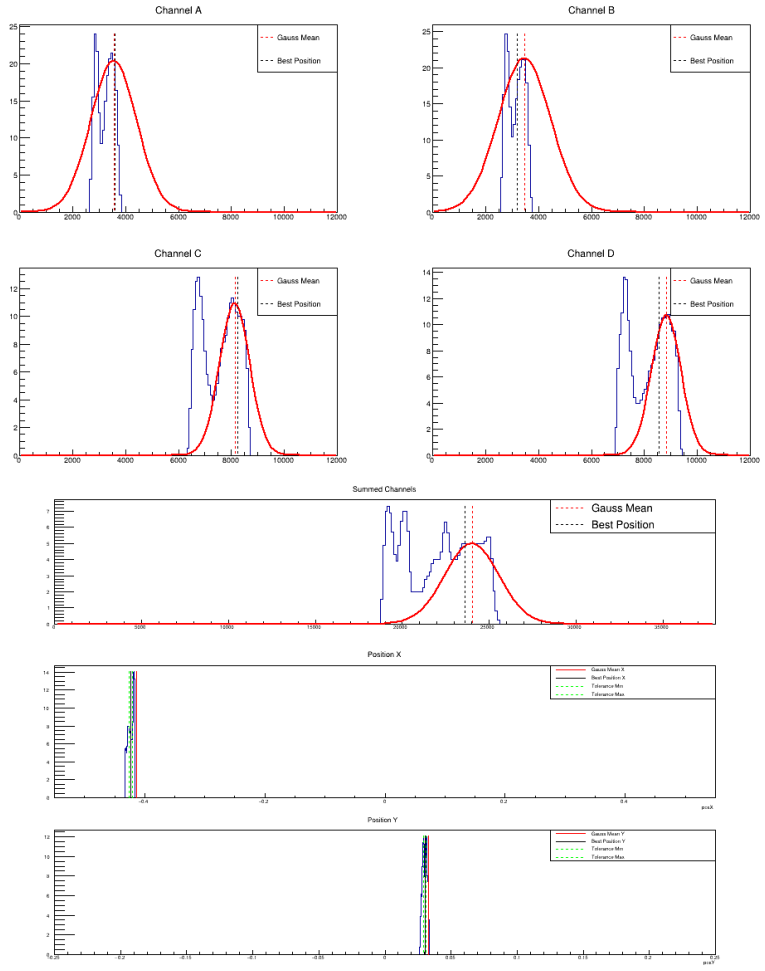

Figure 5.22: Fitted energy spectra and position distributions for pixel (1,11), 1st Layer (edge pixel). Broad fits due to overlapping peaks. X-axes: channel value or position [a.u.]; Y-axes: event counts.

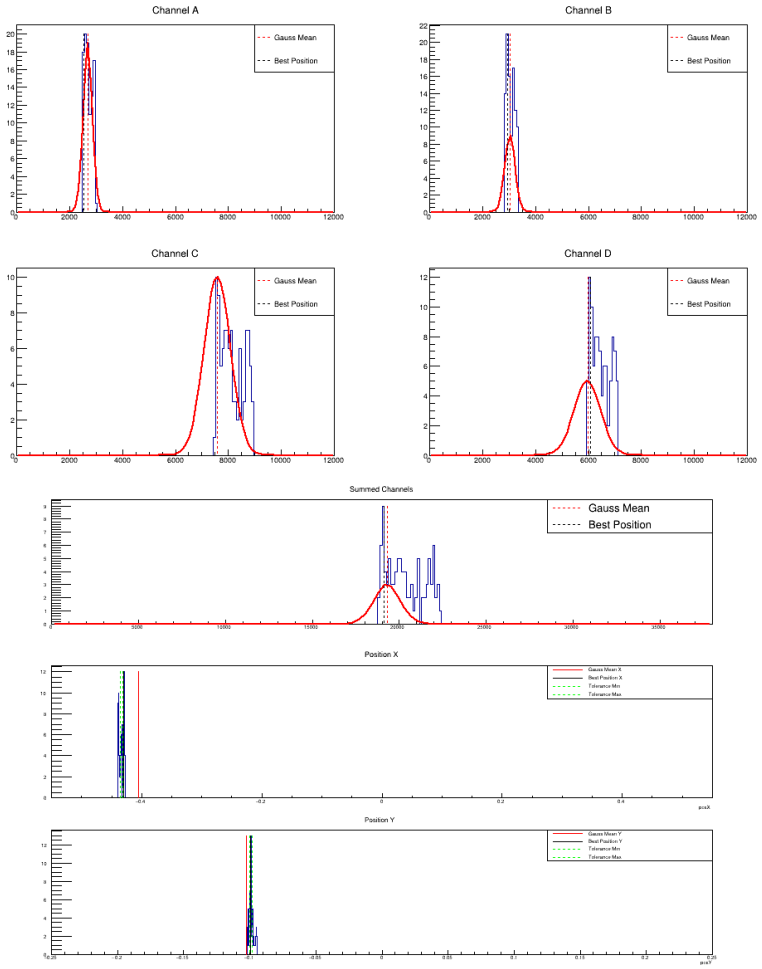

Figure 5.23: Fitted energy spectra and position distributions for pixel (1,6), 3rd Layer (edge pixel). Limited statistics and spectral distortion. X-axes: channel value or position [a.u.]; Y-axes: event counts.

5.3.6 Limitations in Spectral Characterization and the Role of Back-Irradiation

Despite the overall effectiveness of the spectral fitting methodology, several limitations emerged during the analysis, particularly in regions with suboptimal signal characteristics. Two main problem areas were identified: pixels located at the edges of the detector matrix and the third scintillator layer.

Edge Pixel Limitations. Edge pixels—defined here as the first and last two rows and columns of the detector matrix—exhibited notable degradation in spectral quality. These pixels consistently showed lower energy responses, likely due to light loss at the detector boundaries and less efficient optical coupling. As a result, the standard energy window filtering procedure, optimized for central pixels, proved too restrictive for edge pixels, excluding a significant fraction of valid events and thereby reducing statistical robustness.

To address this, a dedicated analysis was performed in which the energy window was temporarily disabled for edge pixels. This allowed for the retention of all recorded events and led to more complex but complete spectral distributions. Additional optimization of the peak-finding and fitting algorithms was required to handle the increased spectral complexity. Despite the added computational cost, this approach resulted in more reliable spectral characterization of edge pixels and enabled their inclusion in the final pixel database.

Challenges in the Third Scintillator Layer. Among the three scintillator layers, the third presented the greatest challenges for spectral characterization. The primary difficulty stems from the presence of multiple closely spaced and poorly resolved peaks in the spectral distributions. This makes it particularly difficult to reliably identify the true photopeak. A typical scenario involves observing two peaks in the individual channel spectra and multiple peaks in the total energy spectrum.

The current software handles this by first applying a peak identification algorithm, followed by fitting a single Gaussian to each detected peak. It then searches for a valid combination of one peak per channel that yields a reconstructed energy close to 511 keV and a spatial position compatible with the expected pixel centroid. However, in cases with multiple close peaks, this method often identifies several combinations that satisfy both energy and spatial constraints. As a result, the software frequently selects an incorrect combination, compromising the accuracy of the extracted spectral parameters.

An alternative approach tested involved fitting the channel spectra with double Gaussian functions to separately model overlapping peaks. While this method showed

some improvement when the peaks were clearly distinct, it frequently failed or produced unstable results in more ambiguous cases. Due to this inconsistency and high failure rate, the double Gaussian fitting approach was ultimately not adopted in the final analysis pipeline.

To explore potential improvements, a back-irradiation setup was tested using a ^{22}Na source placed behind the detector. This geometry maximized photon flux in the third layer, improving event statistics and minimizing the influence of upstream scattering. he resulting flood map (Figure 5.24) displayed improved contrast and pixel separation in the third layer, with an inverted brightness gradient compared to front irradiation.

Flood maps obtained under back-irradiation conditions (Figure 5.24 and Figure 5.25) demonstrated significantly improved brightness and pixel delineation in the 3rd Layer.

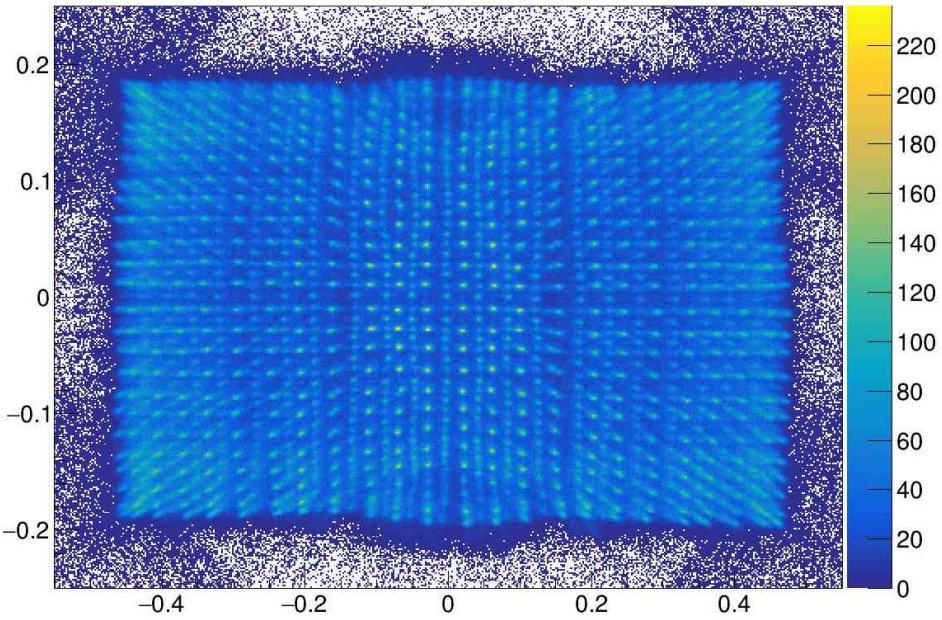

Figure 5.24: Flood map of detector 10 under ^{22}Na back-irradiation. Compared to front irradiation Fig. 5.10, enhanced pixel contrast and separation is evident in the third layer and reduced in the first and second layers.

Figure 5.26 shows the energy spectrum of ^{22}Na back-irradiation on detector 10 without coincidence filtering or energy selection. In contrast to the FDG spectrum (Figure 5.7), a shift toward lower energies is evident, along with a more prominent low-energy peak and tail. These features result from the absence of coincidence filtering, which allows for increased contributions from scattered and background events.

Spectral comparisons between FDG front-irradiation and ^{22}Na back-irradiation data (Figure 5.27) reveal improved peak sharpness and symmetry in the back-irradiation case, accompanied by reduced fitting uncertainties.

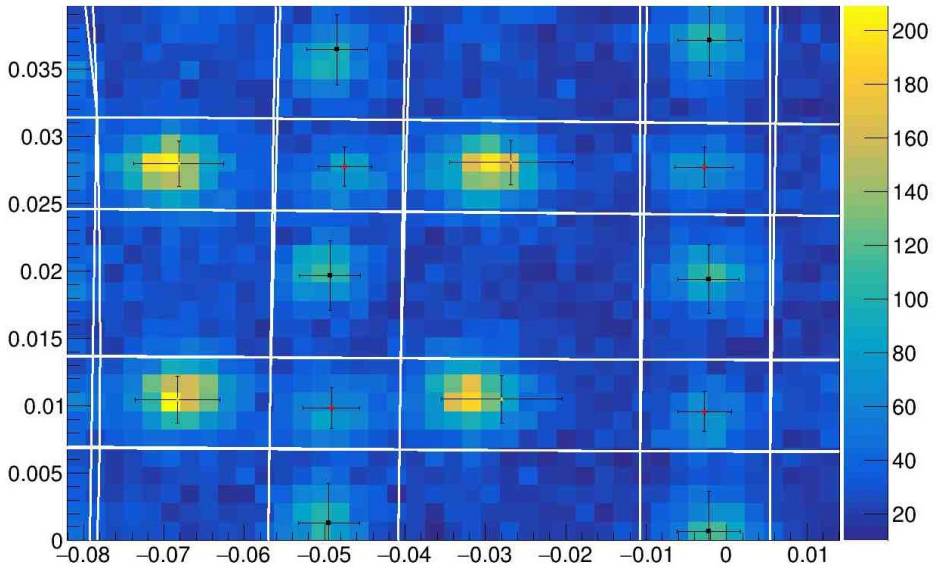

Figure 5.25: Zoomed flood map of detector 10 under back-irradiation with a ^{22}Na source. Compared to front irradiation (see Fig. 5.12), the third scintillator layer appears brighter than the first and second layers. Black, red, and yellow dots with error bar indicate pixels assigned to the first, second, and third layers, respectively.

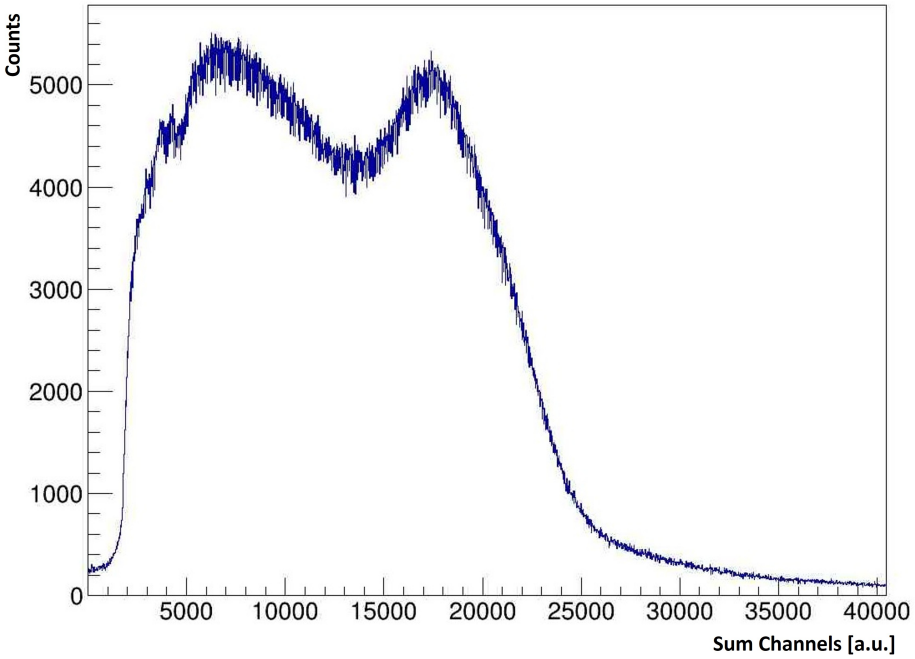

Figure 5.26: Energy spectrum of detector 10 under ^{22}Na back-irradiation. No coincidence or energy filter applied.

However, these improvements come with caveats. The back-irradiation dataset differs from standard acquisition protocols:

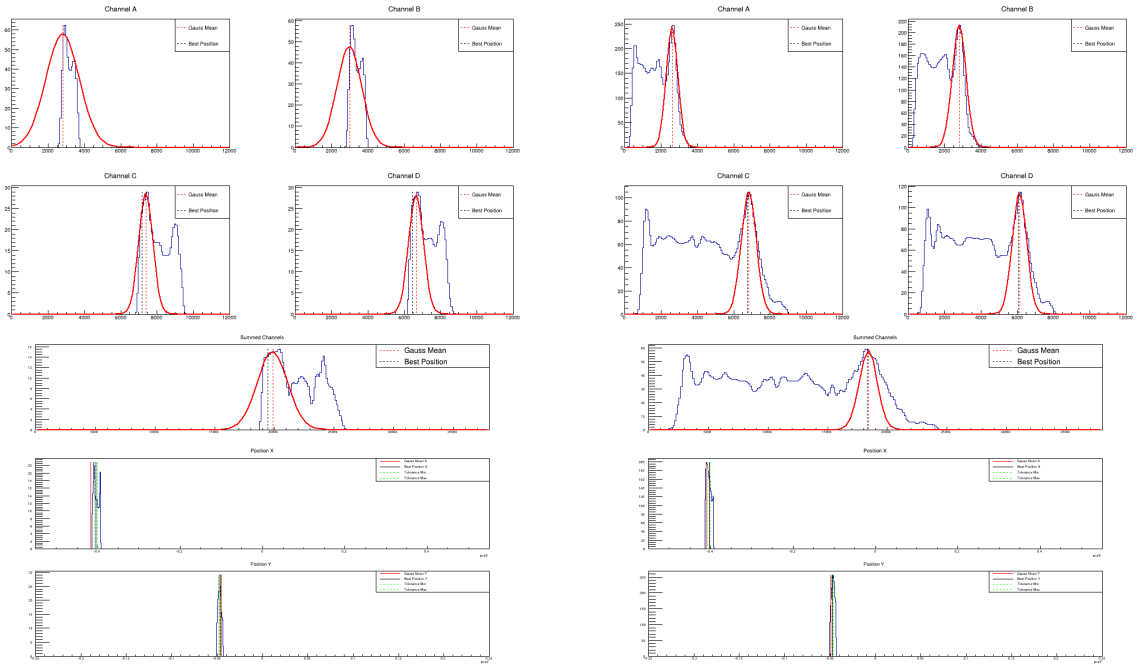

(a) FDG front-irradiation

(b) ^{22}Na back-irradiation

Figure 5.27: Comparison of third-layer energy spectra for pixel (2,9): FDG front-irradiation vs. ^{22}Na back-irradiation. The latter shows sharper and more symmetric peaks, indicating improved spectral conditions.

- Coincidence filtering could not be applied, as the geometry did not allow reliable detection of photon pairs.
- Energy window filtering was excluded due to the shift in energy scale caused by the different irradiation geometry and increased light yield.
- Consequently, the spectra are more susceptible to background contributions, including scatter and intrinsic activity (e.g., from ^{176}Lu in LYSO).

To align the energy scales between FDG and back-irradiation data, a normalization factor was computed by comparing the 511 keV peak positions in central pixels. This yielded an average scaling factor of approximately 1.117. Although this correction improved dataset compatibility, it was based on limited statistics and manual validation. Its robustness remains uncertain and must be interpreted with caution.

Given these constraints, the benefits of the back-irradiation method are limited. While it offers a qualitative enhancement in peak visibility for pixels in the third layer, its practical utility remains uncertain. The extracted parameters were analyzed and compared, but the actual advantage of this method over standard acquisition could not be clearly demonstrated. This is discussed further in Chapter 6.

Chapter 6

Data Analysis and Results

This chapter presents a comprehensive characterization of the high-resolution Depth-of-Interaction (DOI) detector for the Small Animal In-Beam PET Scanner, based on both experimental and simulated data. It is organized into three sections, each targeting a specific aspect of detector performance.

The first section (Section 6.1) covers the pixel-wise analysis of experimental data from FDG measurements. It outlines the processing pipeline for extracting spatial centroids and energy response parameters, and highlights challenges encountered in edge pixels and deeper scintillator layers.

The second section (Section 6.2) explores the detector response through Monte Carlo simulations. It characterizes interaction multiplicity, energy deposition, and spatial dispersion, providing insight into inter-crystal scattering and photon transport mechanisms.

The third section (Section 6.3) evaluates how the extracted pixel-wise parameters can be used to reconstruct synthetic detector signals and apply event filtering. The analysis supports their role in improving localization accuracy and lays the groundwork for integration into advanced reconstruction strategies.

6.1 Detector Pixel-wise Characterization: Workflow, Results, and Limitations

This section presents the results of the pixel-wise characterization of the SIRMIO PET detector. Building upon the data processing and filtering methodologies introduced in Chapter 5, the focus is placed on the quantitative evaluation of the spatial and spectral parameters extracted for each detector pixel. The overarching objective is to generate a high-fidelity, pixel-specific parameter map capable of accurately describing the detector response. Such a database is intended to support event classification, filtering, and

simulation-based modeling for image reconstruction.

Each pixel (j, k) is characterized by its centroid coordinates $(\bar{x}, \bar{y})_{j,k}$ and spatial spreads $(\sigma_x, \sigma_y)_{j,k}$, derived from the analysis of the flood map using spatial filters and statistical analysis of the event distributions. These spatial descriptors provide a compact and statistically meaningful representation of the photon interaction positions within the detector plane.

The subsequent subsections analyze the spatial and spectral distributions of the extracted parameters, assess their pixel-to-pixel variability across layers, and quantify the fraction of pixels for which the characterization procedure either failed or required correction. Special attention is given to the limitations observed in the third layer, where statistical limitations and decreased sensitivity posed significant challenges.

6.1.1 Spatial Pixel Characterization Analysis

The spatial characterization of each pixel in the flood map was carried out by extracting the centroid coordinates $(\bar{x}, \bar{y})$ and corresponding spatial spreads (σ_x, σ_y) from the event distributions. This analysis was performed on the FDG dataset and applied to all layers of detector 10. To investigate the spatial dependence of the detector performance, pixels were systematically grouped into central and edge regions.

Table 6.1 reports the statistical distribution of the extracted spread parameters. As anticipated, central pixels exhibited narrower and more consistent spatial spreads, indicative of higher light collection uniformity and reduced edge-related effects. Conversely, edge pixels displayed increased variability and broader distributions, likely due to boundary reflections, reduced photon statistics, and less favorable light-propagation conditions.

A systematic anisotropy was consistently observed across layers, with typical values of $\sigma_x \approx 2\sigma_y$. This asymmetry is attributed to the geometric configuration of the SiPM array and the anisotropic coupling of scintillation light within the detector module.

To validate the accuracy of the extracted centroids and their associated spread parameters, the reconstructed pixel positions were overlaid on the original filtered flood map, as illustrated in Figure 6.1. The close alignment between the computed centroids and the observed pixel clusters confirms the precision of the spatial characterization procedure.

Table 6.1: Spatial resolution statistics (σ_x, σ_y) across layers and pixel regions.

Metric	Layer	Region	Mean	Std	Min	Max
σ_x	0	central	0.00360	0.00017	0.00332	0.00438
		edge	0.00422	0.00062	0.00341	0.00574
	1	central	0.00389	0.00022	0.00346	0.00473
		edge	0.00423	0.00046	0.00337	0.00537
	2	central	0.00695	0.00152	0.00440	0.01221
		edge	0.00480	0.00190	0.00130	0.00995
σ_y	0	central	0.00155	0.00006	0.00145	0.00181
		edge	0.00183	0.00043	0.00145	0.00422
	1	central	0.00241	0.00062	0.00090	0.00507
		edge	0.00285	0.00100	0.00098	0.00630
	2	central	0.00181	0.00012	0.00161	0.00236
		edge	0.00212	0.00079	0.00115	0.00463

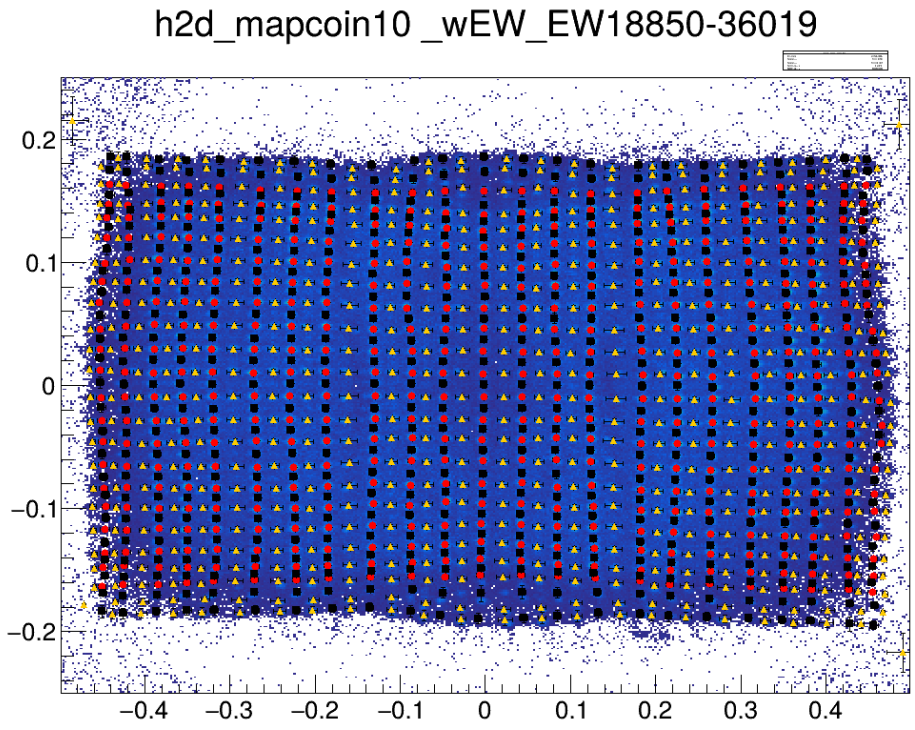

Figure 6.1: Flood map of detector 10 with overlaid pixel centroids.

Flood Map Reconstruction

To verify the accuracy and representativeness of the extracted spatial parameters, a synthetic flood map was reconstructed using solely the spatial centroids $(\bar{x}, \bar{y})$ and spreads (σ_x, σ_y) obtained from the pixel-wise analysis. Each pixel p was modeled as a two-dimensional Gaussian distribution:

$$G_p(x, y) = \frac{1}{2\pi\sigma_x\sigma_y} \exp\left[-\left(\frac{(x-\bar{x})^2}{2\sigma_x^2} + \frac{(y-\bar{y})^2}{2\sigma_y^2}\right)\right] \tag{6.1}$$

From each pixel distribution, 10,000 synthetic events were randomly sampled, assuming a uniform contribution across all pixels. These generated (x, y) coordinates were accumulated into a two-dimensional histogram to form the reconstructed flood map.

As illustrated in Figure 6.2, the resulting synthetic flood map closely reproduces the spatial structure observed in the experimental data, highlighting the detector's regular pixel arrangement and spatial resolution profile.

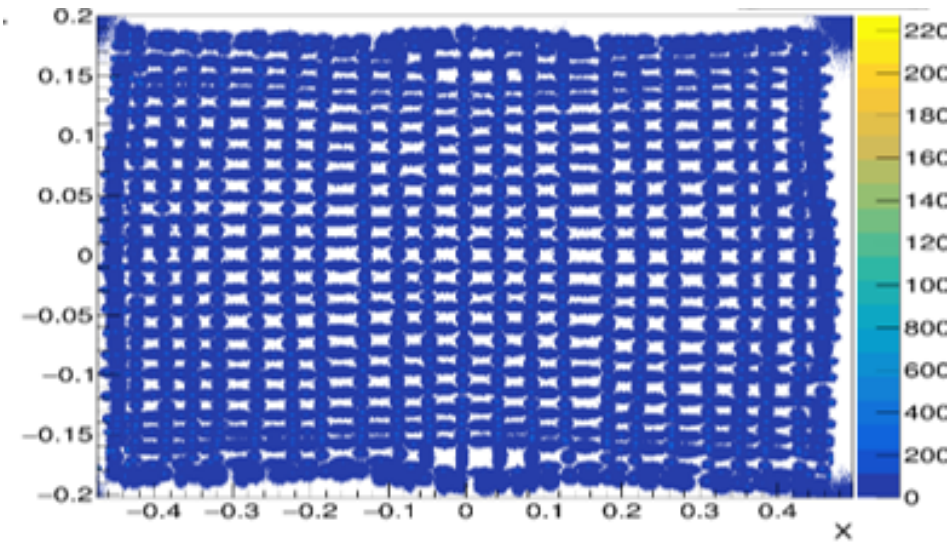

Figure 6.2: Synthetic flood map reconstructed using Gaussian-distributed events centered at each pixel's spatial centroid.

6.1.2 Spectral Parameter Analysis

To characterize the energy response of each pixel, spectral analysis was performed independently on the signals from the four readout channels ch_i, with $i \in \{0, 1, 2, 3\}$. This channel-wise approach avoids the limitations of the total energy spectrum, which is often distorted by pile-up, trigger asymmetries, and inter-crystal scattering (ICS). By fitting each channel spectrum individually with a Gaussian function, the peak position μ_{ch_i} and the corresponding standard deviation σ_{ch_i} were extracted.

The total reconstructed energy deposited in each pixel was then defined as the sum of the channel peak positions:

$$\mu_E = \sum_{i=0}^{3} \mu_{ch_i} \tag{6.2}$$

with an associated uncertainty given by the sum of the squared individual standard deviations:

$$\sigma_E = \sqrt{\sum_{i=0}^{3} \sigma_{ch_i}^2} \tag{6.3}$$

This model assumes that the channels respond linearly and independently, and that events are free from significant scattering or electronic noise. Under such conditions, μ_E is expected to align with the 511 keV photopeak.

To monitor the reliability of the spectral fitting process, a diagnostic log was generated for each pixel, reporting the number of identified peaks, the convergence status, and the number of iterations required. Failures—typically caused by low statistics or ambiguous peak structures—were flagged accordingly. In the FDG dataset, which was filtered by an energy window to suppress background, fitting failures were observed in six pixels: one in the second layer and five in the third layer. These were excluded from the final database.

The distributions of the extracted standard deviations σ_{ch_i} and the total energy resolution σ_E are shown in Figure 6.3. A clear degradation in energy resolution is observed from the first to the third layer. This trend reflects the combined effects of light attenuation and increasing contributions from ICS events in deeper detector regions, resulting in broader and less reliable spectral peaks.

Elevated sigma values are generally linked to edge pixels and the third layer, suggesting statistical constraints and spatial inconsistencies. High sigma indicates a broad distribution of 511 keV, meaning reduced energy resolution and energy degradation. Additionally, variability in sigma values indicates a high degree of spectral dependence, as well as underlying limitations and issues. This affects the detectability of peaks and the reliability of spectral parameters at the pixel level.

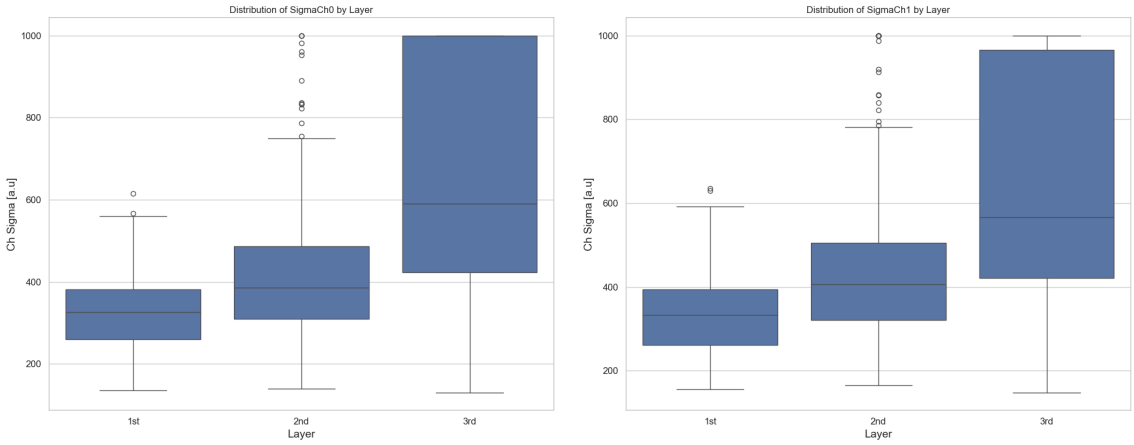

(a) σ_{ch_0}

(b) σ_{ch_1}

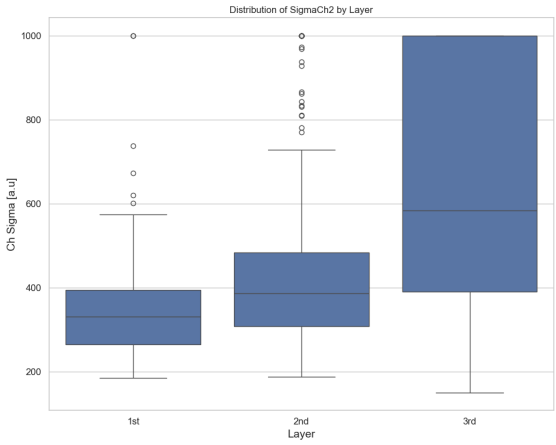

(c) σ_{ch_2}

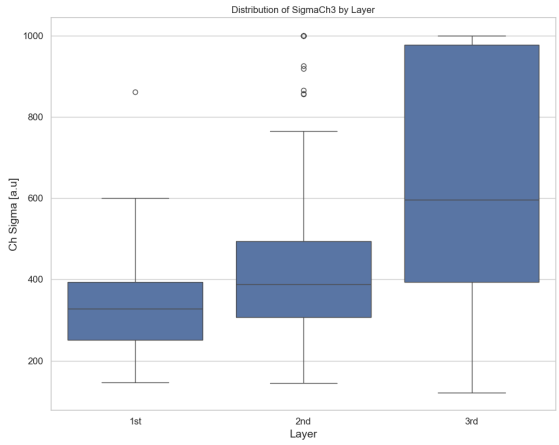

(d) σ_{ch_3}

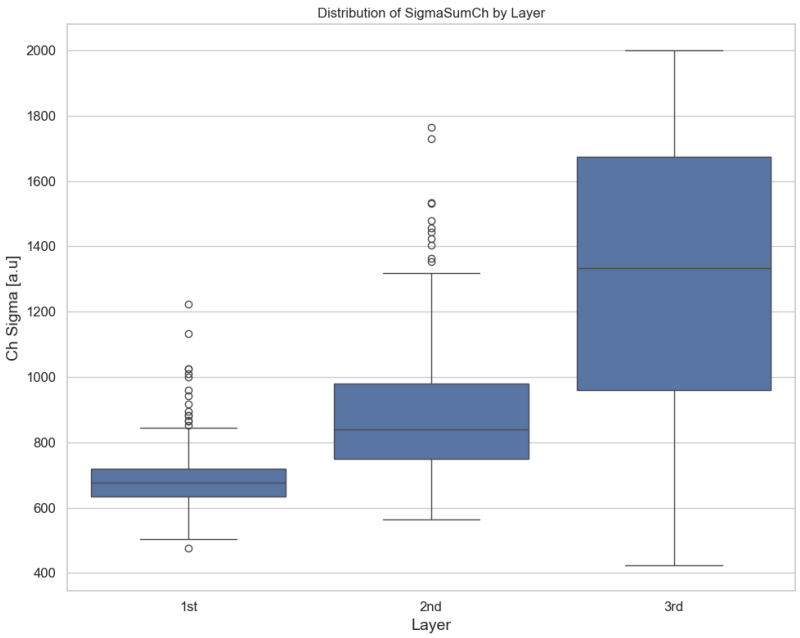

(e) σ_E

Figure 6.3: Distributions of σ in layers for each readout channel and for energy.

Energy Map and Pixel-wise Energy Distribution Further analysis focused on the mean energy per pixel (μ_E), extracted from the sum of channel peaks. 2D energy distributions are shown in Figure 6.4, accompanied by row-wise projections in Figure 6.6. These profiles highlight pixel-to-pixel variations and reveal systematic pattern across the detector.

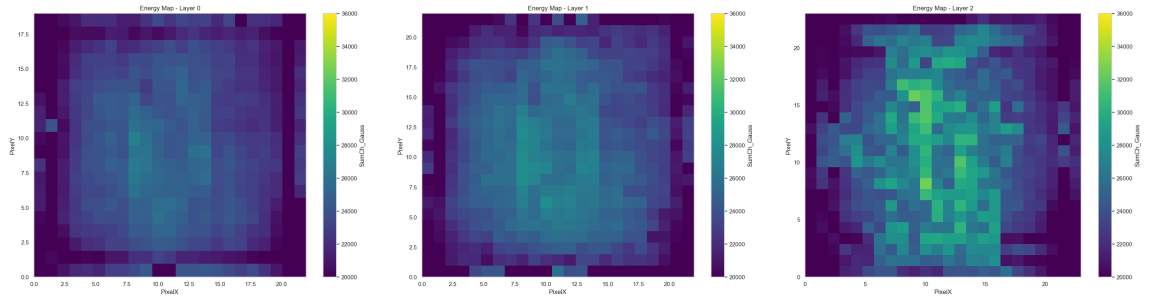

(a) 1st Layer (b) 2nd Layer (c) 3rd Layer

Figure 6.4: Pixel energy (μ_E) maps for each layer showing the pixel-wise μ_E extracted.

A histogram of pixel energy for all pixels is shown in Figure 6.5, summarizing the layer-wise energy evolution.

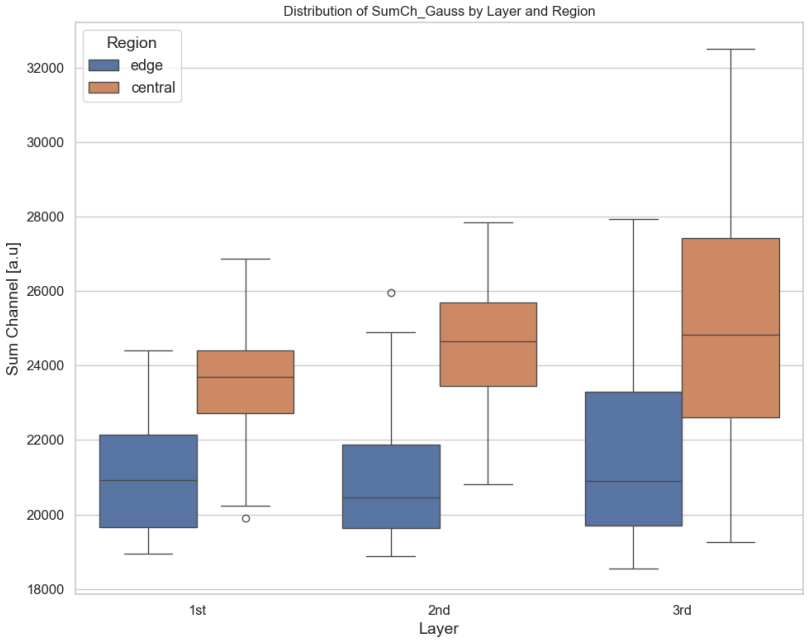

Figure 6.5: Distribution of pixel energy (μ_E) extracted from pixel-wise Gaussian fits from FDG.

As expected, we observe an increase in energy response in the second and third layers, as well as considerable variability under light dependence and pronounced inconsistencies in the third layer, likely due to increased ICS. In particular, the third layer

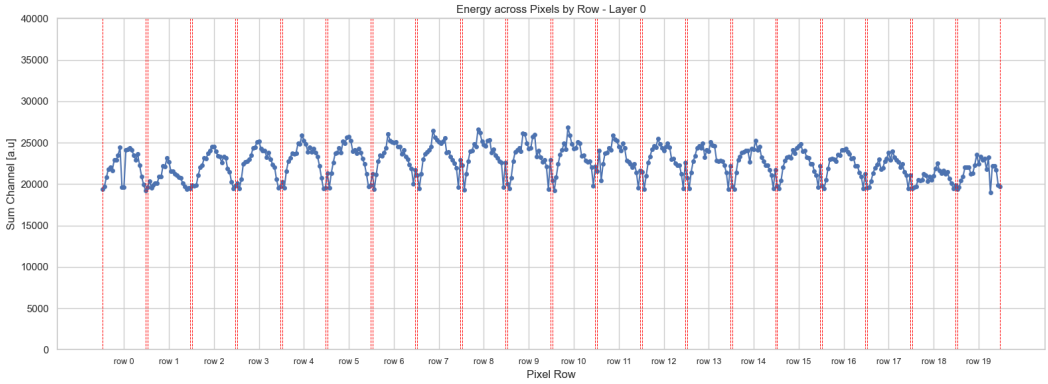

(a) 1st Layer

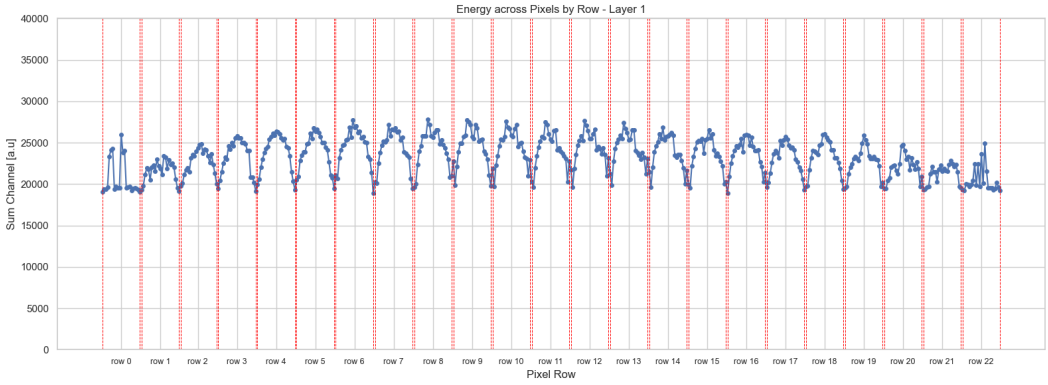

(b) 2nd Layer

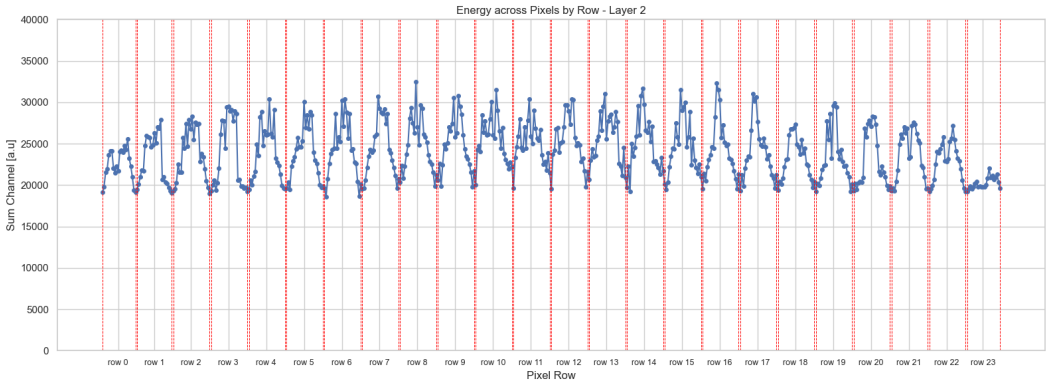

(c) 3rd Layer

Figure 6.6: Row-wise pixel energy (μ_E) evolution for each layer. The red line separates pixel rows for visual inspection.

exhibits abrupt pixel-to-pixel variations, with certain rows showing non-monotonic energy trends and localized deviations from the expected gradient. These variations suggest reduced spectral reliability for some pixels in the third layer. This is likely caused by a combination of contamination from inter-crystal scattering and limited statistics, which lead to less accurate peak fitting.

Performance Evaluation via Position Error and Pixel Quality Metrics

To quantitatively assess the reliability of the spectral characterization process, we evaluated the consistency between spatial and spectral reconstructions and implemented systematic criteria for identifying potentially problematic pixels.

A central validation step involved comparing the reconstructed pixel positions derived from channel-based Gaussian peak fitting to those obtained from the flood map analysis $(\bar{x}, \bar{y})_{experimental}$. Using the peak positions $(\mu_{ch_0}, \mu_{ch_1}, \mu_{ch_2}, \mu_{ch_3})$ extracted for each channel, the reconstructed pixel position $(x, y)_{ch}$ was estimated via the Anger logic:

$$x_{ch} = \frac{\mu_{ch_0} + \mu_{ch_1} - \mu_{ch_2} - \mu_{ch_3}}{\mu_{ch_0} + \mu_{ch_1} + \mu_{ch_2} + \mu_{ch_3}}, \quad y_{ch} = \frac{\mu_{ch_0} - \mu_{ch_1} - \mu_{ch_2} + \mu_{ch_3}}{\mu_{ch_0} + \mu_{ch_1} + \mu_{ch_2} + \mu_{ch_3}} \tag{6.4}$$

The relative errors between the channel-based and flood map-derived positions are then defined as:

$$\text{PosErr}_X = \left| \frac{x_{ch} - x_{experimental}}{x_{experimental}} \right| \cdot 100, \quad \text{PosErr}_Y = \left| \frac{y_{ch} - y_{experimental}}{y_{experimental}} \right| \cdot 100 \tag{6.5}$$

The distributions of these position errors are shown in Figure 6.7. While the majority of pixels demonstrate good agreement (typically within 5%), a notable tail exceeding 10% appears, particularly among peripheral pixels and in the third detector layer. These deviations likely stem from spectral misidentification or limited photon statistics.

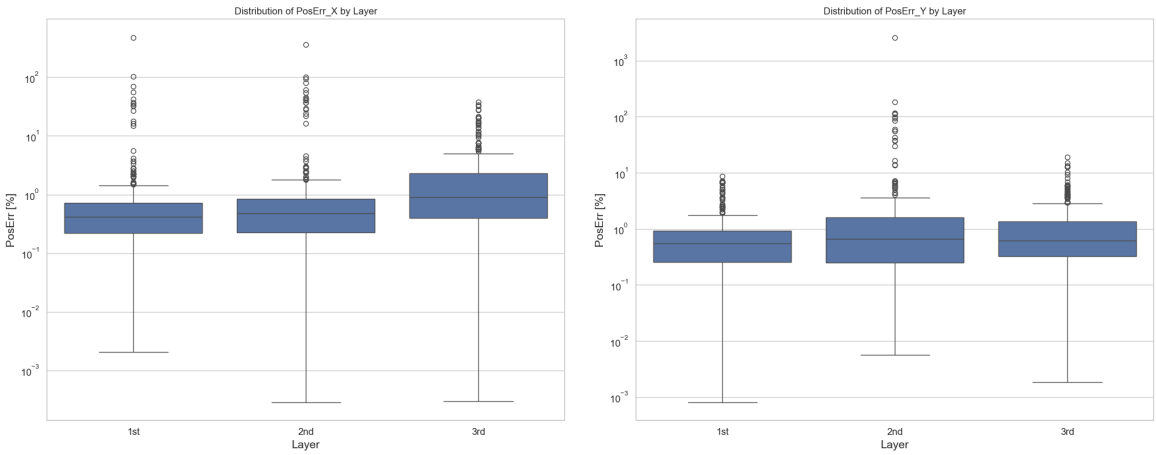

Figure 6.7: Distributions of relative position errors along X (left) and Y (right) for central pixels. Values above 10% are flagged for review.

To improve the reliability of the pixel parameter database, we defined a set of criteria to flag pixels exhibiting anomalous behavior, using both absolute thresholds and statistical outlier detection.
A pixel was flagged to be review if it satisfied at least one of the following conditions:

- **Threshold-based conditions**:

  - Energy centroid μ_E outside nominal range: $\mu_E < 10{,}000$ or $\mu_E > 40{,}000$
  - Position error exceeding tolerance: $\text{PosErr}_X > 10\%$ or $\text{PosErr}_Y > 10\%$

- **Statistical outliers** (based on 3σ criterion within each detector layer and region category):
  - Channel width deviations: σ_{ch_0} to σ_{ch_3}
  - Energy resolution σ_E
  - Relative position errors PosErr_X, PosErr_Y

Pixels meeting any of these criteria were flagged for exclusion or subject to further refinement via manual review. A summary of the flagged pixels per detector layer is provided in Table 6.2. It is important to note that a flagged status does not inherently imply a definitive failure in pixel characterization but rather indicates the need for closer scrutiny. The actual number of functionally unusable pixels may be underestimated due to ambiguity in peak attribution.

Table 6.2: Summary of flagged pixels per detector layer.

Layer	**Flagged Pixels**	**Total Pixels**	**Percentage**
1st	10	460	2.2%
2nd	32	529	6.0%
3rd	80	576	14.2%
Total	**122**	**1565**	**7.8%**

Manual inspection confirmed that the spectral characterization in layers 1st and 2nd was generally reliable, with reported pixels observed near the detector edges. In contrast, a significantly higher rate of unreliable pixels was found in the third layer, primarily due to the frequent presence of multiple spectral peaks within single-pixel spectra. As previously discussed, this effect compromises the ability to unambiguously assign a unique response to a given pixel, resulting in a much larger proportion of flagged cases.

Synthetic Flood Map Reconstruction

To further validate the reliability of the extracted spectral descriptors and explore their potential in modeling the spatial response of the detector, a second synthetic flood map reconstruction was performed based on channel-level information.

For each pixel and each channel i, the response S_{ch_i} was modeled as a one-dimensional Gaussian distribution:

$$S_{ch_i} \sim \mathcal{N}(\mu_{ch_i}, \sigma_{ch_i}) \tag{6.6}$$

Synthetic events were generated by independently sampling from the distributions $S_{ch_0}, S_{ch_1}, S_{ch_2}, S_{ch_3}$. The spatial coordinates of each synthetic event were then computed using the standard Anger logic formula:

$$x = \frac{S_{ch_0} + S_{ch_1} - S_{ch_2} - S_{ch_3}}{S_{ch_0} + S_{ch_1} + S_{ch_2} + S_{ch_3}}, \qquad y = \frac{S_{ch_0} - S_{ch_1} - S_{ch_2} + S_{ch_3}}{S_{ch_0} + S_{ch_1} + S_{ch_2} + S_{ch_3}} \tag{6.7}$$

These coordinates were accumulated into a 2D histogram representing the reconstructed flood map.

Figure 6.8 shows the resulting synthetic flood map generated directly from the raw channel parameters. The image reveals that the reconstructed spots are considerably broadened and spatially overlapped, resulting in a poorly resolved structure where individual pixels are no longer clearly distinguishable. This blur arises from the substantial spreads σ_{ch_i} associated with each channel and the complete neglect of inter-channel correlations. As a consequence, this reconstruction leads to a strong overestimation of spatial uncertainty.

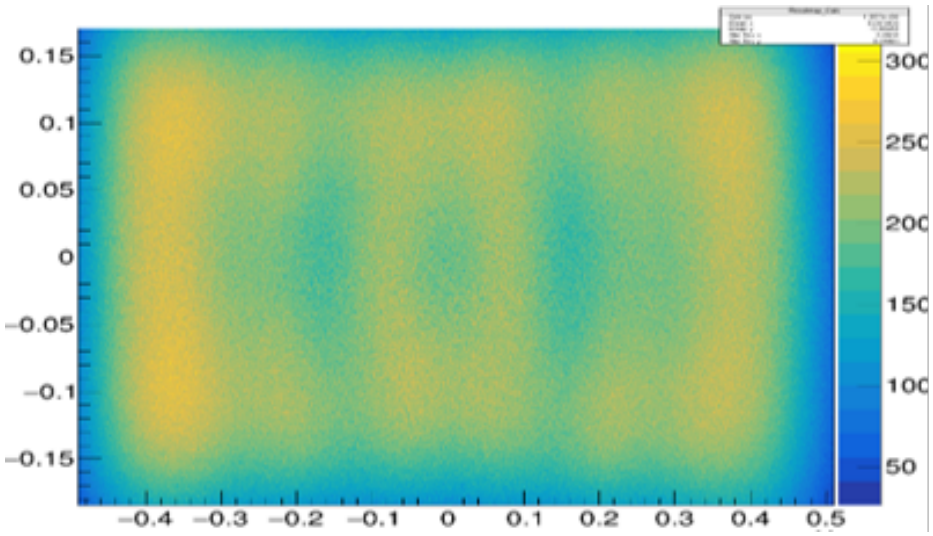

Figure 6.8: Synthetic flood map reconstructed using raw channel parameters without correction.

Deriving a full statistical model that captures the underlying correlation structure between channels is inherently complex, as it requires knowledge of the joint distribution of signal across all four channels. These correlations arise from a combination of optical crosstalk, geometrical asymmetries, and statistical dependencies in light transport. In this preliminary study, such effects were not incorporated, and channels signal were

assumed to be independent. While this assumption simplifies the modeling process, it limits the descriptive accuracy of the resulting spatial response.

To mitigate this limitation and better approximate the observed detector response, an empirical correction was applied. Specifically, the channel-wise standard deviations σ_{ch_i} were scaled by a factor $f = 1/15$, determined through iterative testing to visually match the spatial resolution of the experimental flood map. This corresponds to reduced σ_{ch_i} values in the range of approximately 20 to 60, depending on the original spread of each channel. It is important to emphasize that this correction factor is purely indicative and serves only to illustrate the magnitude of adjustment needed. It does not represent a comprehensive model of the underlying inter-channel correlations, which likely vary across pixels and depend on the complex interplay of light transport, detector geometry, and electronic response. The corresponding reconstruction is shown in Figure 6.9. This adjusted synthetic flood map demonstrates improved localization and sharper pixel boundaries, indicating that the empirical narrowing of channel spreads can partially compensate for the missing inter-channel covariance.

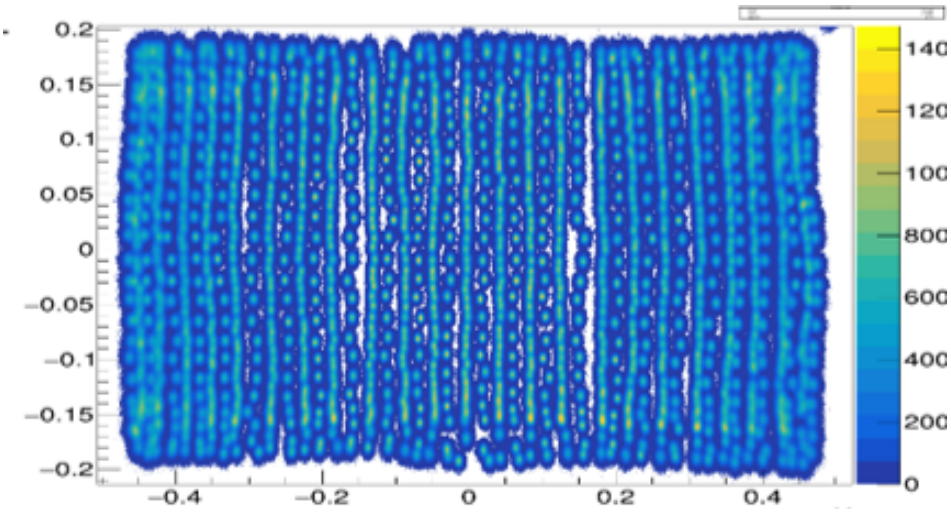

Figure 6.9: Synthetic flood map reconstructed using rescaled channel parameters ($\sigma_{ch_i}/15$).

Despite this visual improvement, notable discrepancies remain. In particular, the reconstructed spots appear isotropic, lacking the elongated morphology ($\sigma_x \approx 2\sigma_y$) observed in the experimental data. This discrepancy stems from the symmetric treatment of channel contributions and the absence of a transformation model that captures the anisotropic propagation of scintillation light within the detector. These findings emphasize the limitations of using uncorrelated Gaussian models and motivate the need for a more refined statistical framework that explicitly incorporates channel interdependencies.

In summary, channel-based flood map reconstruction can serve as a useful tool for

qualitative evaluation of spectral parameters. However, its quantitative accuracy is currently constrained by the simplifying assumptions of statistical independence and isotropy.

6.1.3 Comparison with Back Irradiation Using Na^{22}

To address the challenges in spectral characterization, particularly the reduced statistics and increased inter-crystal scattering (ICS) observed in deeper detector layers with front-irradiation (FDG) data, a complementary dataset was acquired using a ^{22}Na source in a back-irradiation configuration, as detailed in Chapter 5. This geometry facilitated more homogeneous illumination of the third detector layer.

The ^{22}Na acquisition generally yielded improved spectral characterization quality. Notably, the occurrence of multiple spectral peaks was significantly reduced, and pixel coverage in the third layer improved. The distributions of the reconstructed energy peaks (μ_E) and corresponding energy resolutions (σ_E) were observed to be narrower and more uniform, as illustrated in Figure 6.10. These distributions can be directly compared with the FDG-derived results presented in Figures 6.5 and 6.3.

A representative comparison of the energy spectra for pixel (2,9) in the second layer (as shown in Figure 5.27) further highlights this improvement. The ^{22}Na spectrum consistently exhibits a cleaner and more distinct photopeak structure compared to the FDG spectrum, which often suffers from higher background noise and less defined peaks.

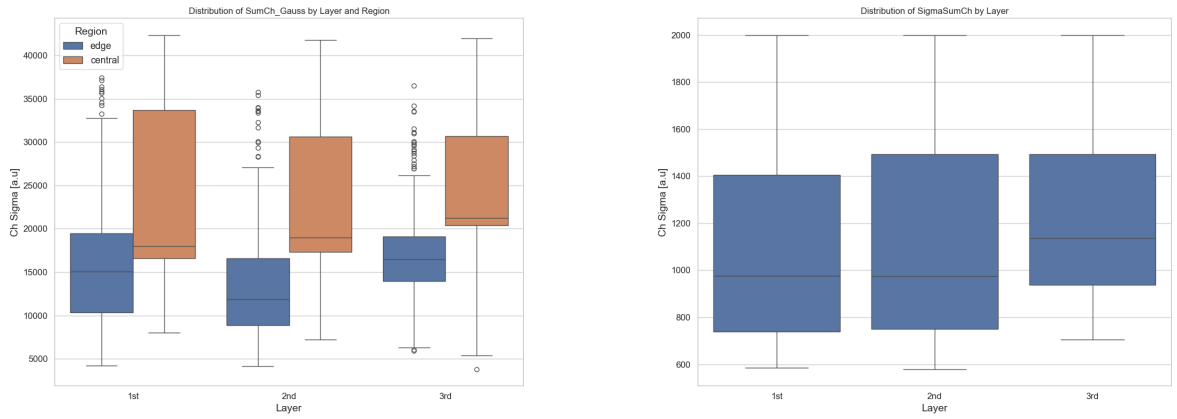

(a) μ_E (b) σ_E

Figure 6.10: Pixel-wise spectral parameters from ^{22}Na back-irradiation: (a) distribution of energy peak positions (μ_E); (b) distribution of energy resolution (σ_E).

Despite the advantages in spectral quality, the current implementation of ^{22}Na back-irradiation for routine detector calibration faces several significant practical limitations:

- Fitting Failures: Twelve pixels, primarily located at the detector's periphery,

exhibited insufficient statistics, leading to unreliable or failed spectral fitting outcomes.

- Absence of Coincidence Filtering: The experimental setup precluded reliable coincidence filtering, thereby increasing the susceptibility of the collected spectra to background noise and scattered events.

- Susceptibility to Contamination: Without the ability to apply an energy window filter (due to potential energy scale shifts from varying light yield and photon incidence angles), spectra were more prone to contamination from Compton scatter and intrinsic radioactivity, such as ^{176}Lu in LYSO crystals.

- Integration Challenges with FDG Data: Integrating ^{22}Na data into the existing FDG-based processing pipeline is complex. It necessitates an accurate calibration factor to align energy scales, but reliably identifying the 511 keV photopeak in low-statistics FDG data can be ambiguous.

- Scalability: Applying this detailed characterization procedure across all 56 detector blocks would demand substantial manual intervention and calibration, rendering large-scale implementation impractical.

While the parameters derived from the ^{22}Na method supported the analysis within this thesis, they were not adopted as the primary replacement for the FDG-derived values for third layer characterization due to the mentioned limitations. Nevertheless, ^{22}Na back-irradiation demonstrates clear potential as a valuable reference or calibration dataset, particularly for optimizing spectral parameter extraction in the more challenging rear layers of the detector. Further study and refinement are essential to overcome its current limitations before full integration into future processing workflows can be realized.

6.2 Detector Response Simulation

This section provides a detailed characterization of the simulated response of the detector to 511 keV annihilation photons, based on the simulation framework presented in Chapter 4. A total of 10^6 photons were simulated to investigate interaction multiplicity, spatial distributions, and energy deposition patterns across the three scintillator layers.

The overarching aim of this analysis is to evaluate the key interaction characteristics of 511 keV photons within the detector volume. In particular, we focus on the multiplicity of interactions, energy deposition behavior, and the spatial correlations between

interaction points. This evaluation is crucial for understanding the impact of inter-crystal scattering (ICS) and for informing the development of robust event selection and correction strategies.

6.2.1 Interaction Multiplicity

We first categorized simulated events according to the number of energy depositions (i.e., interactions) recorded for each primary photon. Here, an *event* refers to the full chain of interactions produced by a single 511 keV photon within the detector. Out of 688,369 unique primary photons that interacted with the detector, a significant portion resulted in multiple energy depositions.

The distribution of interaction multiplicity is summarized in Figure 6.11 and detailed in Table 6.3. As observed, single-interaction events are the most frequent category, accounting for 53.46% of all recorded events. However, a substantial 46.54% of events involve two or more interactions. This high incidence of multiple-hit events is predominantly due to Compton scattering, which is the dominant interaction mechanism for 511 keV photons in LYSO. The probability of an event having a higher number of interactions decreases progressively, with triple-interaction events (11.46%) being significantly more common than those with four or more interactions (2.82%). The prevalence of multi-interaction events underscores the necessity of an effective event reconstruction strategy to accurately determine the total energy deposition and the initial point of interaction.

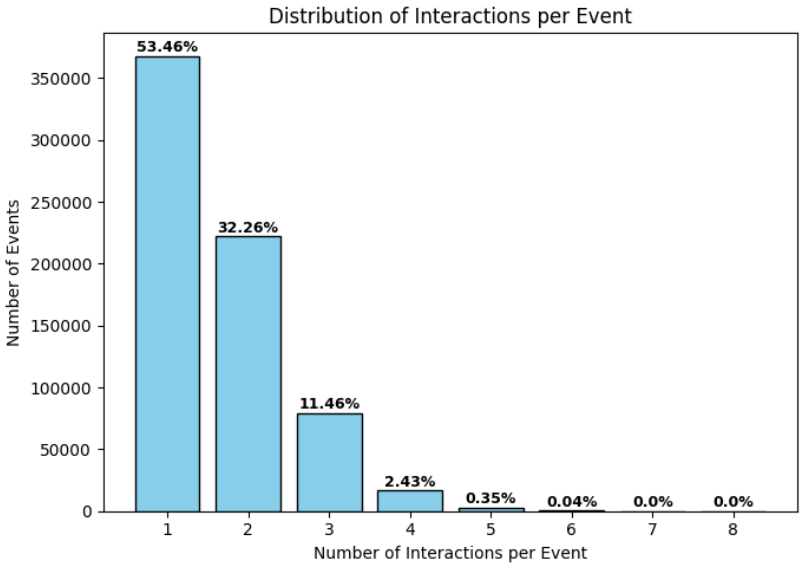

Figure 6.11: Distribution of the number of interactions per event for 688,369 simulated 511 keV gamma rays. Percentages indicate the fraction of total events for each multiplicity.

Table 6.3: Detailed distribution of interaction multiplicity.

Interactions per Event	Number of Events	Percentage
1	367,984	53.46%
2	222,067	32.26%
3	78,880	11.46%
4 or more	19,438	2.82%
Total	**688,369**	**100.00%**

6.2.2 Energy Deposition Analysis

The analysis of energy deposition within the detector is fundamental to accurately interpreting photon interactions. Figure 6.12 presents a stacked histogram depicting the energy deposition spectra categorized by interaction multiplicity and sequential interaction order. Different color coding highlights single interactions, as well as the first, second, and third interactions within multiple-interaction sequences.

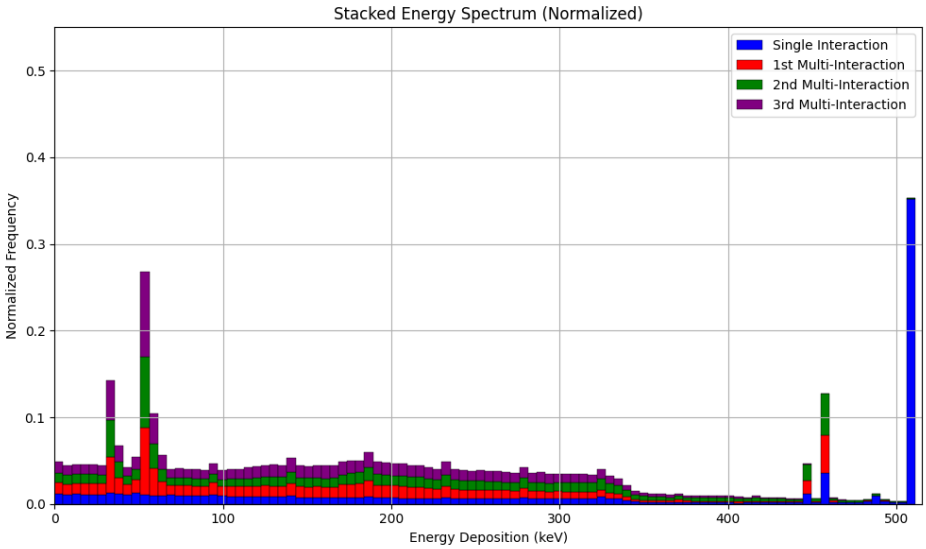

Figure 6.12: Stacked energy deposition spectrum, showing distinct contributions from single interactions and successive interactions in multiple-event sequences.

The key spectral features identified from the simulated detector response include:

- **Photopeak at 511 keV**: This peak predominantly arises from full energy deposition through the photoelectric effect, indicative of ideal PET photon interactions.
- **Compton Continuum**: A broad spectrum observed at lower energies, resulting from partial energy deposition during Compton scattering, where photons either escape the detector or undergo subsequent interactions.

- **Characteristic X-ray Peaks (50–60 keV)**: Produced by photoelectric interactions within the lutetium atoms of the LYSO scintillator, these peaks result from characteristic X-rays fully absorbed within the detector.

- **Escape Peaks (approximately 450–460 keV)**: These occur due to characteristic X-rays escaping the pixel detector volume, creating characteristic energy deficits relative to the photopeak.

Single-interaction events are predominantly represented by the photopeak at 511 keV, marking ideal-photon interactions. However, even these spectra include contributions from the Compton continuum, indicating scattered photons exiting the detector after partial energy deposition.

Multiple-interaction events involve photons interacting at multiple locations within the detector, typically due to inter-crystal scattering (ICS). ICS occurs when initial interactions deposit only part of the photon energy, generating scattered photons that subsequently interact again within the detector. This scattering significantly reduces the accuracy of reconstructing the initial interaction position, thereby negatively impacting detector spatial resolution.

Analysis of these spectra demonstrates that energy filtering can serve as a critical strategy to mitigate the impact of scattered photons. Applying a selective energy threshold around the 511 keV peak effectively reduces events primarily composed of scattered photons. Nevertheless, this filtering inherently removes not only a substantial number of multi-interaction events but also some single interactions and initial interactions of multi-event sequences, thereby precluding the reconstruction of the original photon interaction position for these events.

In the context of PET imaging, while energy filtering substantially enhances spatial resolution by excluding scattered and partially deposited events, it simultaneously introduces an inherent limitation: it reduces the total count of reconstructible events, including certain valid single and initial interaction events, reducing considerable the detector sensitivity.

6.2.3 Spatial Distribution and Inter-Layer Analysis

The three-layer design of the detector is intended to maximize the capture efficiency for both primary and scattered photons. The distribution of interactions across these layers provides insight into the detector's depth-of-interaction (DOI) capability.

Interaction Distribution per Layer

The distribution of interaction types within each detector layer provides insights into how 511 keV photons interact and propagate through the multi-layered detection system. Table 6.4 shows the percentage of each interaction type relative to the total number of events in that specific layer. The event categories include single-hit events (i.e., a single energy deposition), double-hit events (split into first and second interaction), triple-hit events (further divided into first, second, and third interaction), and a residual class named Other Events, which includes more complex cases.

Table 6.4: Percentage distribution of interaction types per detector layer. Values are relative to the total number of interactions recorded in each layer.

Interaction Type	1^{st} **Layer** [%]	2^{nd} **Layer** [%]	3^{rd} **Layer** [%]
Single interaction	33.8	29.1	35.4
Double - 1st interaction	23.6	19.3	14.4
Double - 2nd interaction	16.9	21.3	22.7
Triple - 1st interaction	9.1	7.1	3.7
Triple - 2nd interaction	6.0	8.0	7.1
Triple - 3rd interaction	4.6	7.9	9.3
Other Events	6.0	7.3	7.4

Single-hit events make up roughly one-third of the interactions in each layer, with the 3rd Layer showing the highest proportion (35.35%). This does not necessarily imply better photon absorption in deeper layers; rather, it may reflect scenarios where the photon undergoes Compton scattering and the secondary escapes the detector without further interaction.

Double-hit events show a decrease in first-interaction probability with increasing depth: 23.65% in 1st Layer, 19.27% in 2nd Layer, and 14.37% in 3rd Layer. Conversely, second interactions increase from 16.96% in 1st Layer to 22.72% in 3rd Layer. This confirms the tendency of scattered photons to migrate deeper into the detector, consistent with forward Compton scattering.

Triple-hit events further emphasize this trend. First hits are concentrated in the 1st Layer (9.14%), while second and third interactions are increasingly likely in the 2nd and 3rd Layers, culminating at 9.29% for third interactions in 3rd Layer. This spatial evolution supports a model of multiple energy depositions progressing deeper into the detector structure.

Distribution of Interaction Types Across Layers

While the previous section analyzed how interaction types are distributed within each layer, this section evaluates how each interaction type is distributed across the three layers. In other words, it examines where in the detector a given event category predominantly occurs. Table 6.5 reports the percentage distribution of each interaction category in the three layers, normalized by the total number of interactions of that type.

Table 6.5: Distribution of interaction types across the three detector layers. Percentages are calculated with respect to the total number of interactions for each category.

Interaction Type	1^{st} **Layer** [%]	2^{nd} **Layer** [%]	3^{rd} **Layer** [%]
Single interaction	40.2	30.9	29.0
Double - 1st interaction	46.6	33.9	19.5
Double - 2nd interaction	33.4	35.7	30.9
Triple - 1st interaction	50.7	35.0	14.3
Triple - 2nd interaction	33.2	39.6	27.2
Triple - 3rd interaction	25.3	39.2	35.5

The spatial distribution of single-hit events shows that 40% occur in the 1st Layer, confirming its role as the primary interaction interface. The share decreases in deeper layers (31% in 2nd Layer and 29% in 3rd Layer), aligning with the attenuation profile of 511 keV photons.

Double-hit and triple-hit events clearly illustrate the progression of interactions through the detector. First hits are predominantly recorded in the 1st Layer (47% and 51%, respectively), while second interactions peak in the 2nd Layer. Third interactions of triple events are most frequent in the 3rd Layer (36%). This layered shift reflects the typical trajectory of Compton-scattered photons, confirming a sequential energy deposition pattern.

These statistics emphasize the distinct but complementary roles of each detector layer: the 1st Layer is crucial for initial photon capture, while the 2nd and 3rd Layers play increasingly important roles in recording subsequent interactions. This knowledge is instrumental for reconstructing the full photon path and is particularly relevant for improving depth-of-interaction (DOI) algorithms, time-of-flight corrections, and spatial resolution in PET imaging systems.

Lateral Displacement

The lateral displacement between the first and second interaction points in multiple-interaction events is a critical parameter that directly impacts the intrinsic spatial resolution of the detector. In pixelated scintillator arrays, such as the LYSO-based system considered here, event positioning is typically derived from the location of energy deposition. However, when photons undergo Compton scattering, the position of the first interaction—ideally corresponding to the emission point—may be offset from subsequent interactions, thereby introducing spatial ambiguity.

Figure 6.13 presents the distribution of lateral displacements for second interaction points relative to the first, measured across both double- and triple-interaction events. The bin width is 0.9 mm, which corresponds precisely to the pitch of the scintillator pixels, allowing direct interpretation in terms of pixel units.

The simulation reveals a mean lateral displacement of 2.55 mm with a standard deviation of 2.54 mm. The majority of events (approximately 52%) are clustered within 1 to 2 pixels from the primary interaction (0.9-1.8 mm), and nearly 68% fall within 3 pixels (0.9–2.7 mm). This concentration near the origin suggests that, in most cases, the scattered photon interacts within a relatively small neighborhood, preserving the spatial localization of the original gamma-ray interaction.

Notheless, the histogram exhibits a noticeable tail, with a non-negligible percentage of events extending to larger displacements. For instance, about 5.3% of second interactions occur more than 5 pixels away (greater than 4.5 mm), and a small subset reaches beyond 10 mm. These long-range scatter events typically result from forward-directed Compton scattering at shallow angles, which deposits little energy in the initial interaction and allows the photon to travel further before interacting again.

These insights highlight the necessity of incorporating spatial filtering strategies or DOI-aware reconstruction methods to mitigate the influence of widely separated secondary hits. Furthermore, understanding the displacement distribution is essential for simulating realistic detector performance and for interpreting spatial uncertainty in experimental data.

6.2.4 Discussion

The Monte Carlo simulation offers a comprehensive characterization of the detector's response to 511 keV gamma photons. The results confirm that Compton scattering is the predominant interaction mechanism in LYSO at this energy, resulting in a high incidence of multiple-interaction events. This behavior is crucial for understanding the intrinsic limitations and potential of the detector system.

One of the key outcomes of the study is the demonstration that energy filtering can

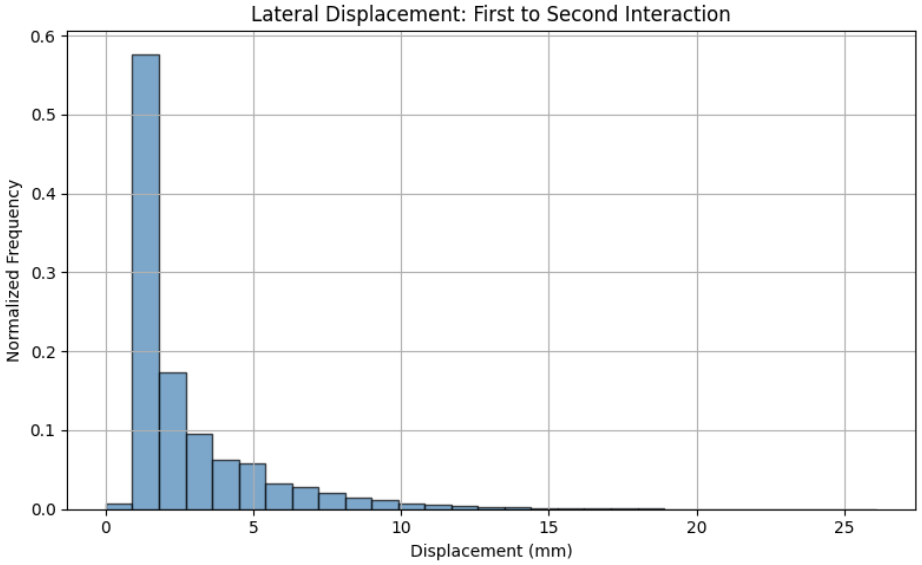

Figure 6.13: Distribution of lateral displacement between the first and second interaction points for all multiple-interaction events. Bin size is 0.9 mm, matching the scintillator pixel pitch.

significantly reduce the contribution of inter-crystal scatter (ICS) events. This forms a foundational strategy for event selection and reconstruction, offering a theoretical basis for improving spatial resolution and reducing mispositioned events.

However, it is important to recognize that the simulation represents an idealized model and does not account for various real-world detector effects. Factors such as intrinsic radioactivity from lutetium, non-uniform irradiation, photon escape (leakage), and electronic noise are not included. These phenomena can significantly impact detector performance and complicate the interpretation of experimental data.

Furthermore, the simulation tracks energy depositions on a per-pixel basis, assuming ideal charge collection and ignoring the complex physical processes that occur within a real scintillator. In practice, gamma interactions generate visible scintillation light, which then propagates through the crystal and undergoes various optical and electronic transformations before being recorded. These additional stages introduce further uncertainties and resolution losses that must be considered in a complete system model.

Despite these limitations, the simulated dataset provides a valuable reference framework for understanding fundamental interaction mechanisms and guiding reconstruction strategies. In the subsequent sections, this dataset will be integrated with experimental data to validate the simulation outputs and to address the detector's behavior under realistic conditions.

6.3 Evaluations of Pixel-wise Channel Parametrization and Filtering Efficiency Using Simulated Data

The simulation framework described in Section 6.2 was extended to evaluate the accuracy and effectiveness of the pixel-wise channel parameterization described in Section 6.1. The goal of this section is twofold: to validate the fidelity of the extracted parameters by reconstructing spatial event distributions from simulated interactions, and to assess the impact of parameter-based filtering strategies in enhancing event purity.

6.3.1 Synthetic Signal Generation Using Pixel Parameters

Simulated interactions (event ID, pixel of interaction, energy deposited) were processed using the pixel-wise channel mean and standard deviation values extracted from experimental FDG data. For a given pixel (j, k) in layer ℓ, each channel ch_i with $i \in \{0, 1, 2, 3\}$ was sampled from a Gaussian distribution:

$$ch_i \sim \mathcal{N}\left(\mu_{ch_i}^{(j,k,\ell)},\, \sigma_{th}\right) \cdot \frac{E}{0.511\ MeV}, \tag{6.8}$$

where E is the deposited energy in MeV, and 0.511 MeV is the reference energy used for normalization. The standard deviation σ_{th} was fixed at 20, based on the empirical reduction factor $\sigma_{ch_i}/15$ introduced in Figure 6.9. This scaling produced flood maps with realistic spatial distributions and represents a pragmatic calibration choice for incorporating realistic signal fluctuations in simulation. While the use of μ_{ch_i} alone would suffice for idealized conditions, the added stochastic component better mimics experimental noise.

The summed signal, representing total energy deposition, is:

$$SumCh = ch_0 + ch_1 + ch_2 + ch_3. \tag{6.9}$$

The reconstructed spatial position is obtained using standard Anger logic:

$$x = \frac{ch_0 + ch_1 - ch_2 - ch_3}{SumCh}, \quad y = \frac{ch_0 - ch_1 - ch_2 + ch_3}{SumCh}. \tag{6.10}$$

Single and Multiple Interaction Events

Simulated events were classified based on the number of energy depositions associated with a single 511 keV photon:

- **Single Interaction (SI):** Events with a single energy deposition, typically corresponding to photoelectric absorption or Compton scattering followed by photon escape.

- **Multiple Interaction (MI):** Events with two or more energy depositions, generally resulting from inter-crystal Compton scattering within the detector volume.

In the SI case, spatial reconstruction was performed using Anger logic, as defined in Eq.6.10. The resulting flood map (Figure6.14) shows a well-defined pixel grid, indicating high spatial accuracy when the interaction is unambiguous. Over 96% of the events are reconstructed within their expected pixel region, defined by a window of $\mu_x \pm 2\sigma_x$ and $\mu_y \pm 2\sigma_y$. The few outliers are attributed to statistical fluctuations during signal sampling.

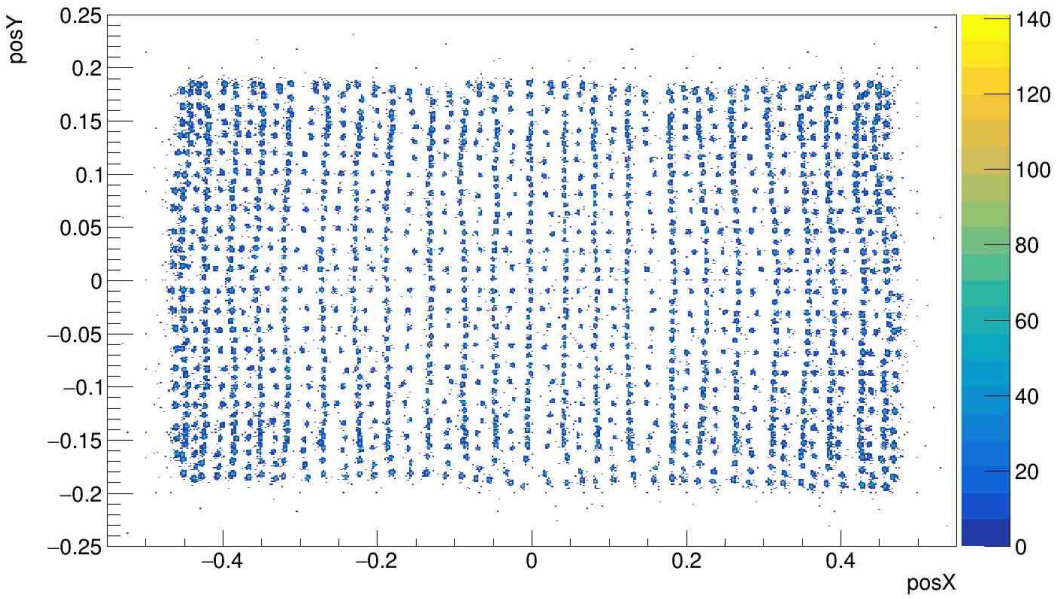

Figure 6.14: Reconstructed flood map from synthetic single interaction events. The pixel grid is sharply defined.

For MI events, channel signals from all interaction points belonging to the same primary photon were summed before position reconstruction. The position was then computed using the modified Anger logic (Eq. 6.11). This process effectively emulates the spatial smearing caused by multiple energy depositions contributing to the same light signal.

$$ch_i^{\mathrm{MI}} = \sum_{n=1}^{N} ch_i^{(n)}, \tag{6.11}$$

$$x^{\mathrm{MI}} = \frac{ch_0^{\mathrm{MI}} + ch_1^{\mathrm{MI}} - ch_2^{\mathrm{MI}} - ch_3^{\mathrm{MI}}}{\sum_i ch_i^{\mathrm{MI}}}, \tag{6.12}$$

$$y^{\mathrm{MI}} = \frac{ch_0^{\mathrm{MI}} - ch_1^{\mathrm{MI}} - ch_2^{\mathrm{MI}} + ch_3^{\mathrm{MI}}}{\sum_i ch_i^{\mathrm{MI}}}. \tag{6.13}$$

The resulting flood map for MI events (Figure 6.15) shows a diffused spatial distribution of events, without a clear pixel pattern. Only about 27.5% of MI events are localized within pixels region. The rest are scattered across the flood map due to the non-local nature of the composite light signal.

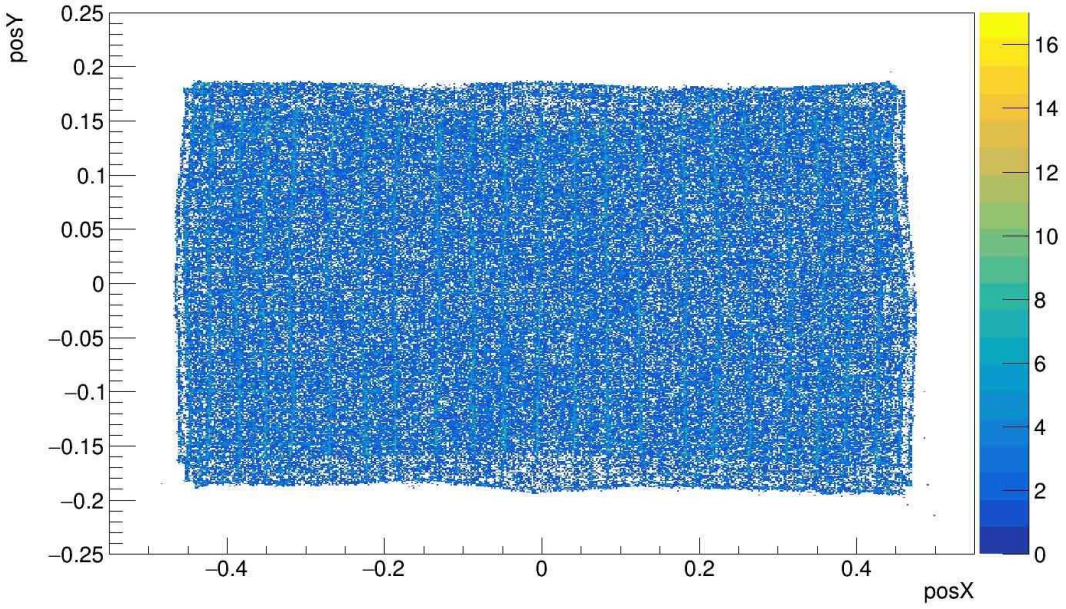

Figure 6.15: Flood map reconstructed from multiple interaction events.

When SI and MI events are merged (Figure 6.16), the resulting flood map displays a distinct pixel arrangement primarily characterized by localized SI events, while MI events introduce dispersed noise. This simulated map offers an accurate representation of the experimental flood map produced post-coincidence and energy filtering, as shown in Figure 6.1.

A more direct comparison is presented in Figure 6.17, where a zoomed region of the synthetic flood map is compared to the experimental flood map. While absolute intensities differ, the structural similarity is evident. Notably, approximately 75% of experimental events fall within defined pixel regions (LUT) after coincidence and energy filtering, closely matching the 68% value observed in the simulation. This confirms

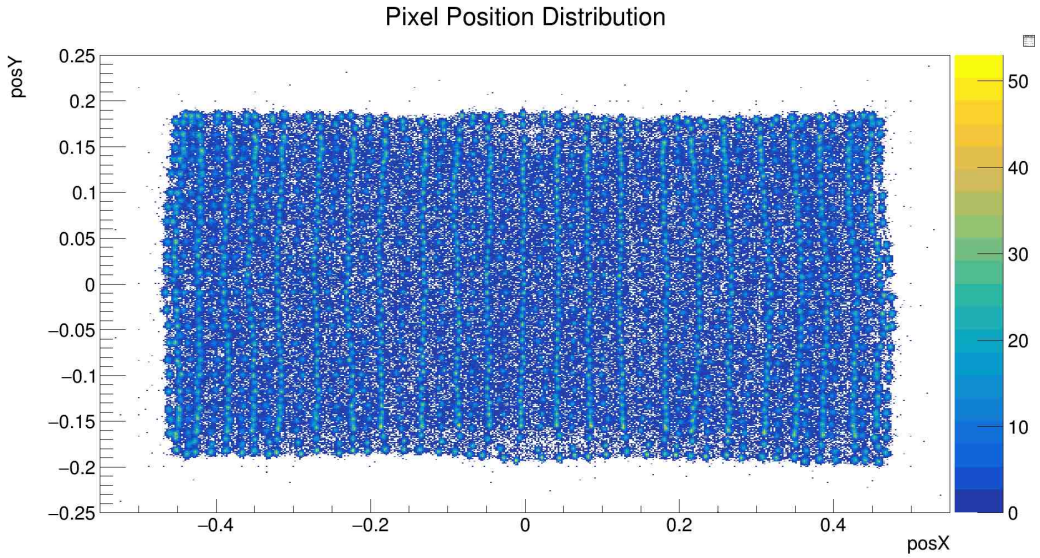

Figure 6.16: Sum of floodmaps from single and multiple interaction events. The central pixel grid, sharply defined, reflects single interactions, while the surrounding noise illustrates the degradation due to multiple interaction events.

that the simulation framework calibrated with pixel-wise parameters provides a robust approximation of the detector's spatial response under controlled conditions.

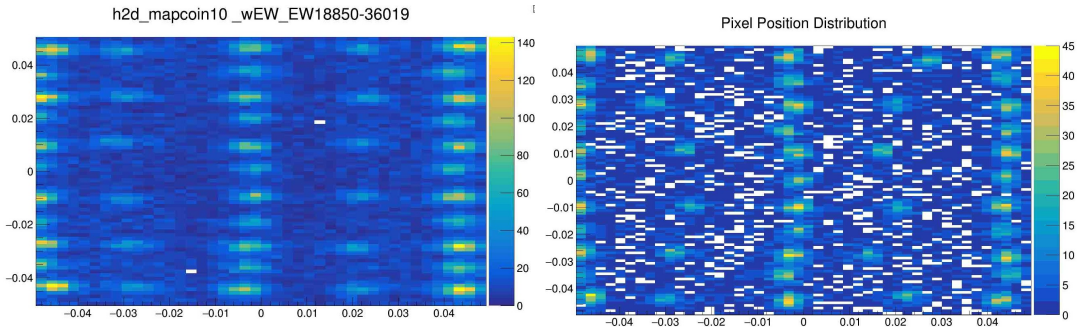

Figure 6.17: Zoomed comparison between experimental (left) and synthetic (right) flood maps. Structural features and localization patterns are consistent.

Further insights are provided by analyzing the layer-wise energy spectra of synthetic events, shown in Figure 6.18. These spectra are presented separately for Single Interaction (SI) and Multiple Interaction (MI) events.

In the SI case (Figure 6.18a), a photopeak near 511 keV is clearly visible across all layers, reflecting events where the full gamma energy is deposited in a single location. A low-energy considerable tail is also observed, arising from interactions where part of the photon energy escapes the detector. The appearance of multiple sub-peaks and the broadening of the spectral lines are attributed to variations in channel gain and calibration among different pixels. Color coding (red, black, blue) highlights differences

among the first, second, and third detector layers, respectively, with deeper layers generally showing increased spectral noise and broader peaks due to light attenuation and increased uncertainties.

The MI spectra (Figure 6.18b) exhibit a broader and more irregular distribution. While the total deposited energy ideally approaches 511 keV through the sum of multiple partial depositions, the variance in individual interaction locations and energies results in significant spectral broadening. Despite the similar global structure to the SI spectra, MI spectra display heightened noise levels, reduced peak definition, and layer-dependent inconsistencies.

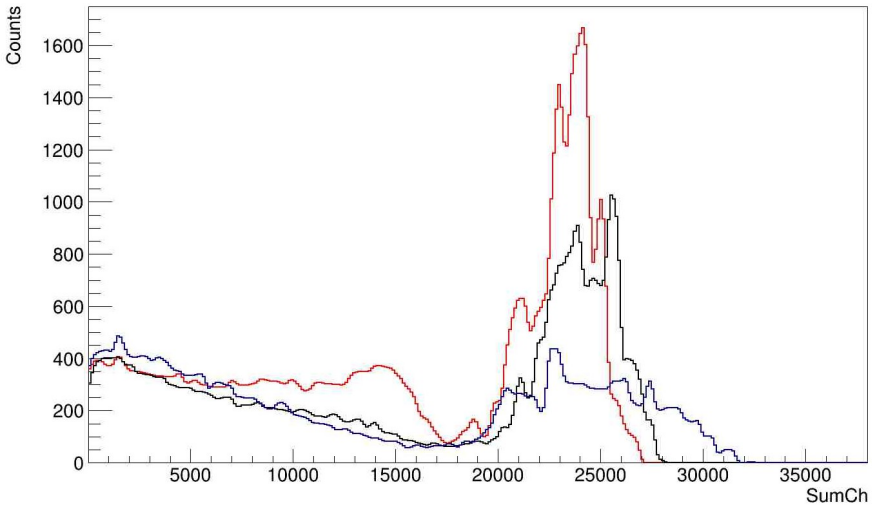

(a) Single Interaction (SI) layer-wise spectra

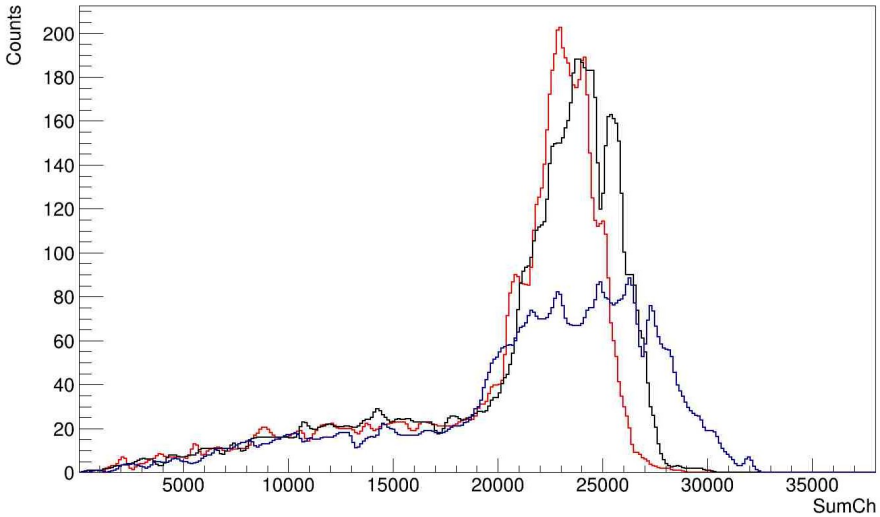

(b) Multiple Interaction (MI) layer-wise spectra

Figure 6.18: Energy spectra from synthetic data, color-coded by detector layer (red: 1st layer, black: 2nd layer, blue: 3rd layer).

When compared to the experimental spectra shown in Figure 5.8, the synthetic

distributions demonstrate good qualitative agreement. However, synthetic data tend to exhibit slightly higher noise, particularly for the MI case. This is likely due to both limited simulation statistics and the stringent pixel assignment procedure applied during synthetic signal generation.

Overall, this study confirms the good accuracy of the synthetic model in reproducing key features of real PET flood maps and energy spectra. While real-world measurements are further complicated by noise, cross-talk, and calibration drift, the simulation results provide a reliable foundation for interpreting event topology and optimizing reconstruction strategies.

6.3.2 Filtering Based on Pixel Spatial and Spectral Parameters

To assess the effectiveness of event-level filtering based on spatial and spectral characteristics, synthetic single-interaction (SI) and multiple-interaction (MI) events were analyzed using calibrated pixel-wise descriptors from all three detector layers. Although the third layer exhibits less precise calibration and broader signal distributions, it was retained in the analysis for consistency, as the simulation framework was parametrized on all three layers. Filters were applied on reconstructed spatial coordinates, total energy, and individual channel responses to evaluate how different constraints affected event retention.

The filtering strategy employed four main criteria:

- **Pixel-wise Spatial Filter:** Retains events whose reconstructed (x, y) positions lie within $\mu_x \pm n_x\sigma_x$ and $\mu_y \pm n_y\sigma_y$ of the assigned pixel reference.
- **Pixel-wise Energy Filter:** Retains events whose total energy signal lies within $\mu_E \pm n_E\sigma_E$.
- **Channel Filter:** Each channel ch_i must satisfy $|ch_i - \mu_i| < n_C \cdot \sigma_i/2$, with $i = 0, 1, 2, 3$.
- **Global Energy Window (GEW):** A fixed total energy filter in the range $[18850, 36019]$ ADC units, mimicking the energy selection used in experimental SIRMIO PET acquisitions of detector 10.

Filtering tolerances $n_x = n_y$, n_E, and n_C were varied to assess their combined impact. Table 6.6 summarizes the results for various filter combinations, reporting the following key metrics:

- **GEW:** Indicates whether the Global Energy Window filter was applied (Yes/No).

- $\boldsymbol{n_x, n_y}$, $\boldsymbol{n_E}$, $\boldsymbol{n_C}$: Numerical tolerances for spatial, energy, and channel filters, respectively.
- **SI** : Percentage of single-interaction events retained after filtering.
- **MI** : Percentage of multiple-interaction events retained after filtering.
- **Global Acceptance** : Overall percentage of events accepted, calculated as:

$$\text{Global Acceptance} = \frac{\boldsymbol{N}^{\text{SI}}_{\text{passed}} + \boldsymbol{N}^{\text{MI}}_{\text{passed}}}{\boldsymbol{N}^{\text{SI}}_{\text{total}} + \boldsymbol{N}^{\text{MI}}_{\text{total}}} \tag{6.14}$$

- **SI presence** : Fraction of SI events among the total accepted events, calculated as:

$$\text{SI presence} = \frac{\boldsymbol{N}^{\text{SI}}_{\text{passed}}}{\boldsymbol{N}^{\text{SI}}_{\text{passed}} + \boldsymbol{N}^{\text{MI}}_{\text{passed}}} \tag{6.15}$$

Table 6.6: Acceptance rates of SI and MI events using different filtering configurations. GEW = Global Energy Window.

GEW	n_x, n_y	n_E	n_C	SI	MI	Global Acceptance	SI presence
No	2	–	–	97%	22%	62%	84%
No	4	–	–	99%	27%	65%	80%
No	4	–	2	36%	10%	24%	80%
No	4	–	4	38%	15%	27%	75%
No	4	2	–	37%	12%	25%	77%
No	4	4	–	40%	16%	29%	74%
No	2	2	2	35%	8%	23%	84%
No	4	4	4	38%	14%	27%	75%
Yes	–	–	–	43%	70%	55%	42%

Several observations emerge from this analysis:

1. **Spatial filtering alone** ($n_x = 4$) proves highly effective, eliminating over 70% of MI events while retaining approximately 99% of SI events. This confirms its strong discriminative power in distinguishing between event types. Conceptually, this filtering step mirrors the process of assigning events to pixels using a Lookup Table (LUT).
2. **Energy filtering** ($n_E = 2, 4$) significantly reduces SI retention. For example, SI acceptance drops from 99% to 40% as n_E increases from 0 to 4 (with $n_C = 0$). This is consistent with simulation results, which show that many single-interaction

events stem from 511 keV photons but involve partial energy deposition. Indeed, about 45% of SI events deposit less than 450 keV, so tightening the energy window helps isolate true full-energy deposition event

3. **Channel filtering ($n_C = 2$ or 4)** further reduces SI acceptance while effectively suppressing MI contributions to 10–15%. For instance, with $n_C = 2$, SI retention drops from 99% to 36%, indicating a strong dependency between strict spectral constraints and overall sensitivity loss. This approach mimics the energy filtering process on a per-channel basis, and thus produces qualitatively similar results.

4. **Combined filters with tight thresholds ($n = 2$)** yield strong MI suppression (7–10%) but at the cost of significantly reduced SI efficiency. Relaxed settings ($n = 4$) offer a better trade-off.

5. **Global Energy Window (GEW) filtering** alone suppresses SI events to 43% while retaining about 70% of MI events. This filter reflects realistic experimental conditions, targeting the 511 keV photopeak and effectively focusing on the 511 keV events, reducing SI with low energy deposited, ICS and background contributions.

Although the filtering strategies described above may appear overly strict, they reflect the real conditions required to remove incompletely scattered (ICS) and background events in order to obtain clean and high-quality PET images.

In practice, fundamental step in experimental data processing is the application of the Global Energy Window (GEW) filter to isolate events corresponding to full-energy 511 keV photon interactions. This establishes a realistic dataset that mimics experimental selection.

To further refine event selection, additional pixel-wise filters (spatial, energy, and channel-based) can then be applied to the GEW-filtered dataset. The goal is to examine how each of these criteria influences the acceptance rate of single- and multiple-interaction events in conditions comparable to real measurements.

Table 6.7 presents the resulting acceptance percentages, all calculated relative to the dataset pre-filtered by the GEW. This analysis provides insight into how well pixel-wise filtering strategies perform in realistic scenarios and how filter parameters influence event classification across detector pixels.

From Table 6.7, several key insights can be drawn regarding the performance of pixel-wise filtering strategies applied to a dataset pre-filtered with the Global Energy Window:

- **Spatial filtering alone** (e.g., $n_x = 4$, $n_E = 0$, $n_C = 0$) is sufficient to retain all SI events while suppressing MI events by nearly 72%. This reaffirms its role

Table 6.7: Acceptance rates of SI and MI events using different pixel-wise filter configurations on Global Energy Window (GEW) filtered synthetic data. All percentages are relative to the GEW-filtered dataset.

n_x, n_y	n_E	n_C	SI	MI	Global Acceptance	SI presence
2	–	–	99%	22%	63%	76%
4	–	–	100%	28%	57%	71%
4	–	2	86%	15%	54%	80%
4	–	4	91%	21%	59%	75%
4	2	–	88%	18%	56%	77%
4	4	–	94%	23%	62%	74%
2	2	2	85%	12%	51%	84%
4	4	4	90%	21%	59%	75%

as a strong primary discriminator, even under realistic conditions. Conceptually, this filtering step mirrors the process of assigning events to pixels using a Lookup Table (LUT).

- **Channel filtering** ($n_C = 2$ or 4) applied in addition to spatial filtering further reduces MI contributions, improving event purity. For instance, at $n_C = 2$, MI retention drops to 15% with SI acceptance still above 85%.

- **Energy filtering** ($n_E = 2, 4$) complements spatial filtering by enhancing MI suppression, with only a minor reduction in SI efficiency. For example, adding $n_E = 4$ reduces MI acceptance from 28% to 23%, while SI acceptance remains high (94%).

- **Combined filters with relaxed thresholds** (e.g., $n = 4$ for all) yield a balanced trade-off between SI retention (90%) and MI rejection (20%), suitable for general-purpose applications including image reconstruction.

- **The strictest filter setting** ($n = 2$ for all) results in the highest SI purity (83.6%) and the lowest overall acceptance (41.4%). This configuration is ideal for applications that prioritize data quality over quantity, such as ground truth extraction or resolution studies.

These results demonstrate that even after energy-based pre-selection, spatial and spectral filters remain highly effective for refining event classification. By examining the SI presence metric, we observe a significant improvement: the fraction of SI events increases from approximately 42% in the GEW-only dataset to 70–80% after applying

pixel-wise filters. This indicates that the final filtered dataset is substantially enriched in true single-interaction events.

As previously noted, spatial filtering consistently proves to be the most impactful method for rejecting ICS and MI events, with spectral filters (energy and channel constraints) offering additional refinement. However, it is important to acknowledge that while MI events are substantially suppressed, they are not completely removed—approximately 20–25% of MI events persist in the final dataset. This residual presence likely consists of events involving small-angle scatterings or closely spaced interaction points, which result in spatial and spectral signatures that closely mimic those of SI events. Nevertheless, these remaining MI events are less likely to affect pixel assignment accuracy and thus have limited impact on overall image quality.

In summary, pixel-wise filtering based on spatial and spectral parameters greatly enhances event selection in in-beam PET systems. Spatial filters serve as a robust foundation, while energy and channel filters fine-tune the selection process. For datasets already constrained by a GEW, combining spatial filtering with moderate spectral thresholds provides an optimal compromise between event purity and retention. Stricter filters are well-suited for high-statistics analyses requiring maximum precision, whereas more relaxed criteria are advantageous for applications such as image reconstruction where higher event throughput is beneficial.

Chapter 7

Conclusion and Outlook

This thesis presented the modeling and pixel-wise characterization of a high-resolution depth-of-interaction PET detector developed within the SIRMIO project. The main objective was to extract spatial and spectral parameters for each detector pixel from both experimental and simulated data, with the aim of improving detector knowledge, supporting simulation-based validation, event filtering strategies, and enabling more accurate image reconstruction in small animal in-beam PET applications.

A dedicated Monte Carlo simulation framework was performed, offering initial insights into photon interaction mechanisms, energy deposition, and interaction multiplicity within the detector's layered scintillator architecture. This simulation capability proved useful for interpreting experimental observations and understanding expected physical behavior.

An investigative pixel-wise study then followed, utilizing both FDG-filled Derenzo phantom and back-irradiation experimental datasets. This characterization focused on a single detector module (detector 10), where each pixel across its layers underwent an initial spatial and spectral analysis. Spatial parameters, specifically centroids and standard deviations, provided pixel localization in the flood map. Spectral characterization involved Gaussian fitting of individual channel energy distributions, offering a preliminary account for inter-pixel variability and systematic non-uniformities; however, significant limitations were identified, particularly at detector edges and in the deepest layer, indicating areas requiring substantial further attention and refinement. A custom software package was developed to manage this intricate characterization process and automate parameter extraction.

The extracted parameters were compiled into a preliminary pixel-wise detector database. While this custom software facilitated the automation of this extraction and initial management of data volumes, preliminary testing indicated that further development is crucial to ensure broad scalability and robustness, particularly for application across the entire system. Validation of the constructed parameter database through

synthetic event generation demonstrated its potential. By sampling channel values from Gaussian distributions derived from the pixel-wise parameters, reconstructed flood maps showed a qualitative reproduction of the detector's spatial characteristics. Furthermore, the application of pixel-wise filtering criteria to these synthetic datasets provided initial evidence that the extracted parameters could contribute to discriminating between well-localized and ambiguous events, suggesting a potential for improving the signal-to-noise ratio in input for downstream image reconstruction pipelines.

Outlook

The results presented in this thesis lay a strong foundation for future research and development aimed at fully realizing the capabilities of the SIRMIO PET system. A key next step will be the extension of the pixel-level characterization pipeline to cover the complete detector array, advancing well beyond the single detector module studied in this work. This expansion will require significant progress in automation and calibration, enabling scalable parameter extraction and continuous, system-wide monitoring of detector performance.

The preliminary pixel-wise database developed in this study shows promising potential to enhance image reconstruction algorithms. It may serve as a valuable source of prior information for regularization techniques or pixel-specific correction factors. However, further efforts are needed to rigorously assess its impact on reconstruction accuracy. Future work should focus on integrating more comprehensive light propagation models into simulation-based reconstruction frameworks, which is crucial for capturing the complexities of scintillation signal generation and transport. A key objective will be to quantify the improvements in spatial resolution and image quality achievable through these enhanced modeling techniques.

In parallel, the database and filtering tools developed here offer a starting point for a more refined treatment of inter-crystal scattered (ICS) events. While such events are typically discarded to preserve image fidelity, the flexibility of the filtering criteria allows for a tunable balance between sensitivity and specificity. Future studies should investigate advanced approaches to not merely to suppress ICS signals, but to reinterpret and recover useful information from them. This could lead to measurable gains in detection sensitivity, provided that resolution is not adversely affected.

In summary, the methodologies and insights gained from this work contribute to a growing understanding of pixel-wise detector behavior in high-resolution PET systems. These developments represent an important step toward improving in-beam PET imaging performance, with the overarching goal of achieving higher precision and reliability in both preclinical and future clinical applications in radiation oncology.

Bibliography

[1] European Commission, Joint Research Centre. 2040 cancer estimates: A preview of the cancer burden in 2040 across european countries. `https://ecis.jrc.ec.europa.eu/sites/default/files/2024-09/2024_08_Factsheet_2040CancerEstimates.pdf`, August 2024. Accessed April 2025.

[2] Madelon C. G. Pijls-Johannesma, Janneke P. C. Grutters, Frank Verhaegen, and Dirk De Ruysscher. Do we have enough evidence to implement particle therapy as standard treatment in lung cancer? a systematic literature review. *The Oncologist*, 15(1):93–103, 2010.

[3] R. F. Mould. *A Century of X-rays and Radioactivity in Medicine: With Emphasis on Photographic Records of the Early Years*. CRC Press, 1993.

[4] D. I. Thwaites and J. B. Tuohy. Back to the future: The history and development of the clinical linear accelerator. *Physics in Medicine and Biology*, 51(13):R343–R362, 2006.

[5] T. Bortfeld. An analytical approximation of the bragg curve for therapeutic proton beams. *Medical Physics*, 24(12):2024–2033, 1997.

[6] K. Otto. Volumetric modulated arc therapy: Imrt in a single gantry arc. *Medical Physics*, 35(1):310–317, 2008.

[7] R. D. Timmerman. An overview of hypofractionation and introduction to this issue of seminars in radiation oncology. *Seminars in Radiation Oncology*, 25(1):1–5, 2014.

[8] M. Durante and J. S. Loeffler. Charged particles in radiation oncology. *Nature Reviews Clinical Oncology*, 7:37–43, 2010.

[9] M. Scholz and G. Kraft. Track structure and the calculation of biological effects of heavy charged particles. *Advances in Space Research*, 18(1-2):5–14, 1996.

[10] M. Yang, G. Virshup, J. Clayton, X. Zhu, W. Hsi, and R. Mohan. Theoretical variability of relative stopping power ratios for proton therapy. *Medical Physics*, 39(7):4199–4208, 2012.

[11] A. C. Knopf and A. Lomax. In vivo proton range verification: A review. *Physics in Medicine and Biology*, 58(15):R131–R160, 2013.

[12] A. C. Kraan. Range verification methods in particle therapy: Underlying physics and monte carlo modeling. *Frontiers in Oncology*, 5:150, 2015.

[13] Katia Parodi. Vision 20/20: Positron emission tomography in radiation therapy planning, delivery, and monitoring. *Medical Physics*, 42(12):7153–7168, December 2015.

[14] W. R. Leo. *Basic Nuclear Processes in Radioactive Sources*. Springer Berlin Heidelberg, Berlin, Heidelberg, 1994.

[15] Silvia Liprandi. *Development and performance evaluation of detectors in a Compton camera arrangement for ion beam range monitoring in particle therapy*. PhD thesis, Ludwig-Maximilians-Universität München, München, Germany, September 2018.

[16] K. Parodi, W. Assmann, C. Belka, J. Bortfeldt, D.A. Clevert, G. Dedes, R. Kalunga, S. Kundel, N. Kurichiyanil, P. Lämmer, J. Lascaud, K. Lauber, G. Lovatti, S. Meyer, M. Nitta, M. Pinto, M.J. Safari, K. Schnürle, J. Schreiber, P.G. Thirolf, H.P. Wieser, and M. Würl. Towards a novel small animal proton irradiation platform: the sirmio project. *Acta Oncologica*, 58(10):1470–1475, October 2019.

[17] Glenn F. Knoll. *Radiation Detection and Measurement*. John Wiley & Sons, 4th edition, 2010.

[18] F. Evangelista. Characterization of a small animal in-beam pet scanner prototype developed in the context of the sirmio project. Master's thesis, Sapienza University of Rome, Faculty of Physics, 2021.

[19] F. H. Attix. *Introduction to Radiological Physics and Radiation Dosimetry*. John Wiley & Sons, 2008.

[20] A. Ghassemi, K. Sato, and K. Kobayashi. *Technical Guide to Silicon Photomultipliers (MPPC)*. Hamamatsu Photonics K.K., 2022.

[21] R. Ganai, S. Mehta, M. Shiroya, M. Mondal, Z. Ahammed, and S. Chattopadhyay. A proof-of-principle for time of flight-positron emission tomography imaging. In M. Naimuddin, editor, *XXII DAE High Energy Physics Symposium*, volume 203 of *Springer Proceedings in Physics*, pages 405–410. Springer, Cham, 2018.

[22] William W. Moses. Fundamental limits of spatial resolution in pet. *Nuclear Instruments and Methods in Physics Research A*, 648:S236–S240, 2011.

[23] Frederic H. Fahey. Data acquisition in pet imaging. *Journal of Nuclear Medicine Technology*, 30(2):39–49, 2002.

[24] Gengsheng Lawrence Zeng. Image reconstruction—a tutorial. *Computerized Medical Imaging and Graphics*, 25(2):97–103, 2001.

[25] Munetaka Nitta, Fumihiko Nishikido, Naoko Inadama, Yoshiyuki Hirano, and Taiga Yamaya. Discrimination of inter-crystal scattering events by signal processing for the x'tal cube pet detector. *Radiological Physics and Technology*, 16, 2023.

[26] F. Evangelista, G. Lovatti, J. Bortfeldt, Z. Huang, M. Pinto, C. Gianoli, G. Dedes, H. G. Kang, T. Yamaya, P. G. Thirolf, K. Parodi, and M. Nitta. Effect of inter-crystal events inclusion on high resolution small-animal pet scanner performance. Poster presentation at IEEE Nuclear Science Symposium and Medical Imaging Conference, 2024. Poster ID: M-08-116.

[27] Giulio Lovatti, Munetaka Nitta, Mohammad Javad Safari, Chiara Gianoli, Marco Pinto, Georgios Dedes, Andreas Zoglauer, Peter G. Thirolf, and Katia Parodi. Design study of a novel geometrical arrangement for an in-beam small animal positron emission tomography scanner. *Physics in Medicine and Biology*, 68, 2023.

[28] Munetaka Nitta, Giulio Lovatti, Mohammad Javad Safari, Tobias Binder, Hyoung Gyu Kang, Satoshi Takyu, Georgios Dedes, Tatsuya Yamaya, Peter G. Thirolf, and Katia Parodi. Design and detector development for an in-beam small animal pet scanner. In *51. Jahrestagung der Deutschen Gesellschaft für Medizinische Physik (DGMP)*, 2020. Präsentation, virtuelle Konferenz.

[29] Hamamatsu Photonics K.K. MPPC (Multi-Pixel Photon Counter) S14160/S14161 Series. `https://www.hamamatsu.com/content/dam/hamamatsu-photonics/sites/documents/99_SALES_LIBRARY/ssd/s14160_s14161_series_kapd1064e.pdf`, 2019. Accessed: 2025-05-27.

[30] MediLumine Inc. Fillable micro derenzo phantom for pet and spect imaging. `https://medilumine.com/product/`

fillable-derenzo-phantom-for-pet-or-spect-imaging, 2024. Accessed: 2025-05-30.

[31] M. Nitta, G. Lovatti, F. Evangelista, J. Bortfeldt, M. Pinto, Z. Huang, N. Bassler, P. R. Poulsen, H. G. Kang, A. Zoglauer, C. Gianoli, G. Dedes, T. Yamaya, P. G. Thirolf, and K. Parodi. Characterization of the sirmio spherical small animal pet toward simultaneous beam and tracer imaging. In *Proceedings of the IEEE Nuclear Science Symposium and Medical Imaging Conference (NSS/MIC)*, 2024. Abstract submission.

[32] ROOT Team. ROOT: Data Analysis Framework. https://root.cern/. Accessed: 2025-05-27.

[33] Python Software Foundation. Python Language Reference, version 3.10. https://www.python.org/. Accessed: 2025-05-27.

[34] ROOT Team. *ROOT Users Guide*. CERN. Accessed: 2025-05-27.

List of Figures

List of Tables